Introduction de magnétosphères auto-cohérentes dans les simulations de jets d'objets stellaires jeunes

Petar Todorov

▶ **To cite this version:**

HAL Id: tel-02095151

https://hal.science/tel-02095151

Submitted on 10 Apr 2019

Introduction de magnétosphères auto-cohérentes dans les simulations de jets d'objets stellaires jeunes

Thèse préparée par

Petar Todorov

en vue de l'obtention du titre de

Docteur de l'Observatoire de Paris

Commission d'examen

Benoît Mosser	Président du jury
Paola ROSSI	Rapporteur
Hubert BATY	Rapporteur
Kanaris TSINGANOS	Examinateur
Jean-Pierre CHIÈZE	Examinateur
Christophe SAUTY	Directeur de thèse
Véronique CAYATTE	Co-directeur de thèse
João José LIMA	Co-directeur de thèse

Le 30 septembre 2013

Introducing Self-Consistent Magnetospheres in Simulations of Jets of Young Stellar Objects

a thesis prepared by

Petar Todorov

in fulfilment of the requirements for the degree of

Doctor of the Paris Observatory

Examination committee

Benoît MOSSER	Président du jury
Paola ROSSI	Rapporteur
Hubert BATY	Rapporteur
Kanaris TSINGANOS	Examinateur
Jean-Pierre CHIÈZE	Examinateur
Christophe SAUTY	Directeur de thèse
Véronique CAYATTE	Co-directeur de thèse
João José LIMA	Co-directeur de thèse

September 30, 2013

На брат ми Димитър
Dedicated to my brother Dimitar

Acknowledgements

I would like to express my gratitude, thanks and appreciation to all the people who contributed, in one way or another, to the successful ending of this thesis. I would like to thank the jury members, *le Président* of the jury, Benoît Mosser, *les Rapporteurs* Paola Rossi and Hubert Baty, and *les Examinateurs* Kanaris Tsinganos and Jean-Pierre Chièze, for taking interest in this work.

I would like to thank Christophe Sauty, Véronique Cayatte and João José Lima, who accepted me to work under their direction the last three years. For giving me the freedom to carry out this work as I intented it, and from whose approach I learned a lot.

The last three years, I have enjoyed a very favourable working atmosphere in the Paris Observatory, in the *Laboratoire de l'Univers et ses Théories* in particular, and the Doctoral school. It is now difficult to imagine how could one carry out research in Astrophysics without taking frequent walks in the forest or around the lake in the middle of the campus! I would like to thank the *luthiers* and the fellow PhD students (current and former!) in Meudon and Paris, for sharing the coffee breaks, for all the fruitful discussions we had, debunking pseudoscience or *Talking Big* about the future. I would also like to thank Pierre Lesaffre, who was my *parrain* in the Doctoral school and who helped me a lot.

I will never forget why I crossed the door of the Observatory and Planetarium in Varna. I was wondering how people see the lines, connecting stars in constellations. I had questions. I came out with much more questions (lines connecting stars do not exist, but why do stars explode?) I thank Eva Bojurova for tirelessly repeating to me: *"Never discard the result that does not fit your exceptations. It might be your most interesting finding."* This way, the seed of scientific exploration started to take roots in my mind and deciding to take a deep interest in Physics became the most natural thing for me.

As Winnie the Pooh famously said, *A day without a friend is like a pot without a single drop of honey left inside.* I would like to thank my friends (those who recognized themselves in the lines before and those who will recognize themselves in those lines), for being what they are. Whenever we

gather in Varna, Sofia, Belite brezi, Paris, Bures, Barcelona, Boston, (and this is only where we gather, because we literally live all over the world,) or we go to several of those places, I cherish every moment spent with you and I feel privileged. You and my family are, as Pooh said it in such a beautiful way, the honey of my days.

Nothing would have been possible without my family. My mother Vania and my aunt Nadka. Whenever I'm living 2065 km or 7560 km from home, I feel them caring about me. But nothing rejoyces me more than seeing them at home. Finally and most importantly, I would like to thank my brother Dimitar who continually inspires me. As every time I was asking myself *"Muß es sein?"*, the answer invariably was *"Es muß sein!"*, *what kind of a serious older brother is not finishing what he has started?*

Abstract

The detailed comprehension of the observed properties of Jets of Young Stellar Objects requires the construction of models, accounting for the observations, but allowing us, by the knowledge of the hypotheses under which those models are constructed, to gain insight into the physical processes responsible for the observed behaviours. Once such models elaborated, we need to test their stablity, and to improve the models, when they exhibit inconsistencies.

In this thesis, we are going to study the stability of solutions for Jets of Young Stellar Objects, and then to change them, in order to include static magnetosphere. The approach we employed is to initialize a simulation box with a semi-analytical solution of a global collimated outflow with non-null velocities in the magnetosphere, and to test its stablity. Then we modify accordingly the semi-analytical solution in order to account for a static magnetosphere. The final state to which the simulation relax is then a numerically obtained solution for global flow with a dead zone. We obtain two different solutions, one for a heated, and one for a non heated dead zone. We discuss the astrophysical implications of the properties of these solutions.

The plan of this thesis is the following: In the Chapter 1, first we make an introduction to the theory of star formation, and second, to the theory and observations of Jets of Young Stellar Objects. In Chapter 2, we discuss the general framework in which we operate, which are the equations of ideal Magnetohydrodynamics, and how the collimated outflows of Young Stellar Objects are studied analytically. In Chapter 3, we discuss the topological stablity of a solution, describing an axisymmetric, collimated stellar outflow. In Chapter 4 we obtain a numerical solution for a jet with static magnetosphere, and discuss how this refers to the observations. In Chapter 5, we compare to the solution, presented in Chapter 4 another solution, in which the dead zone is heated.

Résumé

La compréhension détaillée es propriétés observées des jets des objets stellaires jeunes nécessite la construction de modèles. Ceux-ci tiennent compte des observations et nous permettent de mieux comprendre les processus physiques responsables des phénomènes observés. Une fois de tels modèles construits, nous devons tester leur stabilité, et les améliorer.

Dans cette thèse, nous étudions la stabilité de solutions de jets d'objets stellaires jeunes et les modifier, afin d'en inclure des magnétosphères statiques. L'approche utilisée est l'initialisation d'une simulation numérique avec une solution semi-analytique de jet, dont la vitesse d'écoulement dans la magnétosphère est non-nulle. On vérifie aussi la stabilité de cette solution. Dans un second temps, nous allons modifier la solution semi-analytique de manière auto-cohérente afin qu'elle corresponde à un modèle avec une magnétosphère statique. L'état final vers lequel la simulation converge est alors une solution, obtenue numériquement, de flot collimaté avec une zone morte. Nous obtenons deux solutions différentes, une pour une zone morte chauffée, et une autre pour une zone morte qui n'est pas chauffée. Nous discutons des implications astrophysiques de ces solutions.

Le plan de cette thèse est le suivant: dans le Chapitre 1, nous allons tout d'abord faire une introduction de la théorie de la formation des étoiles, et ensuite, dans la théorie et des observations des jets des étoiles jeunes. Dans le Chapitre 2, nous discutons le cadre général dans lequel on se place, à savoir les équations de la magnétohydrodynamique idéale, et nous discutons également les procédés analytiques utilisés pour étudier les jets des étoiles jeunes. Dans le Chapitre 3, nous discutons la stabilité topologique d'une solution particulière, qui décrit un vent stellaire collimaté stationnaire et axisymétrique. Dans le Chapitre 4, nous obtenons une solutions numérique d'un jet avec une magnétosphère statique. Nous discutons la relation entre cette nouvelle solution et les observations. Finalement, dans le Chapitre 5, nous comparons à la solution obtenue dans le Chapitre 4 une autre solution, dans laquelle la zone morte est chauffée.

Contents

11

List of Figures

List of Tables

Chapter 1

Introduction

Contents

Chapter Abstract

The goal of this thesis is to study models of static magnetospheres in collimated outflows from Young Stellar Objetcs. This requires to introduce first the general context of such a study, by giving an outlook of the current astrophysical paradigm on star formation, which is the formation of protostellar cores in molecular clouds by gravitational collapse, which is governed by the interplay of gravitation, magnetic fields and hydrodynamics, and to describe how collimated outflows – or 'jets' – are part of this theory. The choice we made is to introduce the reader in this framework by starting with an outlook of this very general topic within Astrophysics, which is the theory and observations of Young Stellar Objects, and then to discuss observations and theory of jets. Afterwards, in subsequent chapters, we will discuss the particular models we studied in order to gain insight into these phenomena.

1.1 Stellar variability. T Tauri variables as Young Stellar Objects

1.1.1 T Tauri stars as young stars

Once, the variability of a star was considered to be something unusual. Stars were considered to be part of the Aristotelean supralunar realm, to which was attached the notion of perfectness, or interchangeably, the lack of change. This view was prevalent prior to the advent of modern science

at the beginning of the 17th century. The first star to be described with certainty as variable is o Ceti. Although possibly previously identified as a nova, its periodic variability was discovered by Johannes Holwarda in 1638, and in 1642 Johannes Hevelius named it "Mira," meaning "The Wonderful," (Hoffleit, 1997) possibly imprinting in this name his fascination for the fact that some stars undergo changes. Nowadays, it is clear that, in some sense, every star is variable: stars and their vicinity undergo evolution, and some of the most beautiful physical theories have been employed in answering the question of where do stars come from, what they are, and where do they go. Also, it became clear that the star Mira is part of a class of variable stars in a latter stage of their evolution – an oscillating red giant stars – a class of stars named "Mira-type," after the first discovered of their kind. Similarly, a class of variable stars discovered by Alfred H. Joy in 1945, is named after the star that Joy identified as their prototype – the variable star T Tauri. What Joy pointed out as being characteristic for T Tauri stars (TTS) is their low luminosity, rapid irregular variations in the lightcurve, spectral type between F5 and G5, spectra with emission lines blue-shifted with respect to the absoption lines, and their association with dark or bright nebulae (Joy, 1945). Later, V. Ambartsumian identified TTS as Young Stellar Objects (YSOs), *i.e.* pre-main sequence stars, whose luminosity is due to gravitational contraction, an identification that will prove right (*e.g. Ray, 2007, and references therein*).

The described activity and peculiarities of TTS are nowadays explained by the presence of accretion disk, outflows such as stellar winds and highly collimated jets, and magnetic phenomena.

1.1.2   Interstellar clouds and T Tauri stars

As mentioned, TTS are observed close to nebulae, which are known to be cold molecular clouds, composed mainly of molecular hydrogen. H_2 is a homonuclear molecule with no permanent dipole moment and hence is not interacting with electromagnetic radiation. As the gas is optically thin at these densities, H_2 is not directly observable. Instead, its density is inferred

from the density of "tracer" molecules, which abundances are supposed to have fixed values. Different 'tracer' molecules are used to track H_2, allowing the density of the molecular gas to be measured with different precisions, such as CO and SO. State-of-the-art instruments such as those on the Herschel Space Observatory, which mission recently ended, observe more robust tracers, such as HF (Sonnentrucker *et al.*, 2010). Apart H_2, CO, SO and HF, various other compounds are present in cold molecular clouds, such as NH_3, Polycyclic aromatic hydrocarbons (PAHs) and most notably, dust. Dust accounts for only 1% of the cloud mass, but is responsible for the optical thickness of the cloud. The size of dust particles have long been an open question. Their size has been determined recently by observing the scattered light of close objects at certain wavelenghts: they were found to scatter mostly light at $3.6\mu m$ (phenomenon called "cloudshine" or "coreshine", for denser regions), which could be done by dust particles that have typical sizes of $1\mu m$ (Pagani et al., 2010). More than 4 000 Giant Molecular Clouds (GMCs) are found in the Milky Way galaxy, with much more Small Molecular Clouds (Ray, 2007). Among them, the Taurus-Auriga (GMC), Ophiucus (SMC) and Orion (GMC) star-forming regions are studied in greater detail than others. (Hartmann, 2009).

1.1.3 Gravitational collapse of a young star

Stars form in gravitationally bound overdense regions in these clouds, which can be clumps or prestellar cores (commonly called also "compact sources"). Clumps are sites of formation of young stellar clusters, such as the Trapezium cluster at the heart of the Orion nebula. Cores are sites of formation of individual stars or small multiple systems (Ray, 2007, and references therein). Another interesting feature of the interstellar medium is that it is structured in filaments. It seems to be ubiquitous as revealed by the Herschel Space Observatory (Molinari *et al.*, 2010), and clumps and cores appear along these filaments. This may mean that the molecular clouds first collapse in filaments before forming compact sources (Molinari *et al.*, 2010).

Once the compact source form, various mechanisms may prevent the gravitational collapse that will finally lead to the formation of a star. From theoretical point of view, the maximal mass of a sphere in hydrostatic equilibrium is

$$M_{BE} = 0.66 \frac{(T/10K)}{\left\{ P_{th}/(3 \times 10^5 \, k_B cm^{-3} K) \right\}^{1/2}} M_\odot \qquad (1.1)$$

and is called the Bonnort-Ebert mass (T being the temperature in Kelvin, P_{th} the thermal pressure and k_B Boltzman's constant). The Bonnort-Ebert mass' order of magnitude is $1M_\odot$ for typical clouds and is comparable to the Jeans mass (and respectively, the radius of the Bonnort-Ebert sphere is comparable to the Jeans length: $R_{BE} = 0.486 R_J$, which is the critical mass above which clouds are subject to fragmentation (McKee & Ostriker, 2007, and references therein.) When the gravitational collapse starts, the number density of the newly formed core is $n_{core} = 10^{-20} g.cm^{-3}$ (for the Sun, $n_\odot = 1 g.cm^{-3}$). Material spread at 1ly will collapse to a core with a diameter of 1 Mkm, and during that phase its temperature will rise from 10^2K to 10^6K (Ray, 2007, and references therein).

The mass of a core may exceed the Bonnort-Ebert mass, but gravitational collapse may still be stopped, and various factors are to be taken into account. The ISM is observed to be turbulent, with turbulent motions being sometimes supersonic. Observations of spectral lines of molecules such as CO show that their broadness varies on the observational scale, as expected from Kolmogorov's turbulent spectrum. Second, there is observational evidence for the presence of magnetic fields in the ISM such as the polarization of millimeter emission by aligned dust grains. Their strengths vary from few μG to few mG (Ray, 2007, and references therein). Cores that have the Bonnort-Ebert mass, but are supported by magnetic pressure are called sub-critical. And third, this balance may be modified by rotation.

The Cold neutral medium (CNM) component of the ISM is supposed to be subcritical or at most critical, thus the magnetic fields are able to stop the collapse at first. The quantative contribution of the gradient of magnetic

pressure to the force balance is dependant on the density structure of the core, hence observational evidence is not conclusive. (McKee & Ostriker, 2007 and references therein). Meanwhile, magnetic fields act directly only on ionised particles, and ionisation ratio of the ISM is quite low: 10^{-6}. Particles are supposed to be ionised by cosmic rays, and they interact with neutrals by friction. Depending on the balance of friction and magnetic forces, ions may be allowed to leak out, and the bulk of the cloud, contained in the neutrals, allowed to collapse. This process is called ambipolar diffusion, described for the first time by Mestel & Spitzer (1956). The dynamics of the magnetic field during the gravitational collapse remain an open question, with one of the classic problems of the theory of star formation being the fact that the ISM is strongly magnetized, and a star is weakly magnetized (McKee & Ostriker, 2007).

1.1.4 Evolutionnary sense of protostellar classes

1.1.5 Class 0

The gravitational collapse, when all the envelope is falling onto the star, continues until $n = 10^{-2}$g.cm^{-3} a second core is formed and hydrogen is ionised (Ray, 2007).

At this moment, 1% of the mass is in the core, and the other part is in the envelope. The star starts to accrete its spherical envelope: it's now a Class 0 protostar.

As mentioned, the peculiar activity of a TTS is partly attributed to the presence of an accretion disk. Observational evidence for the presence of accretion disks around YSOs are the observed excess in the infrared and millimeter emission and the fact that the red-shifted part of the emission lines is blocked. On theoretical grounds, the formation of an accretion disk is explained by considering the fact that rotation breaks the spherical symmetry of the cloud, thus material coming from sufficiently large distances in the surrounding nebula at the equator from below will have opposite

momentum flux with respect to material coming from above; this will lead to the formation of a shock at the equator. Gas passing trough this shock will see its entropy increases, hence it will loose kinetic energy, i.e. the infalling gas particles will stay close to the equator, forming a thin disk (Hartmann, 2009, and references therein).

Once a significant part of the envelope is accreted in the Class 0 phase, with the accretion rate being highly variable with respect to time, and outflow in the form of a massive wind and jets develop.This is observable, for instance, through the doppler-shifted CO rotationnal line emission (Ray, 2007, and references therein). Class 0 objects are optically invisible, but observable at far-infrared and millimeter wavelengths (Ray, 2007, and references therein).

1.1.6 Class I

When the disk is formed, the protostar enters a new phase, in which it accretes both from its envelope and disk, with the presence of an outflow. It's called a Class I protostar. Such objects are still optically invisible, but scattered light could be seen in the surrounding nebula (Ray, 2007, and references therein).

The phase corresponding to Class 0 and I together is sometimes called "embedded phase." The embedded phase should last up to 1Myr, according to theoretical models by Contopoulos & Sauty (2001), Dunham & Vorobyov (2012). Evans *et al.* (2009) argue that embedded phase lifetime is 0.44Myr, by counting Class 0 and I sources in the "cores to disks" (c2d) Spitzer spectroscopic survey and comparing their number to the number of Class II sources (based on the assumption that the lifetime of Class II sources is taken to be 2Myr). Class 0 and I sources ignite deuterium and the energy output from deuterium ignition is balancing the gravitational contraction. This is analoguous to the equilibrium between gravitational contraction and hydrogen burning of a main sequence star. T Tauri stars have been identified to have luminosities corresponding to what is predicted for YSOs

burning only deuterium, who follow an evolutionnary track on the HR diagram called "birthline", or "Hayashi track", situated above the main sequence. (Stahler, 1998) Once the main accretion phase is over, the stars stops burning deuterium, and starts burning hydrogen: it has become a zero-aged main-sequence star (ZAMS). As we already said, Class I stars accrete from their envelopes, but most importantly, from an accretion disk, which feature does not exist in Class 0 sources. An important thing to say is that the important part of the mass is already accreted; the mass of the envelope $M_{end} \ll M_{star}$, as opposed to Class 0 sources.

1.1.6.1 The luminosity problem of the embedded (Class 0 & I) phase

A significant shortcoming of the standard model is the luminosity problem. Embedded phase lasts at most 1Myr, which requires an accretion rate of $10^{-6} \, M_\odot yr^{-1}$, close to the accretion rate during the runaway collapse of Shu (1977). This implies luminosities of the order of $7L_\odot$, higher than the typically observed $1L_\odot$. The most plausible solution to this problem is that the accretion rate during the embedded phase is not steady, and that a significant portion of the mass is accreted during episodic bursts, such as those observed in FU Ori stars.

Recent physical models including such behaviour can be found in Dunham & Vorobyov (2012), thus making the median accretion rate (hence luminosity) significantly smaller than the needed mean accretion rate. It is not clear if such scenarii match the observational evidence, since dynamical properties of outflows and jets of Class 0 objects suggest different timings for such outbursts, so further observational studies are called for. Part of the solution of the luminosity problem may be that a more significant fraction of the accretion energy is carried away by outflows and jets (McKee & Ostriker, 2007 and references therein).

1.1.7   Class II

Once the envelope is accreted and there is an accretion disk, the protostar is now a Class II YSO. It is optically visible either as Herbig Ae/Be star (stars with mass of a several solar masses), either as T Tauri star ($1 - 2M_\odot$). A low-mass star in this stage is called a "Classical T Tauri star" (cTTS). The disk continues to accrete and the outflow is developped and potentially observable. (Ray, 2007, and references therein, Hartmann, 2009, and references therein). cTTSs exhibit accretion rates of $10^{-8}M_\odot yr^{-1}$ (Sauty *et al.* (2011) and references therein). Outflows in YSOs last at least 10^6yr. (Bouvier, Forestini, & Allain, 1997) As the cloud, surrounding the young stars dissipates with age, evolved young stars are easier to observe.

The models we are going to present in subsequent chapters are concerning jets from Class II YSOs.

1.1.8   Class III

Class III YSOs, also called "Weak-lined TTS" (wTTS), are even more evolved protostars, where the disk is cleared from the gas, and the remaining dust is about to be used as a material for planet formation. Some authors identify cTTS with fast rotators and wTTS with slow rotators (Kundurthy *et al.*, 2006). Furthermore, Sauty *et al.* (2011) argue that wTTS may also have jets, naturally of purely stellar origin, but undetectable with up-to-date instruments.

Not all stars fall in this classes. For example, the star IM Lup is a transitionnal case between cTTS and wTTS (Günther *et al.*, 2013a), and MN Lup lost its disk of hot dust (Günther *et al.*, 2013b).

1.1.9 Attribution of classes according observationnal criteria

Before it became clear that the numbering of classes has evolutionary sense, classes were attributed to stars based on characteristics of their spectra. André, Ward-Thompson, & Barsony (2000) summarize the criteria used for spectral classification of YSOs. Thus, what is used for the original classification is the parameter α_{IR}, corresponding to the slope of the protostellar spectral energy distribution in the infrared band (wavelengths in the range $2.2\mu - 10 - 25\mu$):

$$\alpha_{\mathrm{IR}} = \frac{d\left(\lambda F_\lambda\right)}{d\lambda}. \tag{1.2}$$

In this classificatoon, $\alpha_{\mathrm{IR}} > 0$ corresponds to Class I, $-1.5 < \alpha_{\mathrm{IR}} < 0$ correspond to Class II and $\alpha_{\mathrm{IR}} < -1.5$ correspond to Class III (André, Ward-Thompson, & Barsony, 2000)

1.1.10 Summary

The presented picture of stellar formation has two other major shortcomings. Two of them are the angular momentum problem and the magnetic flux problem: ZAMS stars have much less of the two than an equivalent mass of ISM. The latter problem is frequently explained in the literature by a drop of ionisation during the gravitational collapse. As the gravitational collapse proceeds, the bulk of the cloud decouples from the magnetic field and the flux is accumulated mainly in the accretion disk. In addition, magnetic reconnection or turbulent diffusion may play a positive additional role to resolve this problem (McKee & Ostriker, 2007 and references therein).

The problem (e.g., Spitzer, 1978) of angular momentum extraction might be resolved by outflows such as massive stellar winds and jets, that may have enough angular momentum to torque down the star (e.g. Mestel, 2012 and Matt & Pudritz, 2008a).

Quantifying this process by models taking into account more aspects of outflow dynamics is still an open question.

1.2 Jets of Young Stellar Objects and angular momentum extraction

1.2.1 Angular momentum in Young Stellar Objects

An important issue arises in the theory of star formation, theory on which we gave a brief outlook in the previous section, which consist of the fact that, if a large mass of gas undergoes a gravitational collapse to form a compact pre-stellar source, and if nothing takes away the angular momentum of the collapsing core, then it should speed-up its rotation. How it comes that centrifugal forces do not tear apart the forming star during the core collapse? A 'break-up speed,' defined as the rotation velocity at which the centrifugal force equals the binding gravitational force, causing the rotating body to disintegrate, should be reached if nothing takes away the angular momentum. The observationnal evidence shows that, first, stars do form, and second, that the TTS rotate at only 10% of their break-up speed. (Bouvier, 1990, Edwards, 1993, Vogel & Kuhi, 1981)

This 'angular momentum puzzle' is still an open issue in theory of star formation. It is well established that bodies in different stages of their evolution have different angular momenta. This quantity is indeed measured in observations. As discussed in Belloche (2013), the specific angular momentum J/M for dense cores in molecular clouds is $J/M = 10^{21-22}\,\mathrm{cm^2 s^{-1}}$ (Goodman, 1993), a pre-main sequence star has $J/M = 10^{16-17}\,\mathrm{cm^2 s^{-1}}$ (Mathieu, 2004), and the Sun has a $J/M = 10^{15}\,\mathrm{cm^2 s^{-1}}$ (Pinto *et al.*, 2011). This brings out the question to quantify, as much as possible, observationnaly and theoretically, the mechanisms responsible for this loss of angular momentum during star formation.

An explanation for angular momentum removal from acreted matter in in young stars and dispersal of infalling circumstellar envelops comes from observations and theoretical models of jets of young stellar objects. Another hypothesis we are not going to explore in this work is involving the magneto-rotationnal instability (MRI) of Balbus & Hawley (1991). The involved

explanation is that the angular momentum is extracted by redistributing it to particles at large disk radii.

1.2.2 From Herbig-Haro objects to jets.

Jets were discovered indirectly, by Herbig (1950) and Haro (1950), who observed extended diffuse objects, associated with T Tauri stars, and coming in pairs, named subsequently Herbig-Haro (HH) objects, and nowadays commonly observed in star-forming regions. It was found, in the early 1980s, that these objects are parts of highly collimated bipolar jets of Young Stellar Objects (Dopita, Evans, & Schwartz, 1982, and later confirmed by Graham & Elias, 1983, Mundt & Fried, 1983, Reipurth et al., 1986) and is now a well established fact (Eislöffel, 2000, Ray, 1998, Reipurth & Bally, 2001). As collimated supersonic outflows, jets are likely to carry the angular momentum needed to be removed from the collapsing young star, and to test this hypothesis a great number of observations and theoretical models have been elaborated. Nowadays, jets are observed on a broad range of wavelenghts, from X-ray to radio (Arce et al., 2006) and on a broad range of low-mass YSOs at all evolutionnary stages. (Cabrit, 2007) Exception are the sources earlier than B0, who do not exhibit well collimated outflows. (Arce et al., 2006)

1.2.3 Propagation scale kinematic properties

Well collimated jets are spectacular cosmic phenomena, spreading on large distances and moving at supersonic speeds, thus creating shocks in the interstellar medium. Jets extend on typical linear scales of $0.1 - 1 \mathrm{pc}$ and their typical outflow velocities of $10 - 300 \, \mathrm{km \, s^{-1}}$. From the previous, we can deduce propagation timescales for jets, $t_{\mathrm{dyn}} = 10^2 - 10^5 \mathrm{yr}$. Observed timescales of jets fall indeed in this range: Arce et al. (2006) point out that the dynamical timescale of HH 211 is $10^3 \mathrm{yr}$, and Takahashi & Ho (2012)

report that the dynamical timescale of the jet of the protostellar core MMS-6/OMC-3 is 10^2 yr, making it the youngest observed molecular outflow known to date.

Another quantities, used for comparaison between different observations and models, are the momentum rates, typically $\sim 10^{-5}\,\mathrm{M_\odot km\,s^{-1}\,yr^{-1}}$, and the mass loss rates, $\sim 10^{-7}\,\mathrm{M_\odot\,yr^{-1}}$, but could be as high as $10^{-6}\,\mathrm{M_\odot\,yr^{-1}}$. (Arce *et al.*, 2006, Bontemps *et al.*, 1996) For example, from observations in forbidden emission lines, Bacciotti *et al.* (2000) deduce a mass loss rate for DG Tau of $\dot{M}_{\mathrm{jet}} = 2.4 \times 10^{-7}\,\mathrm{M_\odot\,yr^{-1}}$.

For Class I objects, measures in optical wavelenghts traced jets out to 0.05pc (10^4AU) to the source. The innermost parts of jets oberved in such detail are traced in the near-IR, as well as in [FeII] lines and H_2, but no further than 1000AU. (Cabrit, 2007)

Class II objects provide the strongest constraints, because when we observe such objects, we are looking mostly at the central driving source at the outflow, without an absorbing envelop. "Micro-jets" appear in such objects. They have a typical $\dot{M}$ of $10^{-8}\,\mathrm{M_\odot\,yr^{-1}}$. (Cabrit, 2007)

It is established, from radio observations, that outflows have an onion-like kinematic structure. In the interior we have a high-velocity, highly collimated atomic jet, encompassed by a wide, slow, ovoid H_2 cavity. (Agra-Amboage, 2009, Bacciotti *et al.*, 2000, Beck *et al.*, 2008) It is, however, the inner streamlines who dominate the emission. (Dougados *et al.*, 2004) and play a dominant role in the mass an angular momentum transport. (Coffey, Bacciotti, & Podio, 2008) The high-velocity beam of the DG Tau jet is moving at a velocity of $200\,\mathrm{km\,s^{-1}}$, and the low velocity beam at $100\,\mathrm{km\,s^{-1}}$ (Agra-Amboage *et al.*, 2011)

The properties of jets on different scales, *i.e.* coming from stars with different masses, are strikingly similar. The jets, appearing on massive YSOs (with luminosities $\sim 4\mathrm{L_\odot}$) appear to be scaled-up versions of $\sim 1\mathrm{L_\odot}$ jets. (Cabrit, 2007) There are similarities not only between jets from YSOs of

different masses, but also between jets from YSOs on different evolutionnary stages. They have similar properties, with the jet kinematic structure probably determined in early evolutionary stages. (Nisini, 2009, Pesenti *et al.*, 2003) This obviously enables a general theoretical approach on the problem of describing the dynamics of jets.

We will not focus in this brief outlook on the possible precessions of jets. Jets propagate along the axis of symmetry of the accretion disk, and their angles of precession do not exceed 5° on 10 yr timescale. (Cabrit, 2007) Numerical simulations of precessing jets are carried out by Cerqueira & de Gouveia Dal Pino (2004).

1.2.4 Accretion-ejection correlation

Jets of Young Stellar Objects are commonly observed in our galaxy. Around 400 are catalogued by different authors (Hatchell, Fuller, & Richer, 2007, Wu, Huang, & He, 1996, Wu et al., 2004). It is well established that outflows and specifically jets are related to accretion disks (Cabrit *et al.*, 1990, Hartigan, Edwards, & Ghandour, 1995). An indication for this is the fact that they are observed in star-forming regions, and that high-resolution images of disks in several jets sources have been obtained with the HST and instruments with adaptive optics. (McCaughrean *et al.*, 2000, and references therein) The direct link between accretion and ejection, in sources not necessarily accessible by direct imaging, comes from the observation of the correlation between the bolometric luminosity, in which the accretion luminosity has a major part, and the outflow rates, force and mechanical luminosity. (Cabrit & Bertout, 1992) This correlation can also be explicited as what part of the accreted mass is taken away by the jet. $f = \dfrac{\dot{M}_{\text{jet}}}{\dot{M}_{\text{acc}}} = 0.1$ is inferred in both Class 0 and I low-L objects. (Bontemps *et al.*, 1996) In the case of DG Tau, Coffey, Bacciotti, & Podio (2008) report $f = 0.07$, and for different YSOs in their sample, $f = 0.01 - 0.07$. To summarize, various strong apparent correlations between the observational signatures of

accretion and the observationnal signatures of outflows have been observed during the years. (Cabrit & André, 1991, Cabrit *et al.*, 1990)

Another way in which accretion correlates with ejection is the fact that as accretion rates decrease as the young star evolves, so does outflow activity. For instance, Class 0 exhibit powerful ejections of matter and all of them have well collimated jets. The picture is however different at later evolutionnary stages. The correlation between the two phenomena is also statistically quantified. A survey of optical and molecular sources in the Taurus-Auriga molecular cloud complex, carried out by Gomez, Whitney, & Kenyon (1997), shows that jets are present in all Class 0 sources, in 60% of Class I sources, and only 10% of Class II sources. Gomez, Whitney, & Kenyon (1997) didn't find any jets in Class III objects.

According to Cabrit (2009), the thurst for this mass low may require a net energy deposit of $0.3L_{\mathrm{acc}}$, but due to losses related to dissipation and waves divergence, much more needs to be injected at the base of the wind.

1.2.5 Dynamics of the collimation

The opening angle of a ballistic hydrodynamic flow is $\tan\dfrac{\theta}{2} = \dfrac{c_s}{v_j}$, which corresponds, for a temperature of 10^4K and typical jet velocities of $300\,\mathrm{km\,s^{-1}}$ to an full opening angle $\theta \approx 4°$, which is comparable to observations. (Cabrit, 2007, Ferreira, 2009) For example, Perrin & Graham (2007) report an opening angle of 9°, for average radial outflow velocity of $100\,\mathrm{km\,s^{-1}}$, again consistent for a ballistic hydrodynamic flow with temperature of 10^4K $(c_s = 9.1\,\mathrm{km\,s^{-1}})$.

The collimation and ejection speeds vary not only with age, but also with the masses of the outflows. We indeed expect that there should be a difference between fully convective T Tauri stars and more massive stars with fully radiative interiors. The magnetic fields, driving the outflows, are much smaller in the case of massive YSOs, and as Shepherd *et al.* (1998) report, jets from high-mass YSOs are much less collimated with opening angles

of $30° - 60°$. An order-of-magnitude difference in the collimation factors (defined as the ratio between the width of the outflow to the distance to the driving source) is reported by Beuther *et al.* (2002), who give collimation factors of 1–2 for high mass outflows, while low mass sources have outflows with collimation factors of up to 10.

Molecular outflows observations, both from low- and high-mass YSO, mostly CO tracing molecular hydrogen, show that there is a mass-velocity relation, which could also be used to compare different observations and is relevant to radiative jets simulations. Explicitly written this relation is a power law: $\frac{dM}{dv} \propto v^{-\gamma}$ with γ from 1 to 3, but up to 10 in some cases, with the steeper slopes at high velocities. This slope steepens with the mass and the energy of the flow. (Arce *et al.*, 2006, and references therein)

1.2.6 The jet launching zone

1.2.6.1 Jet launching mechanism

The disk launching mechanism is unclear, but there is a consensus on the fact that magnetic forces are at the base of the ejection mechanism, together with thermal and centrifugal forces of the star-disk system. (Arce *et al.*, 2006, Ferreira, Dougados, & Cabrit, 2006, Königl & Pudritz, 2000, Shu *et al.*, 2000)

The canonical model of Blandford & Payne (1982) introduces the idea of a magneto-centrifugically driven disk wind. It consists of considering a disk, with magnetic fieldlines, which could be seen as 'wires,' rooted in the disk. Because of the rotation of the whole star-disk system, particles, seen as 'beads', are constrained to move along the almost vertical (but inclined) magnetic fieldlines, and are ejected by the disk. This 'bead-on-a-wire' analogy is a popular way to explain the launching mechanism of disk winds. This mechanism has its General-Relativistic generalizations, aiming to explain activity of active galatic nuclei. A plethora of papers,

discussing or developping this model are published since then, *e.g.*: Contopoulos & Lovelace (1994), Ferreira (1997), Salmeron, Königl & Wardle (2011), Tzeferacos *et al.* (2009).

Another models, as Sauty & Tsinganos (1994), discuss, among other models, thermally driven collimated stellar winds. As discussed in §3.5, the heating needed for the thermal drive could come either from dissipation of Alfvén waves, produced in the convection zone, could be changed by radiative transfer, or as Matt & Pudritz (2005) suggest, could be deposited by accretion.

However, the complex morphology of the observed outflows could not be explained solely by stellar winds or disk winds. As Lee *et al.* (2000, 2001, 2002) point out, there is evidence that there is a superposition of two components: a stellar jet and a disk wind. In the optical, the forbidden emission lines profiles of TTS show two velocity components: high-velocity, identified as a stellar jet and low-velocity, identified as a disk-wind.

Finally, a third class of models consider possible periodic ejections, due to the interaction of the magnetosphere of an YSO with the unmagnetized accretion disk. This could be either the X-wind of Shu *et al.* (1988), (Cai, 2009), the similar 'ReX', for 'Reconnection X-wind' of Ferreira, Pelletier, & Appl (2000) or the magnetospheric ejections, described by Zanni (2009).

The need of MHD in order to adequatly describe jet launching and collimation is also well-established. We will remind the basic arguments for the need of MHD for the study of collimated outflows, and for a more detailed discussion the reader is referred to lectures by Cabrit (2007) and Tsinganos (2007).

One obsolete hypothesis on the collimation of outflows is that an isotropic stellar wind is confined by an α-disk thermal pressure. Barral & Canto (1981) show that even if this mechanism can produce collimated outflows in the equatorial plane, where the accretion disk is present, the opening angle of the emerging flow above the accretion disk will be far too large for the flow to be considered as a jet. Then, this argument could be extended, and

the existence of an external pressure agent, above the α-disk, collimating the flow, could be speculated. This could be either a thermal pressure of the ambient medium or external magnetic pressure. Both mechanisms require by far too large thermal energy density, or far too large magnetic fields, failing to match the observations.

The self-collimation of jets, *i.e.* the collimation of the outflow by the YSO's own magnetic field, appear to be the process requiring physically plausible values for the magnetic field. In the case of equipartition of energy at the flow base, the magnetic fields needed to achieve self-collimation are of the order of $\approx$ 200mG, orders of magnitude smaller than an external collimating magnetic field. A magnetic field, producing collimation, could be nearly isotropic near the stellar surface. In the regime of low plasma β, the material coming out of the star will travel along magnetic fieldlines (the inertia of the fluid will not be sufficient to deform the fieldlines and the magnetic field will keep its near-to-vacuum configuration), until it reaches the Alfvén surface, where poloidal velocity equals the Alfvén speed. Beyond the Alfvén surface, the kinetic fluid energy starts to dominate the magnetic energy density. As a result, the inertia of the fluid deforms the shape of the magnetic field lines. A strong B_ϕ is generated, and strong hoop stresses as a result, exerting a confining force towards the axis, collimate the magnetic flux surfaces. However, as Mestel (2012) points out, it is not correct to think as the magnetic hoop stresses collimating alone the flow, actually the flow is collimated by the joint action of magnetic hoop stresses and material stresses. The particularity of the self-collimation we just described is that this process, as we mentionned, needs orders of magnitude smaller magnetic field. This is because B_ϕ collimates the outflow, and not external magnetic pressure in the poloidal plane. (Arce *et al.*, 2006, Cabrit, 2007, Ferreira, 2007, Tsinganos, 2007)

To measure the magnetic field, Zeeman splitting measures are commonly used. (Hartigan, 2009) Magnetic fields tend to remain helical at jet propagation scales, as reported by Chrysostomou, Lucas, & Hough (2007) for the case of HH 135-136.

1.2.6.2 Extent of the jet launching zone

Different sizes of the jet-lauching zone put constraints on different outflow scenarii. For instance, different sizes of the jet launching zone could rule out different disk wind scenarii. (Ferreira, Dougados, & Cabrit, 2006) The size of this zone could be deduced by two ways. By measuring jet expansion with respect to distance from the central source, and then extrapolating back from the resolved area back to the central source, Hartigan, Edwards, & Pierson (2004) found that the jet of HN Tau originate in less than 5.5 AU from the source.

The second way of determining the extent of the zone is to deduce it from rotation. As derived by Pelletier & Pudritz (1992), there is a direct link between the accretion and mass loss rates/total angular momentum and the ratio of the magnetic lever arm to the footprint radius of the wind, $\frac{\dot{M}_{\text{jet}}}{\dot{M}_{\text{acc}}} = \left(\frac{\varpi_A}{\varpi_0}\right)^2$. If the velocity gradients across the axis, observed by Bacciotti *et al.* (2000) are indeed interpreted as rotation (see §1.2.8 for discussion), Anderson *et al.* (2003) deduce $\varpi_0 < 3\,\text{AU}$ for the external part of the collimated jet of DG Tau.

1.2.7 Future observations of the jet-launching zone

The main difficulty on the observation of the jet lauching zone comes from the fact that central sources are often heavily embedded, hence we do not have a clear line of sight to the base of the jet. Besides this fact, the angular resolution needed to observe the jet launching is very high. At its most suitable working configuration, at wavelenght $\lambda = 7mm$ and at the most extended antenna configuration, the synthesized beam of the VLA observatory (equivalent of point spread function for radio observations) is 40 miliarcseconds, which corresponds, if we look at the Taurus-Auriga or Ophiucus molecular cloud complexes ($d \approx 140\text{pc}$), to the size of the orbit of Jupiter ($\approx 5\text{AU}$) (Wilner & Lay, 2000). The HST/adaptive optics seeing corresponds to a linear size of 125AU in the Taurus-Auriga complex.

As we discussed in §1.2.6, the jets are launched at smaller scales, thus with the advent of the ALMA telescope, with its maximal resolution of 5 miliarcseconds, hence $\approx$ 0.7AU at the Taurus-Auriga distance, (Belloche, 2013) these regions will be resolved. Moreover, as Beuther *et al.* (2002) point out, high-angular resolution observations are needed in order to disentangle the outflow contribution in the overall emission of the observed object from the emission of the central source.

1.2.8   Observations of rotation

In order to constrain better the jet-launching mechanism, more detailed and high-resolution observations of jet rotation near the central driving source, are still needed. Rotation at propagation scales $(2 \times 10^3 - 10^4 \mathrm{AU})$ is observed by Davis *et al.* (2000), but this does not put much constraint on the jet rotation, because the velocity field is 'contaminated' by strong interaction with the environment. It still provides some valuable information on jet physics. Rotation of outflows is also reported in high-mass YSOs, Herbig Ae/Be stars, as reported by Klaassen *et al.* (2013), who detect a rotating disk wind in the Herbig Ae star HD 163296.

Doppler-shift spectral observations of rotation in low-mass YSO jets need, first, high spectral resolution, and second, should disentangle effects, due to rotation, from other systemics, relative orbital motion, effects, induced on the spectrum by physical processes such as magnetospheric accretion (Edwards, 1997), among others.

In the early 2000s, Bacciotti *et al.* (2002) reported for a first time detection, with the STIS instrument of the HST, of velocity gradient across the jet axis in the first 110AU from the central driving source. Later, those findings where confirmed by Coffey *et al.* (2004). If this gradient is effectively caused by jet rotation, it results in toroidal velocities of DG Tau fall in the range $6 - 15 \mathrm{km\,s^{-1}}$, which results in angular momenta by far too large to be considered are produced by X-winds. Moreover, Coffey *et al.* (2004) show that some of the jets, like the jet of RW Aur, are counter-rotating with

respect to their accretion disks. Cai (2008) argue that this questions the interpretation of this velocity gradient as true rotation. On the theoretical side, Sauty *et al.* (2012) argue that counter-rotation of jets is possible in MHD. Moreover, this flip of toroidal velocity, they argue, might be due to post-ejection shocks, as proposed by Fendt (2011). Soker (2005) claim that the Bacciotti *et al.* (2002) and Coffey *et al.* (2004) papers do not detect rotation, but that the observed velocity gradient is due to the interaction of the jet with the surrounding gas. With the advent of high-resolution instruments as ALMA, we should be able to firmly verify or reject claims for jet rotation. (Belloche, 2013)

Chapter 2

The equations of ideal MHD and a self-similar model for jet-like flows

Contents

Chapter Abstract

The goal of this chapter is to list the fundamental equations of Magneto-hydrodynamics, which is the mathematical framework within which jets of Young Stellar Objects are studied. As it is well known, proving the existence of globally-regular, exact solutions of the Navier-Stokes equations, even without introducing electromagnetic fields, is a formidable, unsolved problem in Mathematics. However, in some simple cases, when symmetry considerations and approximations simplify the problem, analytical, or semi-analytical solutions exist. In this work, we give a brief presentation of the approaches, used in order to address the problem of studying jets of YSOs, which consists in making the corresponding hypothesis and approximations in resolving the set of equations of ideal MHD. By this we mean that we will remind which conserved quantities exist in the case of stationary, axisymmetric outflows, and then we will discuss the self-similar hypothesis, allowing, by physically plausible symmetry considerations, to reduce the set of partial differential equations of MHD to a set of ordinary differential equations. Finally, we will discuss a self-similar ansätz, used in order to obtain, by a proper integration of the differential equation resulting from the self-similar hypothesis, the values of the relevant physical quantities density, pressure, magnetic and velocity fields. Meanwhile, we also discuss the velocities at which waves propagate in a MHD system. This is useful, for instance, if we want to know if a given point within the system under consideration is influenced by a given boundary condition.

2.1 On the ideal MHD approach for jets of YSOs

As we discussed in the previous chapter, magnetic fields are supposed to play a dominant role in the evolution of Young Stellar Objects. Hence, in order to correctly describe the evolution of matter around an YSO, we need to study the coupling of matter with the magnetic field. In this work,

we will operate in the framework of ideal MHD, which means that we are studying the flow of an perfectly condicting, highly collisionnal inviscid fluid, with negligible viscosity, and on scales much bigger than the typical scales involved in the problem. In the case of low densities, the strong coupling of the magnetic field to matter ensure the validity of the MHD approximation. Moreover, in MHD we operate with the important basic parameters such as the temperature T, pressure P, density ρ, magnetic field $\mathbf{B}$ and velocity field $\mathbf{V}$, which are quantities that could be deduced by observations of jets of YSOs. We will indeed make a concise verification that we could operate in the framework of ideal MHD, which concretely means that we will check that the typical lengths for the systems we are studying (jets of YSOs) are much larger **(a)** than the collisional mean free path of the particles, which in its turn is much larger than **(b)** the Debye length. We will verify that **(c)** the mean collision interval is much longer than the ion gyration time and the electron gyration time, and finally **(d)** we will remind the values of electrical, thermal conductivity and viscosity in such astrophysical plasmas. The discussion that follows will be similar to those in Fendt, Camenzind, & Appl (1995), Mestel (2012), Tsinganos (2007).

(a) In the case of Coulomb scattering by electrons by ions, we have for the value of the mean free path:

$$\lambda_{ei} \approx \frac{4k_B^2 T^2}{9\pi Z^2 n_i e^4} \approx 5 \times 10^4 \frac{T^2}{Z^2 n_i}, \tag{2.1}$$

hence a mean collision interval of

$$\tau_{ei} = \frac{\lambda_{ei}}{(v_{th})_e} \tag{2.2}$$

With $(v_{th})_e = \sqrt{\dfrac{k_B T}{m_e}}$ the thermal velocity of the electrons, k_B the Boltzmann's constant and e the charge of the electron. In the case of a hot, pure hydrogen (Z=1), tenious plasma, like the matter in the

solar corona, we have $T \sim 10^6$K and $n \sim 10^8$cm^{-3}, which results in:

$$\lambda_{ei} \approx 5 \times 10^8 cm = 5000 \text{km} \tag{2.3}$$

which is much less than the tenth of the astronomical unit (0.1AU $=$ 1.496×10^7km);

(**b**) For the validity of the plasma approximation, we also need that enough electrons are contained within the Debye sphere, *i.e.* that a given electron influences not only its closest neighbour, but also a statistically significant number of charged particles. The Debye length, which is the radius of the Debye sphere, is the distance over which the influence of a given charge is screened, *i.e.* we have effective 'charge separation.' This length is given by:

$$\lambda_D = \sqrt{\frac{k_B T}{4 \pi n_e e^2}} \approx 6.9 \sqrt{\frac{T}{n_e}}. \tag{2.4}$$

For the same parameters as we used to compute the other lengths, this yeilds λ_D of the order of a cm, much smaller than the mean free path of Coulomb scattering.

(**c**) In the simplest approach, the gyrofrequency of a single particle of charge Ze and mass m_x in a uniform magnetic field **B** is $\omega_g = \dfrac{ZeB}{m_x c}$. We have, for ions (with mass Am_p) and electrons, respectively:

$$\frac{2\pi}{\tau_i} = \omega_i = \frac{ZeB}{m_p c} = 10^4 \frac{Z}{A} B \tag{2.5}$$

$$\frac{2\pi}{\tau_e} = \omega_e = \frac{eB}{m_e c} = 2 \times 10^7 B \tag{2.6}$$

This has to be compared to the mean collision time, which expression is given in (**a**):

$$\frac{\tau_{ei}}{\tau_e} \approx 1.75 B \frac{T^{\frac{3}{2}}}{n} \gg 1, \tag{2.7}$$

if we take the same parameters as above and a magnetic field $B \sim$ 1 kG. Therefore the Larmor radius $r_L \ll \lambda_{ei}$.

(d) As Tsinganos (2007) reminds, the thermal conductivity is very high $\chi \approx 6 \times 10^8 \mathrm{g\, cm^{-1}s^{-1}}$, the electrical conductivity is comparable to that of excellent conductors like copper ($\omega_{Cu} \approx 10^{16} \mathrm{s^{-1}}$), and the viscosity ($\mu \approx 0.1 \mathrm{g\, cm^{-1}s^{-1}}$) negligible.

In conclusion, with this arguments together, we can argue that the ideal MHD approximation is a good approximation for the description of the overall behaviour of stellar outflows.

2.2 Conservation of mass, momentum, energy and the induction equation

The set of equations of ideal MHD consists of 8 equations, which is required to obtain a solution giving the 8 MHD quantities, namely density, velocity, magnetic field, and pressure, which in usual notation are written ρ, $\mathbf{V}$, $\mathbf{B}$, and P, respectively. Those equations are:

$$\frac{\partial \rho}{\partial t} + \nabla \cdot (\rho \mathbf{V}) = 0 \tag{2.8}$$

$$\frac{\partial \mathbf{V}}{\partial t} + (\nabla \cdot \mathbf{V})\mathbf{V} + \frac{1}{\rho}\frac{1}{4\pi}\mathbf{B} \times (\nabla \times \mathbf{B}) + \frac{1}{\rho}\nabla P = -\nabla \Phi \tag{2.9}$$

$$\frac{\partial P}{\partial t} + \mathbf{V} \cdot \nabla P + \Gamma P \nabla \cdot \mathbf{V} = H - \Lambda \tag{2.10}$$

$$\frac{\partial \mathbf{B}}{\partial t} - \nabla \times (\mathbf{v} \times \mathbf{B}) = 0 \tag{2.11}$$

where $H - \Lambda$ is the energy equation source term, representing the volumetric energy gain/loss terms, Φ is the gravitational potential of the central object ($\Phi = -\mathcal{G}\mathcal{M}/r$), where $\mathcal{M}$ is the mass of the central object, and the gravitational constant $\mathcal{G} = 6.67259 \times 10^{-8} \mathrm{cm^3 g^{-1}s^{-2}}$. Units are usually expressed in CGS system.

The first equation is the mass conservation equation, relying the time derivative of density with the spatial derivative of the linear momentum.

The second equation is the momentum equation, relying time derivative of momentum with the energy flux. The third equation is the energy conservation, on which RHS we have the heating/cooling term. Finally, the last equation in this set is the induction equation, governing the coupling between the velocity and the magnetic field. This form appears to be useful for writing down the discretisation of these equations, in order to attempt a numerical resolution of the set of equations. For more details on this last point, the reader is referred to Mignone *et al.* (2007), where is presented the PLUTO code that we will be using in this work to carry out numerical simulations.

2.3   Magnetohydrodynamic waves

If we want to study how a particular point in the interior of our MHD system is affected by another point, or a boundary, we should know if the information had time the to travel between the two regions in question. In order to know this, we should know at which velocity a perturbation will travel across the system. In a pure hydrodynamical system, perturbations travel at the sound speed:

$$c_s = \sqrt{\frac{\partial P}{\partial \rho}}. \tag{2.12}$$

The picture is a bit more complicated in magnetized fluids. In order to find modes of propagation of waves in MHD systems (called *Magnetosonic modes*), we should look for plane-wave solutions of Eqs. (2.8-2.11), i.e. solutions $\propto e^{i(\mathbf{k}\cdot\mathbf{r}-\omega t)}$, where $\mathbf{k}$ is the wave vector; $\mathbf{r}$ the position vector and ω the wave frequency. A detailed derivations of eigenequations of these modes in given in most MHD textbooks (e.g., Blandford & Thorne, 2012), so we will directly remind the dispersion relations for the different modes. A characteristic speed in MHD systems is the Alfvén speed:

$$\mathbf{v}_a = \frac{\mathbf{B}}{\sqrt{4\pi\rho}} \tag{2.13}$$

which is the speed of magnetosonic waves, propagating along the magnetic fieldlines. The full dispersions relations for the magnetosonic modes are:

$$\omega = \pm\mathbf{v}_a \cdot \mathbf{k}; \quad \frac{\omega}{k} = \pm v_a \cos\Theta \tag{2.14}$$

and

$$\left(\frac{\omega}{k}\right)^2 = \frac{1}{2}\left(v_a^2 + c_s^2\right)\left\{1 \pm \left(1 - \frac{4c_s^2 v_a^2 \cos^2\Theta}{(v_a^2 + c_s^2)^2}\right)^{\frac{1}{2}}\right\} \tag{2.15}$$

Note that Θ is the angle between the wave vector $\mathbf{k}$ and the unperturbed magnetic field $\mathbf{B}$, and should not be confused with θ, which is the polar angle in the spherical coordinate system.

One magnetosonic mode, described by Eq. (2.13) is the *Alfvén mode*, called also *Intermediate mode*. As it can be seen in Eq. (2.13), this mode does not propagate in directions perpendicular to the magnetic field. In the limiting case of a wave propagating purely in the direction of $\mathbf{B}$, longitudinal oscillations of the perturbation propagate with the Alfvén speed. The magnetic field tension $(\mathbf{B}^2/2\pi)$ acts as a restoring force. This mode does not induce any pressure or density fluctuations.

The dispersion relations of the two other magnetosonic modes are given in Eq. (2.15). The mode with the minus sign in Eq. (2.15) is called the *slow magnetosonic mode* and the one with the plus sign: *fast magnetosonic mode*. Those modes induce a combination of magnetic pressure, magnetic tension and gas pressure fluctuations. As it can be seen from Eq. (2.15), the fast magnetosonic wave is fastest when the perturbation is propagating in direction perpendicular to the magnetic fieldlines. In this case, the fast mode can be seen as analogous to transverse sound waves, which propagate in gas to which usual pressure P is added the magnetic pressure $\left(\dfrac{\mathbf{B}^2}{8\pi}\right)$.
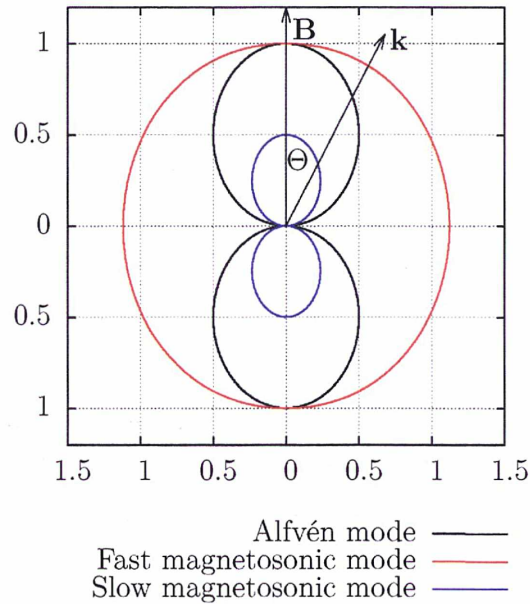
FIGURE 2.1: Magnetosonic waves phase velocity (see Eqs. 2.13 and 2.15) polar plot (Friedrich diagram). The direction of the magnetic field **B** and the wave vector **k**, as well the angle between them, Θ are also plotted. In this sample plot, $c_s = v_a/2$ and $v_a = 1$.

The three magnetosonic modes are plotted on Fig. 2.1. What will be relevant to discussions in subsequent chapters is the fact that the fast magnetosonic waves are the fastest waves. Moreover, this mode is the only mode that can propagate information in directions, perpendicular to the magnetic fieldlines. Hence, the maximal speed at which information can propagate in MHD systems along the flow/magnetic fieldlines is the fast magnetosonic speed plus the bulk velocity of the flow, and simply the fast magnetosonic speed for information propagating in direction perpendicular to the flow/magnetic fieldlines. What we will note is that there is no way for information to propagate upstream if the flow is superfast (i.e. which bulk velocity is greater than the local fast speed.)

2.4 Conserved quantities for steady-state and axisymmetric solutions

After the very general discussions we had in the two previous sections, we remind that we are interested in the theoretical modelling of jets. Before discussing any particular model, we will point out that in ideal MHD, under quite general assumptions, which are stationarity and axisymmetry, Tsinganos (1981) shows that several quantities are conserved along field-lines. A direct consequence of the 'flux freezing' of ideal MHD is the fact that the magnetic flux is conserved along a fieldline. This conserved quantity, which is the mass-to-magnetic flux ratio, is noted Ψ_A:

$$\Psi_A(\alpha) = \frac{4\pi\rho \mathbf{V_p}}{\mathbf{B_p}}. \tag{2.16}$$

Hence, for a given line we have a given value of Ψ_A, which could be used to label the fieldline. The two other conserved quantities are the field angular velocity

$$\Omega(\alpha) = \frac{1}{\varpi}\left(V_\phi - \frac{\Psi_A B_\phi}{4\pi\rho}\right), \tag{2.17}$$

and the total specific angular momentum

$$L(\alpha) = \varpi\left(V_\phi - \frac{4\pi B_\phi}{\Psi_A}\right). \tag{2.18}$$

The combination of Eqs. (2.16) and (2.17) gives the velocity field:

$$\mathbf{V} = \Psi_A(\alpha)\frac{\mathbf{B}}{4\pi\rho} + \varpi\Omega(\alpha)\hat{\boldsymbol{\phi}}, \tag{2.19}$$

which expression is a generalisation of the Ferraro law (1937).

Thus, next to the origin, the second term in the expression will be negligible compared to the first term: the field will be practically radial. On long

TABLE 2.1: Coordinate variables description

r	Spherical distance from the origin
θ	Polar angle; $\theta = 0$ at the axis
r_*	At $(r_*, \theta = 0)$ the Alfvén surface crosses the axis
$R = r/r_*$	Dimensionless distance
$R_0 = 0.108$	One stellar radius
$R_* = 1$	The Alfvén radius. $R_* = 9.29 R_0$
ϖ	Dimensioneless cylindrical distance; $\varpi = (r/R_*)\sin(\theta)$
z	Cylindrical height
(ϖ, z)	The poloidal plane

distances, the second term will dominate the first one: the field will be practically toroidal and will encompass the flow. Equivalently, this could be seen as magnetic stress hoop and material stress collimating the flow.

The study of those quantities will be of physical importance. Verifying that these quantities are conserved along fieldlines will ensure that the steady state is reached. The interplay of those quantities will enable us to quantify the angular momentum extraction process. The quantity τ, which expression is:

$$\tau = \frac{\varpi B_\phi}{4\pi} - \Psi_A \Omega \varpi^2 \tag{2.20}$$

is the constant rate of transport of angular momentum across a unit flux tube (Mestel, 2012).

2.5 The self-similar model

Sauty, Tsinganos, Trussoni *et alii* study models of non-relativistic flows from young stellar objects in a series of papers (Tsinganos & Sauty (1992a),

Tsinganos & Sauty (1992b), Sauty & Tsinganos (1994), Trussoni *et al.* (1997), Sauty *et al.* (1999, 2002, 2004a,b), Sauty *et al.* (2011)), on which this work heavily relies. In particular, the solution we are going to study in the next chapter, and modify in susequent chapters, is first presented in Sauty *et al.* (2011).

The self-similar approach consists of supposing that there exist a solution of separable coordinates of the ideal MHD equations (Eqs. 2.8-2.11 in this text), which are already simplified by the assumptions of stationarity and axisymmetry. If we suppose that the magnetic flux varies with colatitude as a dipolar field, *i.e.* $\sim \sin^2(\theta)$, where θ is the polar angle (the notations we adopt for the various coordinates are described in Table 2.1), and some *a priori* unknown radial function $G(R)$, we could write it in the separable form:

$$\alpha = \frac{R^2}{G^2} \sin^2(\theta), \tag{2.21}$$

This function $G(R)$ is related **(a)** to the expansion factor $F = F(R)$, which definition we will give, and **(b)** to the magnetic lever arm for the given fieldline, which expression we are also going to give now:

(a) The function $F(R)$ is the 'expansion factor' of a given fieldline:

$$F = F(R) = 2 \left(1 - \frac{d \ln G}{d \ln R} \right). \tag{2.22}$$

For constant $F(R) = 2$, i.e. $G(R) = const.$, we have purely cylindrical fieldlines (all perpendicular to the equator) and $F(R) = 0$, i.e. $G(R) \propto R$ corresponds to a purely radial wind solution. Hence, $F(R)$ and $G(R)$ have geometrical meaning.

(b) If we introduce the magnetic lever arm ϖ_A for the given fieldline, we have

$$\varpi_A = \sqrt{\frac{L(\alpha)}{\Omega(\alpha)}}, \tag{2.23}$$

which allows us to discuss the physical meaning of the involved quantities. $G(R)$, which is the ratio of the cylindrical distance to the magnetic lever arm:

$$G(R) = \frac{\varpi}{\varpi_A}. \tag{2.24}$$

The functions $F(R)$ and $G(R)$ are *a priori* unknown functions and will be determined once the equations are integrated. Rewriting the ODE, resulting from the separation of variables, in terms of these functions, makes it easier to integrate. They are usually called 'key functions'. Another key function, which will allow us to compute density, once the equations are integrated, is the Alfvénic Mach number, i.e. the ratio of the poloidal velocity to the local Alfvén velocity:

$$M = \frac{V_p}{B_p/\sqrt{4\pi\rho}}. \tag{2.25}$$

By rewriting Eq. (2.25) for ρ, and by making self-consistent hypothesis for the form of V_p and B_p, Sauty & Tsinganos (1994) write density in the following form:

$$\rho = \rho_* \frac{1}{M^2}(1 + \delta\alpha) \tag{2.26}$$

In this equation, as intuitively could be understood by mass conservation reasoning, density is inversely proportionnal to the square of the Alfvén Mach number. The term in the parentheses is function of α only, hence it describes how the density varies from one fieldline to another. This variation is more or less pronounced if the constant free parameter δ is bigger or smaller. For $\delta = 0$ we have a density function depending only on R. For bigger δ we have bigger deviations from spherical symmetry. As we noted, $M^2(R)$ is *a priori* unknown function, it will be inserted in the equations, which will be solved for $M(R)$ and the other key functions. In a similar way, a full ansätz, describing the other quantities, could be

constructed. We are not going to discuss this in detail, the interested reader is referred to Sauty & Tsinganos (1994). In terms of the key functions, the three components of velocity have the following expressions:

$$V_r = V_* \frac{M^2}{G^2} \frac{\cos\theta}{\sqrt{1+\delta\alpha}} \tag{2.27}$$

$$V_\theta = -V_* \frac{F}{2} \frac{M^2}{G^2} \frac{\sin\theta}{\sqrt{1+\delta\alpha}} \tag{2.28}$$

$$V_\phi = \frac{V_*\lambda}{G^2} \frac{G^2 - M^2}{1 - M^2} \frac{R\sin\theta}{\sqrt{1+\delta\alpha}} \tag{2.29}$$

A key function, not introduced to this moment, is the dimensionless radial pressure distribution $\Pi(R)$, participating in the expression for the gas pressure:

$$P = P_*(\Pi(1 + \kappa\alpha) + \Pi_0), \tag{2.30}$$

where the dimensionmess parameter κ describes the departure from spherical symmetry for the pressure P. Finally, the expressions of the three components of the magnetic field are:

$$B_r = \frac{B_*}{G^2}\cos\theta, \tag{2.31}$$

$$B_\theta = -B_* \frac{F}{2} \frac{1}{G^2}\sin\theta, \text{and} \tag{2.32}$$

$$B_\phi = -B_* \frac{\lambda}{G^2} \frac{1 - G^2}{1 - M^2} R\sin\theta \tag{2.33}$$

2.6 Free parameters and normalized quantities

The constants ρ_* and V_* correspond to the characteristic values of the corresponding quantities on the Alfvén radius; $P_* = \dfrac{1}{2}\rho_* V_*^2$ and $B_*^2 = 4\pi\rho_* V_*^2$.

In Eq. (2.26) we define the constant free parameter δ; κ is defined in Eq. (2.30); λ in Eq. (2.29), and describes the rotation of the flow. The last free parameter of the self-similar model is ν, not defined in Eqs.(2.26-2.33), and its expression is:

$$\nu^2 = \frac{2\mathcal{G}\mathcal{M}}{r_* V_*^2} \tag{2.34}$$

where $\mathcal{G}$ is the gravitational constant and $\mathcal{M}$ is the mass of the central object and P_0 is an arbitrary constant. In this framework, δ and κ are deviations from spherical symmetry for the density and pressure, respectively; λ is the strength of the magnetic torque at the Alfvén radius R_*, and ν is the strength of the gravitational potential.

The approach is called semi-analytical, because once the ODEs, representing the force balance on a fieldline, are rewritten in terms of the key functions, the solution is not given in terms of known analytical functions, but is determined numerically, which is done in Sauty *et al.* (2011). A propagation scale plot of this solution could be seen on Fig. 3.1.

The ODE in question, describing the force balance along a given fieldline is called the transfield equation, studied for a first time by Grad & Rubin (1958) and Shafranov (1966), hence also named Grad-Shafranov equation. In a nutshell, the physical meaning of this is that we have the same physics on all fieldlines. Once we resolve the transfield equation for one fieldline, we can apply a scaled-up version of the solution on any other fieldline, following the 'recipe' which is Eq. (2.21). This is why the approach is called 'self-similar.'

Chapter 3

Stability of a particular solution: Axisymmetric analytical stellar outflow

Contents

Chapter Abstract

The goal of this chapter is to study the solution, derived in Sauty *et al.* (2011), in particular to determine whether it is structurally stable or not. First, in this chapter, we make use for a first time of the PLUTO code, which is a numerical code for modelling of 2.5 dimensions time-dependant MHD systems. Using a 2.5D approach means that the time evolution/fluxes in the MHD simulation box are computed in 2D, and the third component is deduced from conservation arguments. In this chapter, we implement the solution of Sauty *et al.* (2011), and set it up as an initial condition in our MHD simulation box. We find that this solution is topologically stable and that, globally, the eight MHD quantities keep their initial distributions. Finally we plot several quantities of physical interest and discuss the results of the simulation.

3.1 A solution with a particular set of parameters

Sauty *et al.* (2011) obtain a particular solution for a jet-like outflow. The interest of this solution is that it is modelling cTTS with low mass accretion rates. Those stars exhibits 'micro-jets', which means that the outflow is not emanating from the disk or is weakly connected. As a consequence, they have much lower mass loss rates. Those observed by Agra-Amboage *et al.* (2009), Gómez de Castro & Verdugo (2001), St-Onge & Bastien (2008) have typical $\dot{M} \sim 10^{-9} M_{\odot} yr^{-1}$). The solution, obtained by Sauty *et al.* (2011), which stability we are testing here, fits particularly well the case of the micro-jet of RY Tau.

From now on, we will call this solution "Cylindrical analytical stellar outflow" - CASO and the numerical setup we will use, except if the contrary is specified, will correspond to this particular set of parameters. An outlook
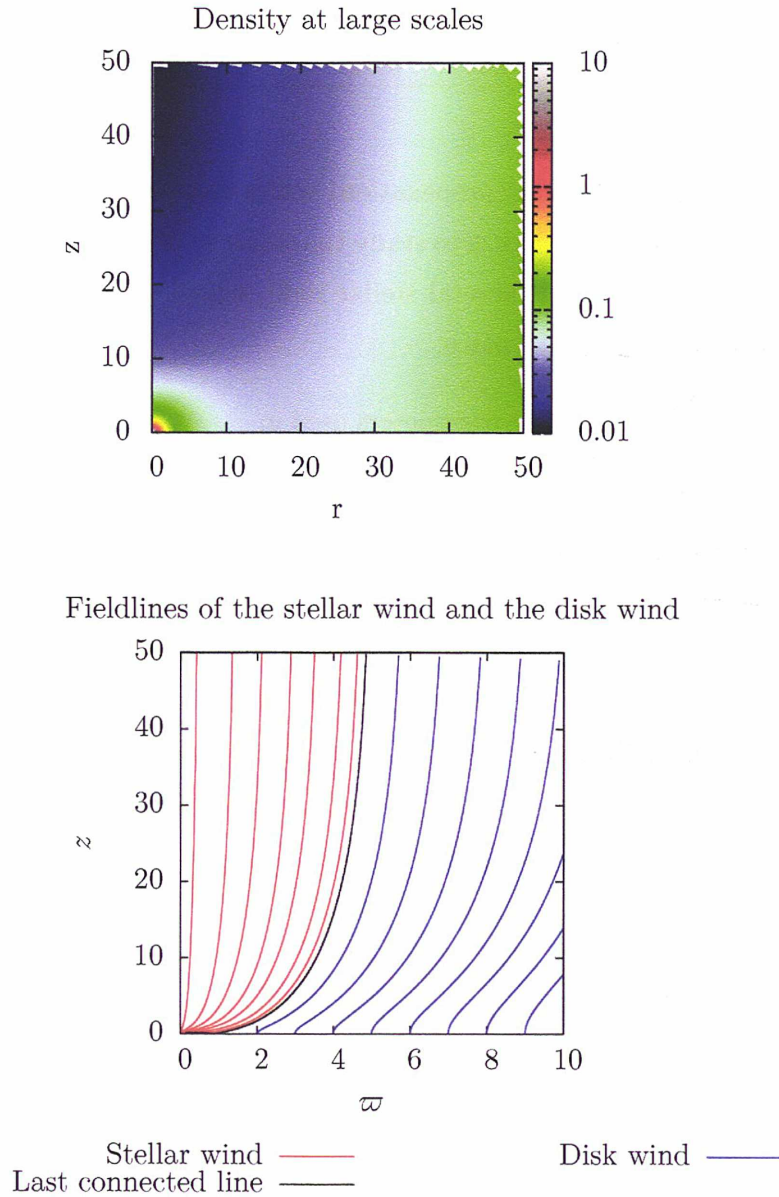
FIGURE 3.1: On the top panel, density in the poloidal plane normalized to the density at the Alfvén radius for the solution in Sauty *et al.* (2011), which set of free parameters is given in Table 3.1; On the bottom panel, lines of equal poloidal velocity (grey lines, numbers show the velocity on the corresponding line, normalized to the Alfvén speed). Two kinds of fieldlines are visible on this plots.First, fieldlines anchored to the star (for the stellar wind) and second, fieldlines anchored to the disk. Those are "disk-wind"-like outflow. Distances are normalized to the Alfvén radius.

TABLE 3.1: Numerical values of the free parameters of Sauty *et al.* (2011), corresponding to the ansätz in § 2.5.

δ	κ	λ	ν
0.0778	0.021	0.775	1.5

of this solution at large (propagation) scales can be found on Figure 3.1. The first goal of this work is to study the stability of this particular solution on small scales, i.e. at several stellar radii, where the jet collimation and initial acceleration take place.

The particular set of free parameters used in Sauty *et al.* (2011) and Globus (2011) are shown in Table 3.1.

This particular CASO solution is adapted to study the stellar wind: that component of the jet which is ejected by the star itself; and the mechanism by which the star accelerates matter along the fieldlines is thermally driven pressure gradient. This only corresponds to a star with low mass loss rate, because for high mass loss rates an unphysically high thermal input is needed for accelerate an important amount of matter. (Decampli, 1981, Sauty *et al.*, 2011) The question of the topological stability is not self-evident, since the flow is not polytropic (see Sauty & Tsinganos (1994), Sauty *et al.* (2011)). This is self-consistent with the goal of the study: as we investigate a thermally-driven stellar outflow, employing a non-polytropic heating function is essential, as explained in §3.5.

3.2 Initial and boundary conditions for the time-dependant simulation

In order to study the solution in the close vicinity of the star, where the initial acceleration and ejection take place, we set up a 2D simulation box with size $\left(R \in [0.2 : 2], \theta \in \left[0 : \dfrac{\pi}{2}\right] \right)$. For the boundary conditions setup, we follow procedures, similar to those in Gracia *et al.* (2006)

and Matsakos *et al.* (2008, 2009). On the inner boundary of the box, which is close to the stellar surface, we initialize a stellar wind outflow, given by the semi-analytical model of Sauty *et al.* (2011). We apply the same procedure on the equator. For the axis, we choose the 'axisymmetric' boundary treatment of PLUTO. Now, a problem arises on the outer boundary. We might use the 'outflow' boundary condition in PLUTO, which copies the value of the last cell in the ghost zone for a given radial direction, *i.e.* it is a zero-gradient boundary condition. This is problematic, since this zero-gradient might generate artificial currents. Linear extrapolation of the values of the last cells might generate a similar problem. The solution we adopt is to drastically increase the size of the box, $\left(R \in [0.2 : 2], \theta \in \left[0 : \frac{\pi}{2}\right]\right) \rightarrow \left(R \in [0.2 : 340], \theta \in \left[0 : \frac{\pi}{2}\right]\right)$, in order to be sure that waves, coming out of the surface $R = 2$ quit definitely this region and that waves, generated downstream, particulary in the outer boundary at $R = 340$, will not propagate back to the central part. This cannot happen, because, as we will discuss in this section, the outflow is already superfast in this region, and perturbations cannot travel upstream a superfast flow. One particular feature of the simulation box we set up is that as we want to keep the numerical resolution high in the region $R \in [0 : 2]$, we set up a mesh with 384 pixels, equispaced in the region $R \in [0 : 2]$, and 128 pixels of streched, logarithmic grid in the region $R \in [2 : 340]$. Hence, we conjecture that we can set up any boundary condition at $R = 340$, and information from this boundary will have no time to propagate back to the central source.

In order to verify the last affirmation, we plot, in Appendix A for this solution, the changes in all eight MHD quantities between the final and the initial state. What we see in Appendix A is that the final state is different from the initial state on isolated regions far from the region ($R \in [0.2 : 2]$ that interests us. Thus, we *a posteriori* verify that the central region is causally disconnected from the outer boundary. We have also an *a priori* argument that information from the outer boundary cannot travel to the central source. First, close to the axis, the flow is vertical and information

cannot travel upstream a superfast flow. In order to verify that the flow is superfast, we plot the sonic speed (c_s, Eq. 2.12) and the Alfvén speed (v_a) close to the axis on Figure 3.2. To plot c_s, we first plot P as a function ρ and then take the centered derivative $\left(\dfrac{dP}{d\rho}\right)$. Then, we could also plot the fast speed, according to Eq. 2.15, but as could also be seen on Fig. 3.2, $c_s \ll v_a$, for $R > 0.21$, so Eq. 2.15 becomes $v_{\text{fast}} \approx v_a$. Indeed, if we plot it, the graph of v_{fast} is identical to v_a, except very close to $R = 0.2$ (the inner boundary). Hence, we conjecture that the superfast surface, where the transfield equation changes nature and passes from elliptical to hyperbolical (Beskin, 2010, Tsinganos, 2007) coincides with the Alfvén surface. The problem with this argument is that, as Tsinganos (2007) points out, in the case of self-similar solutions, the sonic speed cannot be readily defined. This is because of singularities of the type $\dfrac{0}{0}$ in the transfield equation. In order to integrate the transfield equation, some regularity conditions, selecting only solutions passing smoothly through the Alfvén point, should be imposed. We are not going to enter into the detail of this integration, but the point, relevant to this discussion is as those Heyvaerts & Norman regularity conditions (1989) are imposed at the Alfvén point, so we pretend that the plot of the sonic speed on Fig. 3.2 in the vicinity of the Alfvén point should be the actual sonic speed. This cannot be affirmed for points far from the Alfvén point.

However, unlike slow and Alfvén waves, the fast waves can also propagate in directions, perpendicular to the magnetic field (*e.g.*, see the Friedrich diagram on Fig. 2.1). We again conjecture that fast waves, generated at the outer boundary close to the equator, have no time to propagate back to the central part, because of the size of the box. In the previous discussions, we discussed waves, propagating along the radial direction, which means, when we are close to the axis, and parallel to the equator, when we are close to the equator. As Tsinganos *et al.* (1996) discuss, MHD waves preserving the symetries of the system should have velocity components perpedicular to the directions of symmetry (ϕ) and self-similarity (θ), *i.e.* along r. Those

symmetries are supposed to derive the semi-analytical solution, but the self-similarity condition is relaxed in the numerical setup. But as we are going to show, the MHD quantities keep their initial distribution, *a fortiori* the self-similar condition should also be kept, so interesting us only in waves propagating along r in the previous analysis will be justified *a priori*.

3.3 Topological stablity of the solutions

Matsakos *et al.* (2008, 2009) have found that a large number of self-similar solutions, obtained by varying the free parameters in the solutions above, are "topologically stable" at large (propagation) scales. This means that when we initialize a MHD simulation box with the solution above as an initial condition, and we let a MHD code compute the time evolution of this initial condition, the eight MHD physical quantities might keep or not their initial distribution, but from the initial distribution the quantities converge to a steady state. This corresponds to the discussed notion of topological stability.

3.4 Time units

To describe the time evolution, we will prefer to express the time in units of Alfvén crossing time, i.e. the time needed for a characteristic to cross an Alfvén distance close to the base of the flow. This time could be related to the disk rotation time (by reminding the definition of ν in eq. 2.34):

$$t_{\text{Kep}} = 2\pi \sqrt{\frac{r_*^3}{\mathcal{G}M}} = \frac{2\pi}{\nu} \sqrt{\frac{2r_*^2}{V_*^2}} \tag{3.1}$$

As the starred quantities are taken to be unity at the reference radius R_*, by replacing the constants with their numerical values in Eq. (3.1) we obtain

Comparison of the poloidal speed in the axis and characteristic speeds
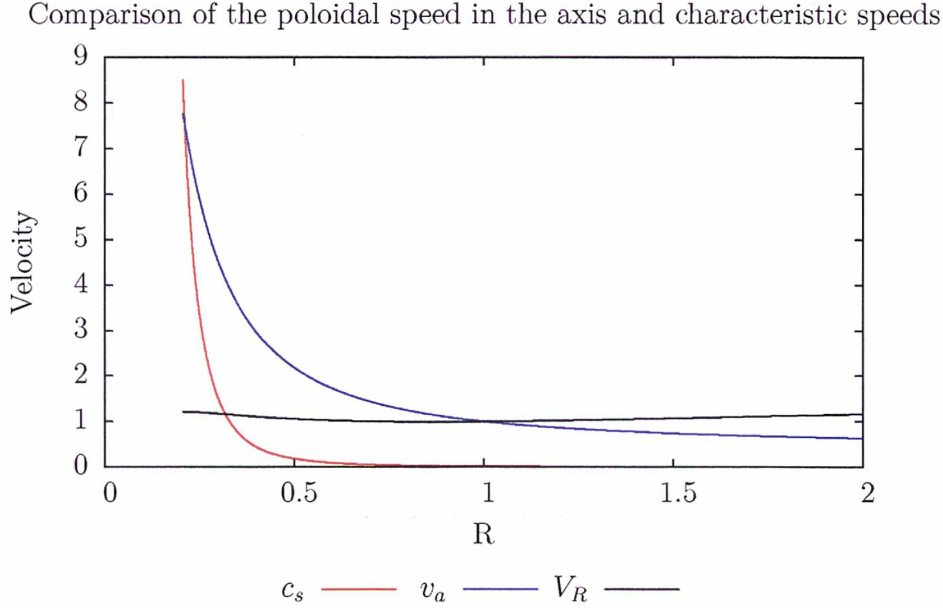
FIGURE 3.2: Comparison of the sonic and Alfvén speed with the radial velocity.

the Keplerian time in units of the Alfvén crossing time for this particular solution:

$$t_{\text{Kep}} = 5.92 t_* = 5.92 \sqrt{\frac{2 r_*^2}{V_*^2}} \tag{3.2}$$

We stress that we prefer to express time in units of the Alfvén crossing time, since the CASO solution is a thermally driven outflow and not a magnetocentrifugically driven disk wind.

3.5 Heating distribution

By writing the expressions for the density (Eq. 2.26) and pressure (Eq. 2.30), under the self-similar hypotheses, we do not make the assumption that an *a priori* relation exists between those two quantities. Instead of a relation of the type $P \sim \rho^\gamma$, self-similarity puts not necessarily polytropic

Density contours and fieldlines, initial condition
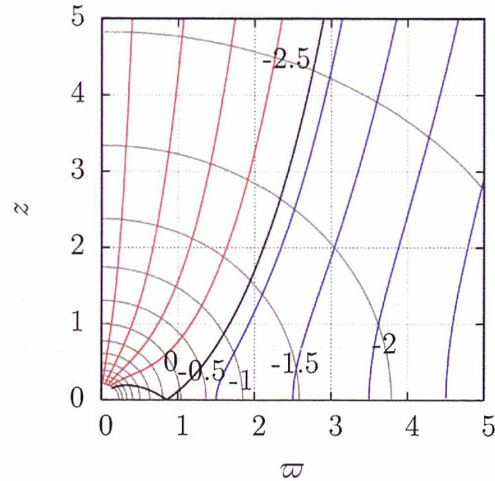
$\log(\rho)$ ———	Last connected line ———
Stellar wind ———	Disk wind ———

Density contours and fieldlines, initial condition
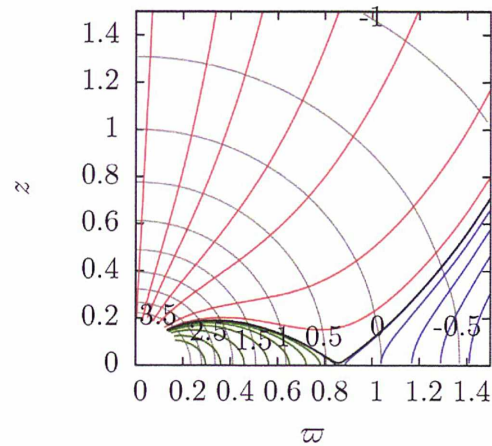
$\log(\rho)$ ———	Last connected line ———
Stellar wind ———	Disk wind ———
Dead zone ———	

FIGURE 3.3: Fieldlines and density contours for the CASO solution. The bottom panel is a zoom of the top panel, showing closed fieldlines (in green). Fieldlines in blue are rooted in the star, and describe the stellar wind and fieldlines in red are anchored in the disk, describing an outflow from the disk. The last connected line (which for $r < 0.85$ is also a "last connected fieldline" is a thick black line).

Heating distribution
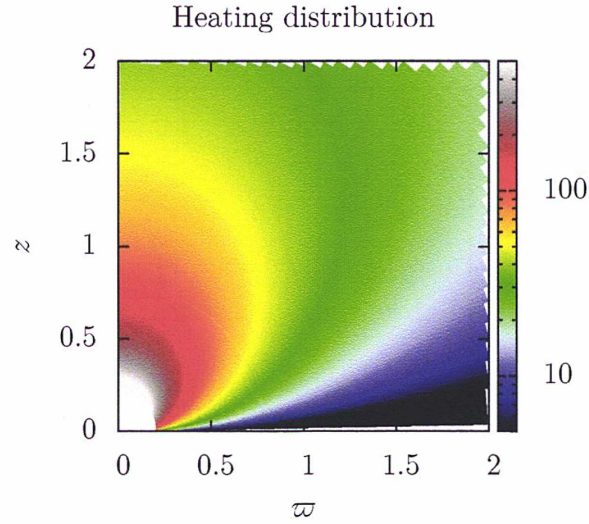
FIGURE 3.4: Heating distribution

constraints on the $P - \rho$ relation, which relation emerges a posteriori from the mathematics. With the first law of thermodynamics, we can quantify the departure from adiabaticity with a flow with the current geometry:

$$H - \Lambda = \rho \mathbf{v} \cdot \nabla h - \frac{P}{\rho} \mathbf{v} \cdot \nabla \rho \tag{3.3}$$

where the volumetric enthalpy h is a function, obviously independant of any relation between P and ρ,

$$h = \frac{\Gamma}{\Gamma - 1} \frac{k_B}{\mu} T = \frac{\Gamma}{\Gamma - 1} \frac{P}{\rho}, \tag{3.4}$$

with Γ the ratio of specific heats in the gas, $\Gamma = \dfrac{c_p}{c_v}$ and μ the mass of the gas. The resulting heating distribution, computed from Eq.(3.3), taking into account Eqs.(2.26-2.29), is plotted on Fig. 3.4.

Hence, we have a heating function, suitably distributed in order to satisfy the energy equation (Eq. 2.10) and maintain the steady state. Most importantly, this heating function is non-polytropic. As Sauty *et al.* (2002) argue, this heating function could be of thermal or another origin. One might argue that such a relation between P and ρ, computed *a posteriori*, is no better than any other relation. For instance, such a relation could be the polytropic assumption $P = \rho^\Gamma$, or the quasi-polytropic relation $P = \rho^{\Gamma'}$, where Γ' is some constant different from $\Gamma = \dfrac{c_p}{c_v}$, which relation corresponds to a effective heating for values of $\Gamma' < \Gamma$. As discussed in Mestel (2012), it is known since Parker (1963) that a constant Γ' results in inconsistencies of the solution near and far from the stellar surface. In the case of the Sun, adjusting Γ' in order to fit the observations at 1AU results in unphysically high velocities and low densities at the solar surface. Analogically, in the case of jets, the terminal velocities of the outflow are way smaller than the observed velocities of the jets.

We are not going to try to disentangle contributions to this heating function from physically plausible arguments, and we will instead say that the heating distribution used in these models is the one needed to maintain this geometry and this geometry is close to the observed geometry of the flow. The goal of this study will not be to understand the nature of this heating, but to understand relevant physics in the context of this geometry. A correct treatment should compute contributions from processes like thermal conduction in the atmosphere (starting from the important input of heat at the base), heating from damping of waves from the sub-photospheric convection, (Decampli, 1981), and to compute the radiative transfer of energy in the wind by the radiation from the central source. Moreover, Matt & Pudritz (2005) argue that heat could be deposited by accretion.

In numerical simulations, we are going to set up inital and boundary conditions for all MHD quantities coming from the semi-analytical solution and in addition to that we will *a priori* impose the heating function and

release the constraints on the MHD quantities. We will prove that this configuration is stable.

3.6 Study of the solution close to the inner boundary (central object)

The magnetic topology of the Cylindrical Analytical Stellar Outflow (CASO) contains three distinct regions. First, a polar region with open fieldlines, rooted at the star, second, a disk region with open fieldlines, rooted in the disk, and third, a region with closed fieldlines, with both footprints are rooted in the star. Matter is ejected from the disk in the "disk wind"-like region and from the star, both in the stellar wind region and the closed-line region. These three zones meet and the "X-point," where the last closed fieldline crosses the equator. This line is connected, at the X-point, with the "last connected line", which is the common interface of the three regions: the two open lines regions (the one with the topology of a stellar wind and the other with a topology of a disk wind) and the other with closed field lines (see Figure 3.3).

This CASO solution has the disadvantage (as we will explain in §4.1.2) of having non-zero velocities in the closed fieldlines region (which we call 'dead zone' or 'magnetosphere' in green on Figure 3.3), and we will modify this in Chapter 4.

3.7 Initialization of the simulation

As our ultimate goal is to understand the physical characteristics of outflows with such topologies, the question of what is the topological stability of these solutions is of crucial importance. In a fashion similar to Matsakos *et al.* (2008) and Matsakos *et al.* (2009), we test the stability of this analytical

solution by setting it up as an initial condition in a time-dependent MHD simulation.

To solve the equations of ideal MHD, we make use of the PLUTO code (Mignone *et al.*, 2007). We perform a 2.5 dimensionnal simulation, which means that the toroidal vector components of **V** and **B** remain axisymmetric; second order time integration is achieved by a Runge-Kutta method and we also use a linear interpolation in space. The computationally efficient Lax-Friedrich solver is used, but switching to less diffusive Riemann solvers does not introduce any significant change to the solution. The $\nabla \cdot B = 0$ requirement is enforced with an eight-wave MHD algorithm.

Naturally, we use spherical coordinates, which allows us to take advantage of the natural grid cell accumulation near the surface of the central object (i.e. the inner boundary of our simulation box), which allows for our simulation to achieve better resolution near this inner boundary, where the jet launching region, which is of particular interest, is situated.

In this scenario, when we initialize the simulation box with the semi-analytical solution, what we expect for this initial condition is to be an "educated guess" of the final state. We anticipate such a behaviour because these solutions were semi-analytically obtained with reasonable approximations, and we expect them to relax to a final steady state, which will not differ significantly from the initial one. Our goal is to verify this. We indeed obtain a final state very close to the initial one, and we pursue the simulation until relaxing to a steady state. In order to detect changes, we will be investigating the relative differences for all MHD quantities between the final and the initial state, which will enlighten us how the final steady state differs from the initial educated guess. This is done for this model in Appendix A, and in subsequent appendices for the other models.

Differences between the initial setup and final state are hardly visible to the naked eye, so in Appendix A, we plotted the relative differences between the initial and the final states for all eight MHD quantities.
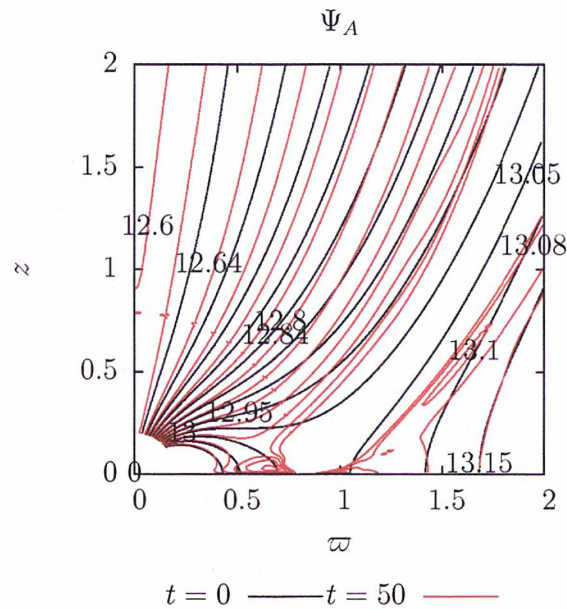
FIGURE 3.5: Contour plot of Ψ_A, for $t = 0.0$ and $t = 50.0t_*$

First we are going to discuss the conservation (and non-conservation) of α along fieldlines. At the initial step, the α contours are parallel to fieldlines, as we discussed above this is because of stationarity and axisymmetry. Nevertheless, we notice that the last connected line, which has $\alpha = 0.9885$ tends asymptotically towards the $\alpha = 1.0$ (α, the dimensionless magnetic flux is normalized to its value at the fieldline passing through $r = r_*$). On the bottom panel of Fig. 3.6 we plot several fieldlines rooted between the X-point, where the last connected line crosses the equator, and $R/R_* = 1$. What we see is that matter coming the star, travelling along the last connected line, mixes with matter coming from the equator between the X-point and Alfvén radius, and flows in the interface between the stellar wind and the disk wind, which becomes more and more narrow as we go further from the star. This immediately makes this 'interface region' of particular interest, and we are curious to investigate its stability.
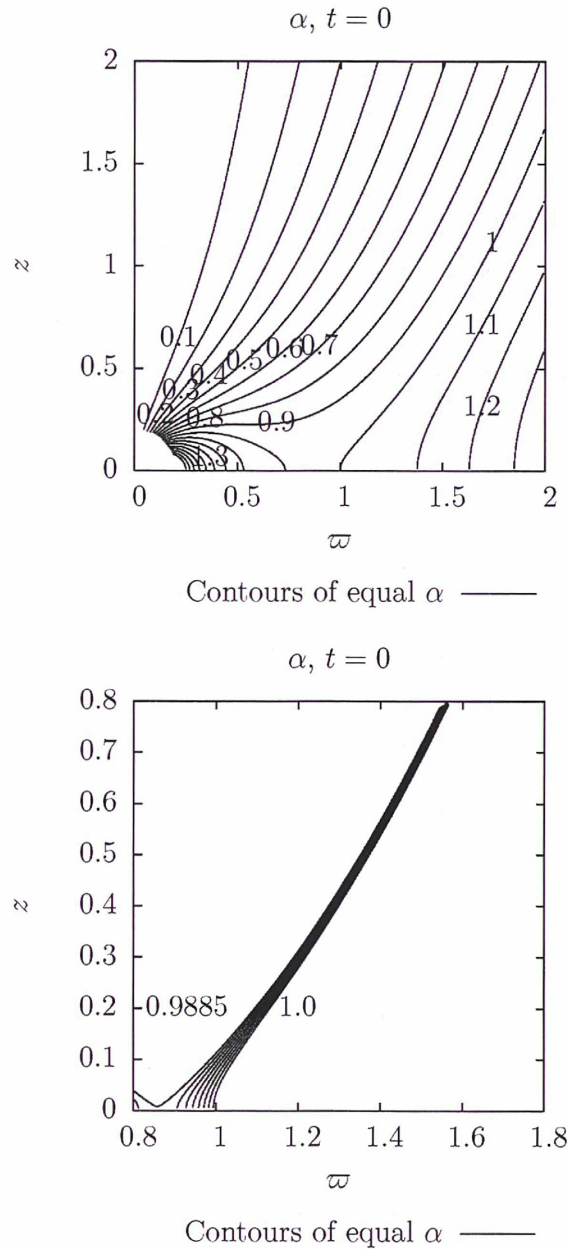
FIGURE 3.6: On the top panel: Contour plot of α, each value labelizing a fieldline; on the bottom panel: Zoom of the top panel plot, but only contours between $\alpha = 0.9885$ (the last connected line) and $\alpha = 1.0$ (passing through the reference radius and towards which the last connected line asymptotically tends) are shown.

3.8 Outcome of the simulation

As the initial setup evolves for a sufficently long time (until $t = 50t_* = 8.45t_{\text{Kep}}$), we notice that the flow globally goes to a steady state, but not everywhere. In order to understand the stability of the solution, we plot, in Appendix A the relative differences between the final and initial state of all MHD quantities. We will also discuss the quantities, supposed to be conserved, as well as the quantities τ, the torque, and the plasma β parameter, which will help us understand the impact of releasing the stationarity constraint in the problem. Equations 2.16, 2.17, 2.18, respectively for Ψ_A, Ω and L, are conserved quantities in the case of stationary, axisymmetric flows. Although we are not under the hypotheses of a stationary flow, since the problem is now time-dependant, we find instructive to plot those quantities and to try to quantify the departure from stationarity in the different parts of the outflow. We remind that in the case of the semi-analytical solution, the lines of equal Ψ_A, Ω and L are parallel to the fieldlines, and because of the existence of those conserved quantities the *stationary* semi-analytical solutions were derived.

3.8.1 Mass-to-magnetic flux ratio Ψ_A

First, we conclude that the stellar wind part of the outflow, for which description the model is specifically constructed, is going to a steady state. The Ψ_A contours in this region of the flow are practically parallel to those of the initial setup; such is also the case of the disk wind.

Different is the case of the interface region, which fieldlines we plotted in Fig. 3.6. As it is shown on Fig. 3.6, fieldlines rooted between $\varpi = r = 0.841r_*$ and $\varpi = r = r_*$ on the equator pratically merge as we go further from the central driving source. So, matter, ejected from this region on the equator, goes in a very small flux tube. We argue that this does not affect the stability of the solution for this reason. Also, we should note that the

value of Ψ_A is very sensitive to changes in the value of the magnetic field, since the magnetic field is in the denominator of Ψ_A and is much smaller than the numerator. Therefore, other conserved quantities as L, showing less sensitive behaviour in this zone, might be more relevant to describe it.

The X-point itself is forced to keep its position, since those lines cannot reconnect because of the fact that we are under the hypotheses of ideal MHD (up to numerical diffusivity). Even if we are in ideal MHD, we cannot escape from numerical magnetic diffusivity. Including physical magnetic diffusivity is out of the scope of this work, but as Fendt (2009) suggests, magnetic diffusivity might be included in the study of ideal MHD systems. Such a diffusivity should be enough in order to allow reconnection, and to gain better insight into the effects of the X-point within the framework of these models. But this diffusivity should be kept small, in order to keep the quasi-ideal MHD treatment of the problem, *i.e.* not to modify the dynamics of the system, and most importantly, collimation of the outflow.

3.8.2 Specific angular momentum L and torque

We note that the angular momentum L is very close to the initial angular momentum distribution (Fig. 3.10). This quantity is of important in our problem since it has direct consequence on observable quantities, as discussed in §1.2.8. The fact that the contours of L are parallel to the fieldlines, except in a small zone near the X-point, confirms our conclusion, coming first from the fact that the MHD quantities are not showing important differences, hence the solution is topologically stable on these scales, and second, the fact that Ψ_A and Ω show sensitive behaviours in the interface region shows that it might be a region of transient phenomena. A similar interface region is observed in the recent simulations of Zanni & Ferreira (2013).

Related to the angular momentum is the torque τ, which expression is given in Eq. 2.20 and which we plot in Fig. 3.11. This quantity is of central

importance for this study, since the main physical effect of winds is to ensure angular momentum extraction and the torque quantifies this process and the aforementionned graph gives some interesting point of view on the numerical solution. When we plot the torque for the semi-analytical initial condition, we see that in this model, the torques of the disk wind, the stellar wind and the magnetosphere are comparable. The difference between the axial fieldline, carrying the smallest torque, and the typical torque values of the disk wind is less than one order of magnitude. Nevertheless, what is interesting to note, is that the closed fieldlines in the magnetosphere have the biggest torque. This torque does not extract angular momentum from the star, since the matter moving along those fieldlines stays in the magnetosphere and is not taken away. Nevertheless, here is probably the biggest difference between the semi-analytical solution and the numerical solution that we obtain in the final state. In the final state of the torque (red lines on Fig. 3.11), we see that the fieldlines with the biggest torque are now on the other side of the X-point, in the interface region discussed on Fig. 3.6, instead of being trapped in the closed magnetosphere. As we discussed for Fig. 3.6, all the outflow from $\varpi = r = 0.85r_*$ (the X-point) and $\varpi = r = r_*$ tends towards the flow on the last connected line, on the interface between the disk wind and the stellar wind. We tentatively conclude that because of this result of the simulation, this region might be important for angular momentum extraction.

3.8.3 Ω, plasma β and T

The other integral, Ω, plotted on Fig. 3.9. We have also plotted the contours of the plasma β parameter, on Fig. 3.8. Again, this is another parameter hinting for the stablity of the solution. In the disk wind and stellar wind zones of the solution, the value of the β field is close to its initial one. In the interface region, the plasma β is diverging from its initial value, showing again that the semi-analytical solution is topologically stable almost everywhere, except in this region. Also, we plotted $\ln \beta$, on Fig. 3.8, where it

could be seen that in the very close vicinity of the star, the magnetic pressure is much bigger than the kinetic pressure, what is needed for magnetic braking to operate. The variations of orders of magnitude show how fast actually the ratio thermal/magnetic pressure is dropping. In the regions with low beta, the magnetic pressure is dominant and the plasma, ejected from the star is in forced corotation with the star. The particles are hence having a larger angular momentum than what should have an uncharged particle in the gravitational field of the star. Once the particle passes in the region with high β/low magnetic pressure, the inertia of the plasma particle is much bigger and it carries with it the magnetic field, and also takes away the angular momentum it extracted from the star before reaching the isorotation radius. This phenomenon of 'magnetic braking' was described for a first time in the seminal of paper Schatzman (1962).

We are also plotted the temperature $T = \dfrac{P}{\rho}$ in the whole domain (Fig. 3.7). In the framework of this model, in Eq. 2.30, we note that we have the arbitrary constant P_0 allowing us to callibrate the temperature in such a way that it matches the observations. This comes from the fact that what participates in the force balance is the pressure gradient. We can hence add any scalar constant to the whole pressure field. We use $P_0 = 50P_*$, which ensures 0 pressure gradient at the outer part of the domain ($R = 340$) and normalizes the β to 1 at $R = 1$ on the axis. What results is that the ratio of the temperature at the edge of the jet and temperature at the center is approximately 5 times.
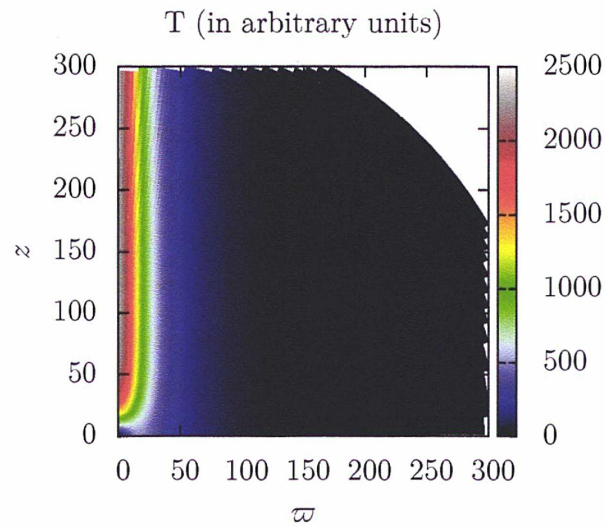
FIGURE 3.7: The temperature accross the whole domain. Note that the temperature is in arbitrary units since P_0 is an arbitrary integration constant in Eq. 2.30.

FIGURE 3.8: The plasma beta is dropping fast as one gets close to the star.

FIGURE 3.9: Ω for the semi-analytical solution and its evolution to its final state

FIGURE 3.10: The angular momentum L is well conserved during the simulation

FIGURE 3.11: The torque τ throughout the simulation

Chapter 4

Cold dead zone

Contents

Chapter Abstract

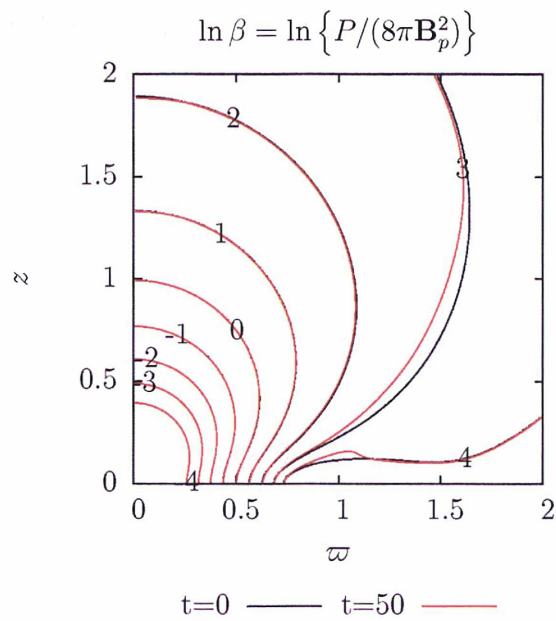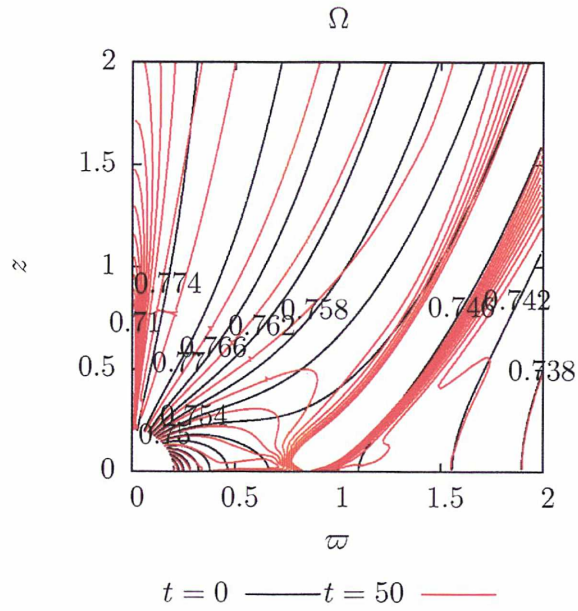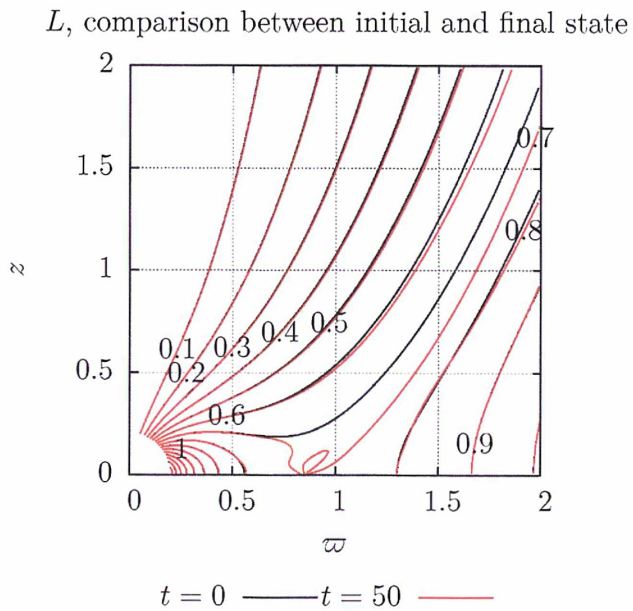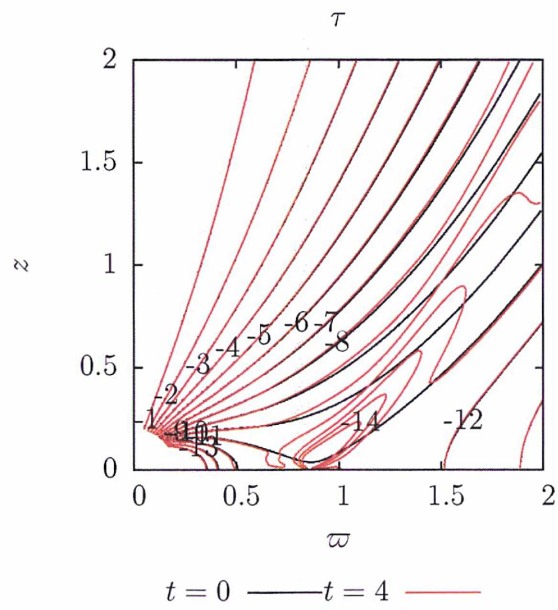The goal of this chapter is to describe the approach we used in order to obtain a solution of a stellar outflow with a static magnetosphere – a 'dead zone'. First, we discuss why the matter in the magnetosphere should be in static equilibrium and how this is treated in an inconsistent way in the CASO solution, presented in the previous chapter. We also discuss observations of clouds, around some stars, confined in stellar-sized closed loops. Then we describe the procedure, we followed in order to obtain such solutions, namely modifying the CASO solution, by introducing a static magnetosphere, and discussing the implications of this on other MHD quantities. Finally, we discuss the outcome of the simulation, by describing the stated the simulation box converged to, and discussing the physical implications of this result, notably how the structure of the dead zone corresponds better to the observations than the original, non-static magnetosphere of the CASO solution.

4.1 Introducing a self-consistent dead zone

4.1.1 Need for a more precise study of the close vicinity of the star

As discussed in the previous chapter, semi-analytical solutions obtained by Sauty & Tsinganos (1994) have been found to be topologically stable at propagation scales by Matsakos *et al.* (2008). In the previous chapter we discussed the topological stability of a particular analytical solution, obtained in Sauty *et al.* (2011). The main difference is that here we are studying the close vicinity of the star, where the accretion-ejection connection takes place. Unlike the studies of the propagation scales, we resolve

the magnetosphere: a zone where both footprints of the magnetic field lines are rooted to the star.

4.1.2 Inconsistency of the analytical solution: why the magnetosphere should be in static equilibrium

An inconsistency of the analytical solution, relevant to the current work, is the way the magnetosphere is treated. The magnetosphere is the region of the outflow, where both ends of the magnetic fieldlines are rooted in the star, i.e. the fieldlines are closed. Hence, matter flowing along the closed magnetic fieldlines, emanating from the star in a given point in the magnetosphere, will at some point reach the equator. There it will meet a plasma flow coming from the southern hemisphere. Plasma coming from above and from below the equator will have momentum fluxes both perpendicular to the equator, but in opposite directions. We remind that we are in regime of low plasma β ($\beta = \left\{ P/(8\pi \mathbf{B}_p^2) \right\}$). Hence the magnetic energy density will still be much larger than the thermal, so plasma flows with opposite momentum fluxes, constrained to follow the magnetic field lines, will be stopped in this collision, *i.e.* the big magnetic pressure is holding the gas in hydrostatic equilibrium. (Decampli, 1981)

In a very general context, the condition $\beta \ll 1$ ensures that a static plasma remains stable (in the case $\beta \gg 1$ a static plasma would collapse.) Moreover, once in magneto-hydrostatic equilibrium, the flow will remain in this state, such any perturbation of the magnetic fieldlines will generate a perturbation of the magnetic pressure that will compensate any perturbation in the thermal pressure, as explained in Mestel (1968). Flows with static magnetospheres have been investigated by Tsinganos & Low (1989), and for the first time numerically, in the approximation of an isothermal flow, by Pneuman & Kopp (1971). The seminal paper of Keppens & Goedbloed (1999) investigated models with static zones in polytropic outflows.

In this and the next chapter, we will be investigating flows with static magnetospheres (dead zones), by modifying the solution presented in the previous chapter. Hence, we will introduce a static magnetosphere in this solution, which has non-polytropic heating function (starting from the one in § 3.5, but accordingly modified, see next paragraph). In the modified solution, the equator in the magnetosphere will no longer be a sink for matter, which is rather unphysical.

A point not explored in this work, but for which a perspective is opened by introducing a self-consistent magnetosphere, is to include accretion in the simulation box, in particular by adding accretion columns in this region.

4.1.3   Dead zones in observations

4.1.3.1   The case of AB Dor

Indications for the presence of dead zones around stars come from X-ray, UV and radio observations. First indications that some stars have prominences (hosted by closed magnetic loops) come in the early 1980s with UV observations of Schroeder (1983). Later, observations of Algol by White et al. (1986) also suggest the presence of large, hot, closed loop structures around the variable star. We will focus on a well-studied case, the variable star AB Dor (=HD 36705). Collier Cameron (1988) explain the anomalously low rising times of X-ray flares of AB Dor with gas, trapped in large, hot, closed loop structures in the stellar corona, hosting quiescent prominences. Collier Cameron & Robinson (1989a,b) make an extensive study of AB Dor, observing the variable star in H_α. Their observations show prominence-like clouds of mainly neutral hydrogen, spreading between 3 and 9 stellar radii, orbiting in forced corotation with the star. They conclude that most probably closed magnetic loops are the confining agent for these clouds. These slingshots of plasma in suspension over

the stellar surface are, the observations again show, of stellar size. Collier Cameron & Robinson (1989a,b) attribute the absoption spectra of quiescent stellar-sized prominences. For a review of the observations of stars hosting stellar sized prominences the reader is referred to the article Collier Cameron (1996). Ferreira & Mendoza-Briceño (1997) point out that such stellar-sized loops do not have solar counterparts. In the case of the Sun, closed loops have much smaller sizes. This lack of counterpart is a reason, they argue, that more convincing evidence for the existence of such loops should be provided. According to Mestel (2012), and references therein Stix (2004) and Dwivedi (2003), high emission regions in X-ray of the Sun and late-type young stars are associated with wind zones, whether coronal hole regions are associated with wind zones.

4.1.3.2 The case of BP Tau

BP Tau is a classical T Tauri star (cTTS). Spectropolarimetric observations with the ESPaDOnS instrument at the CFHT and NARVAL instrument at TBL, carried out by Donati *et al.* (2008), reveal the existence of a 1.2kG dipole and 1.6kG octupole. The dipole field is a slithly tilted, strong axisymmetric poloidal field. They also conclude that the magnetosphere of BP Tau extends to 4 stellar radii.

Sauty *et al.* (2011) discuss some similarities between the CASO solution and the structure of the magnetic field around BP Tau. The CASO solution has $B_* = 1.82$kG, which roughly corresponds to the value of strength of the dipole of BP Tau. The Alfvén point is situated at $\varpi = R = 9.29r_0$, and the terminal speed is $V_* = 103$kms^{-1} (for the notations refer to Table 2.1). In the case of the CASO solution, the magnetosphere terminates at the equator at a distance $\varpi = r = 7.97r_0$, while Donati *et al.* (2008) point out that the magnetosphere of BP Tau extends to $4r_0$. This point will be relevant in a subsequent discussion.

4.1.4 Constructing a self-consistent solution with no mass flux through the equator

We will attempt to obtain a numerical solution, by modifying the existent solution by suppressing accordingly the mass flux through the equator by replacing the poloidal velocity field with a null field.

There is no reason for this modified field to be solution of the ideal MHD equations. Nevertheless, we suppose that this configuration will be close to a solution, and we will initialize a simulation box with a null poloidal velocity field and velocity field identical to the CASO solution outside the dead zone. Our exceptation is that the simulation box will relax to a steady state with a two-component corona (corona with 'wind' zone outside the magnetosphere and a 'dead' zone in the magnetosphere.) An analogical procedure is followed in Keppens & Goedbloed (1999), who obtain 2.5D solutions for polytropical models of stellar wind with a dead zone. The difference with our problem is that we have a non-polytropic heating function and the different geometry of the flow. Imposing $\mathbf{V_p} = \mathbf{0}$ has several consequences for other MHD quantities and we are going to discuss this in the next subsection.

4.1.5 Introducing self-consistent boundaries

Setting $V_r = 0$ and $V_\theta = 0$, and as we still except stationary ($\frac{\partial}{\partial t}\cdot = 0$) and axisymmetric ($\frac{\partial}{\partial \phi}\cdot = 0$), for the projection along ϕ of Eq. 2.9, we have:

$$\left(\frac{\partial \mathbf{V}}{\partial t} + (\nabla \cdot \mathbf{V})\mathbf{V} + \frac{1}{\rho}\mathbf{B} \times (\nabla \times \mathbf{B}) + \frac{1}{\rho}\nabla P + \nabla \Phi \right) \cdot \hat{\phi} = 0 \qquad (4.1)$$

where $\hat{\phi}$ is the unit vector in the azimuthal direction. The Lorentz force $\mathbf{B} \times (\nabla \times \mathbf{B})$ will be noted $\mathbf{F_L}$. Since the gravity has no component along ϕ and $\frac{\partial}{\partial \phi}\cdot = 0$, the first, forth and fifth term in the bracket are evidently equal to zero. We are left with

$$\left((\nabla \cdot \mathbf{V})\mathbf{V} + \frac{1}{\rho}\mathbf{F_L} \right) \cdot \hat{\boldsymbol{\phi}} = 0 \tag{4.2}$$

Now, let us look at the $((\nabla \cdot \mathbf{V})\mathbf{V}) \cdot \hat{\boldsymbol{\phi}}$ term:

$$((\nabla \cdot \mathbf{V})\mathbf{V}) \cdot \hat{\boldsymbol{\phi}} = \left\{ V_r \frac{\partial V_\phi}{\partial r} + \frac{V_\theta}{r}\frac{\partial V_\phi}{\partial \theta} \right.$$
$$\left. + \frac{V_\phi}{r\sin(\theta)}\frac{\partial V_\phi}{\partial \phi} + \frac{V_\phi V_r}{r} + \frac{V_\phi V_\theta \cot(\theta)}{r} \right\} \tag{4.3}$$

The first, second, forth and fifth term of the equation should be equal to zero because of the static condition of the dead zone. The third term should be equal to zero because of axisymmetry. Hence, we are left with the condition that for a static magnetosphere, we need a zero component of the Lorentz force along ϕ. Otherwise, as could be shown by reversing Eq. 4.2 for $(F_L)_\phi \neq 0$, and taking into account the exact expression in Eq. 4.3, this component will accelerate matter in the dead zone. Hence, we need $L_\phi = 0$. The equation

$$\left(\frac{1}{\rho}\mathbf{B} \times (\nabla \times \mathbf{B}) \right) \cdot \hat{\boldsymbol{\phi}} = 0 \tag{4.4}$$

developped in spherical coordinates is

$$B_\phi \left(-\frac{B_R}{R} - B_R \frac{B_{\phi,R}}{B_\phi} + \frac{2}{R\tan\theta}B_\theta \right) = 0 \tag{4.5}$$

Hence, if we want to keep the $\mathbf{V_p} = \mathbf{0}$ in the dead zone, preventing the Lorentz force to accelerate the matter in the poloidal place, we should impose for the toroidal magnetic field component $B_\phi = 0$, as an initial and boundary condition in the dead zone. Moreover, in order to prevent a toroidal magnetic field to form, we should also impose the physically

plausible condition to have a magnetosphere in solid rotation with its host star, which will be consistent with the observations of quiescent prominences in stellar coronae, as discussed in §4.1.3. Setting $\mathbf{V_p} = \mathbf{0}$ has also consequences on the heating equation (Eq. 2.10), which LHS terms vanish because of the stationarity, axisymmetry, and static magnetosphere conditions, and the equation reduces to $H - \Lambda = 0$, in which $H - \Lambda$ is the source term in the heating equation (Eq. 2.10). Thus, to reach a steady state, the heating must be exactly balanced by a heat loss process ($H = \Lambda$). Physically, when the plasma is static in the dead zone, we are not able to transport heat either. In other words, in the heating balance participate the mechanical energy flux, the conductive flux and the radiative losses. In order to keep $H - \Lambda = 0$ we suppose that all mechanical energy input should be radiated away. Conductive cooling is rejected for a mechanism, assuring the heat/loss balance, since the quasi-isothermal structure of the stellar coronae, it its vanishing thermal gradient, prohibits heat conduction.

Until now, we discussed the implications of setting a static zone in rotation with its host star, starting from the $\mathbf{V}_p = 0$ condition and the resulting $B_\phi = 0$, $H - \Lambda = 0$ and V_ϕ in solid rotation. This is what makes the dead zone self-consistent. We set up other MHD quantities, such as density and pressure, to their theoretical values as if there was no dead zone, excepting this to be an educated guess for their final steady state, which will be obtained once they relax in a stationary state. On Fig. 4.1 we plot several quantities at $t = 0$.

4.2   Initial and boundary conditions, heating

Regarding the simulation box, we are going to use the same mesh as the one described in §3.2, which we used for the CASO solution. Regarding the boundaries, we will suppress mass flux in the dead zone, and we will modify magnetic field, rotation and heating according to the discussion in the previous section. This means that the heating will be suppressed in
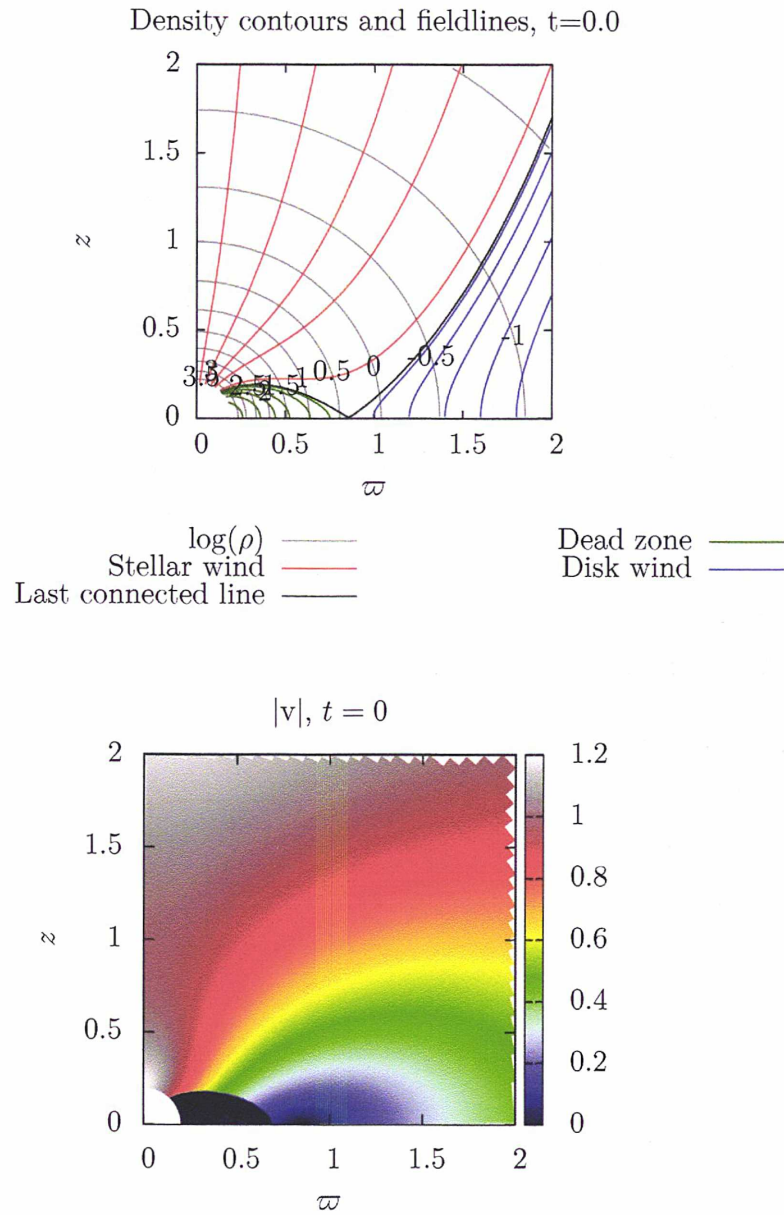
Density contours and fieldlines, t=0.0

log(ρ) ——— Dead zone ———
Stellar wind ——— Disk wind ———
Last connected line ———

|v|, $t = 0$

FIGURE 4.1: Initial setup for the 'wind' and 'dead' zone configuration. The top panel shows the geometry of the magnetic field (magnetic field lines in the stellar wind are in red, disk wind fieldlines are in blue and magnetosphere fieldlines are in grey) and density contours (in grey). The bottom panel shows the magnitude of the poloidal velocity, identical to the analytical solution in the wind zone and set up to zero in the dead zone.
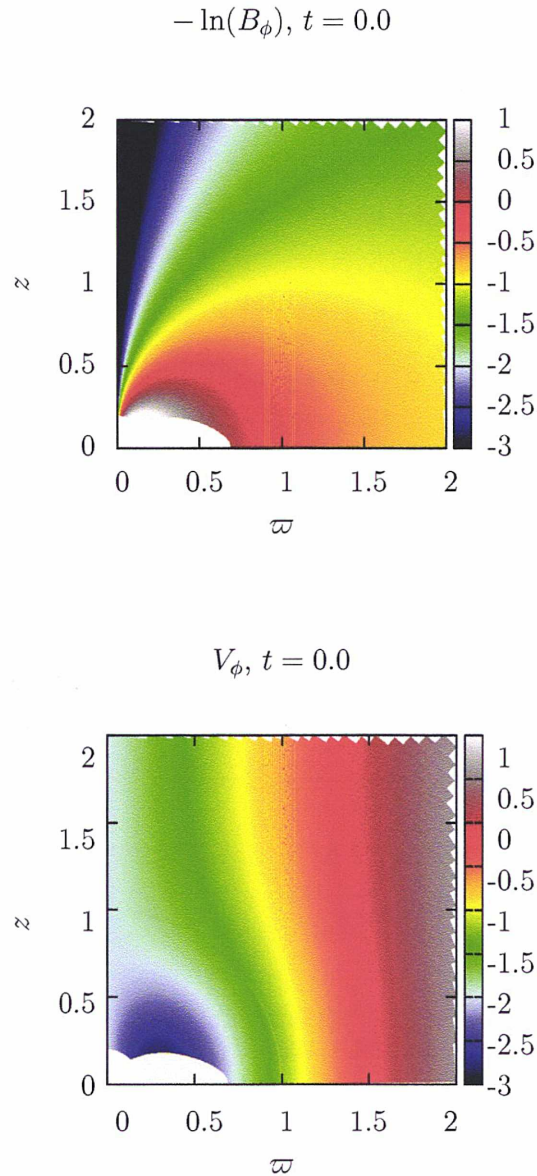
FIGURE 4.2: Toroidal components of the initial condition. The top panel shows the toroidal magnetic field component, set up to the analytical one in the wind zone and to 0 in the dead zone. On the bottom panel, we see the rotationnal velocity, on which we see a dead zone set up in solid rotation
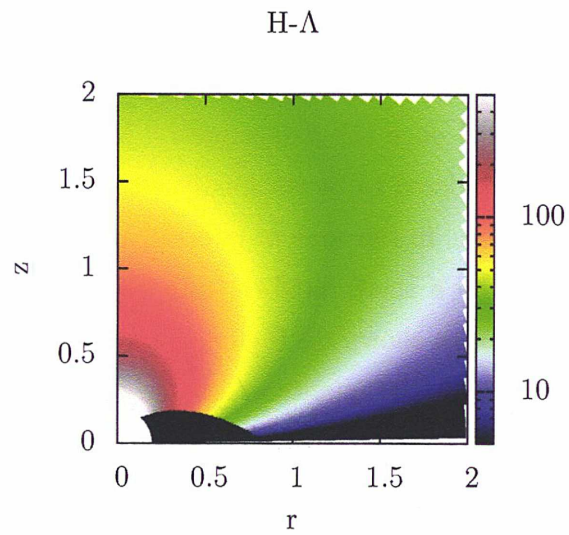
FIGURE 4.3: Heating function for an outflow with a static magnetosphere

the dead zone (see Fig. 4.3), so will be the toroidal magnetic field, and the rotation velocity will correspond to a solid rotation. For a graphic representation of the initial condition, refer to Figures 4.1 and 4.2.

The heating source term (Fig. 4.3) and the boundary conditions are kept constant throughout time.

4.3 Outcome of the simulation: description of the final solution

The simulation is ended once the axisymmetric MHD wind is converged to a state which is considered to be stationary when relative differences in all eight MHD quantities, in the zone of interest, between two consecutive timesteps are topped by a small number (typically 10^{-4}). The final distribution of the quantities shown on Figure 4.1 are shown on Figures 4.4 and 4.5. For the other 7 MHD quantities, the relative differences between the initial and the final state are given in Appendix B (LHS for the first part of the simulation, $0.0 < t < 4.0$, and RHS for the second part of the simulation, $4.0 < t < 20.0$). We see that the initial configuration for these quantities is maintained not in the whole dead zone, but only in a helmet-shaped part of it. The fieldlines of the initial dead zone from the side of the axis open up and matter is accelerated along them. As a consequence, the vicinity of the last connected line is emptied.

Globally, the disk wind remains at its place, so does the stellar wind. Several fieldlines on the interface between the disk wind and the dead zone open up; as we continue to treat the part of the boundary where they are rooted as a dead zone (zero mass flux), the density along the fieldlines previously in the dead zone drops. The final state could be divided in four regions, according to whether or not the initial condition is maintained and how. The first region is the wind zone. We conclude that, globally, the stellar wind, as well as the disk wind, keep their initial topology and are not affected, in any significant way, by the introduction of a dead zone. Second, the initial condition is not maintained all over the dead zone, but only in a helmet-shaped part of it. In the third part of the field, outside the helmet but within the initial dead zone, the initially closed fieldlines open up and matter is accelerated along them. The extension of those fieldlines outside the dead zone is asymptotically tending towards the last connected line, thus on the interface between the stellar wind and the disk wind. As

Density contours and fieldlines, t=4.0
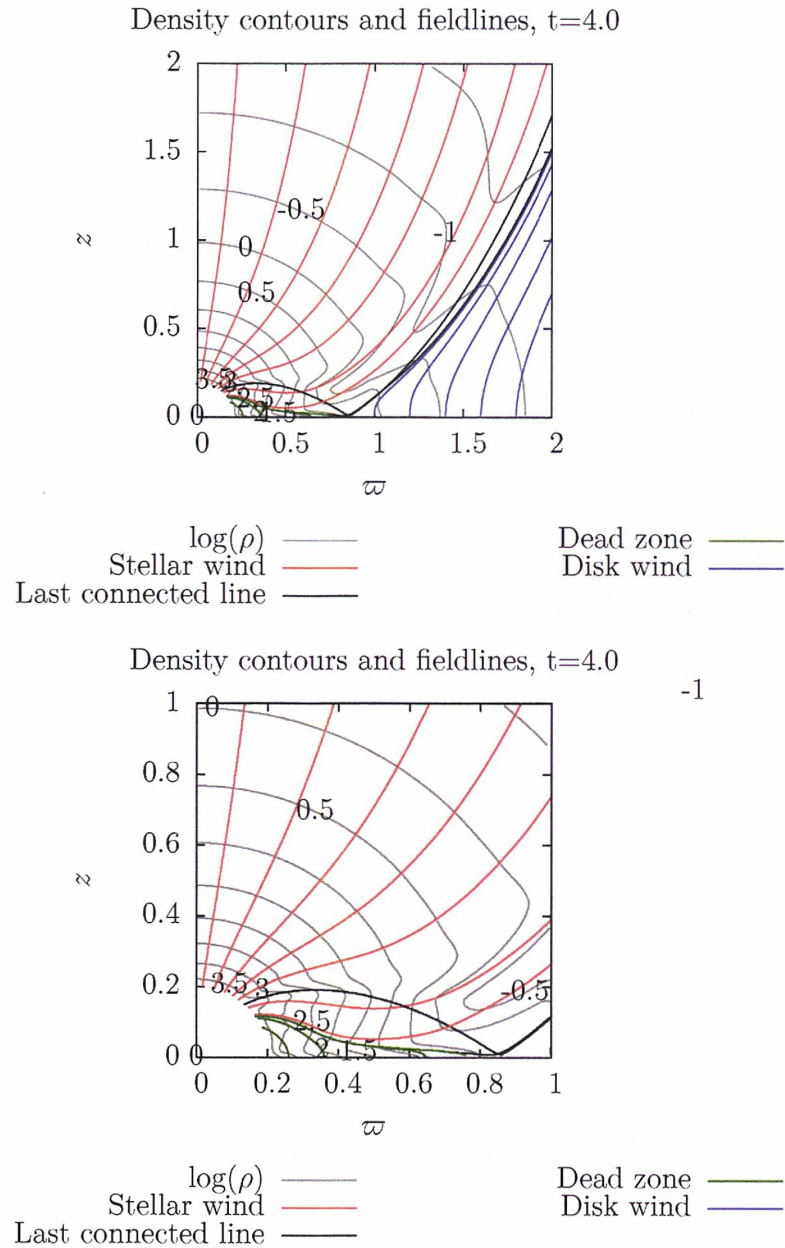

Density contours and fieldlines, t=4.0

FIGURE 4.4: Wind and dead zone configuration throughout a poloidal cross-section; fieldlines and density contours. The bottom figure is a zoom of the top figure. We see the green fieldlines, describing the new shape of the dead zone, have a characteristic helmet shape. The initial position of the last connected line is plotted for clarity.
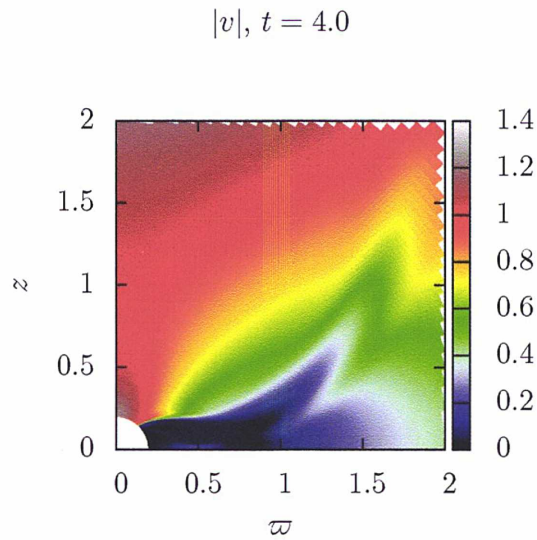
$|v|,\ t = 4.0$

FIGURE 4.5: The poloidal velocity remains $\mathbf{V_p} = 0$ in the dead zone as it is initialized; in a region along the opened fieldlines the poloidal velocity also drops

the boundary conditions are not evolving, but fixed in time, the fieldlines are rooted to a part of the inner boundary with zero mass flux (between the top of the helmet and the initial footprint of the last connected line). As a consequence the fourth region of the field is the one in the vicinity of the last connected line; the fieldlines opened up during the time evolution are emptying the vicinity of the last connected line.

As we can see from Figures 4.4 and 4.5, we have indeed a zone in which the fieldlines are connected to the star, and in which the initial conditions for B_ϕ and V_ϕ are maintained. Note the specific shape of the new last connected line on figure 4.4, reminding a helmet. In this helmet-shaped zone, the toroidal magnetic field component is kept to 0, and the solid rotation is maintained, as could be seen on 4.5.

Probably the most important feature of this simulation is the fact that the zone with closed fieldlines has smaller extent than in the initial setup. Indeed, if we look at the bottom panel of Fig. 4.4, we see that fieldlines,

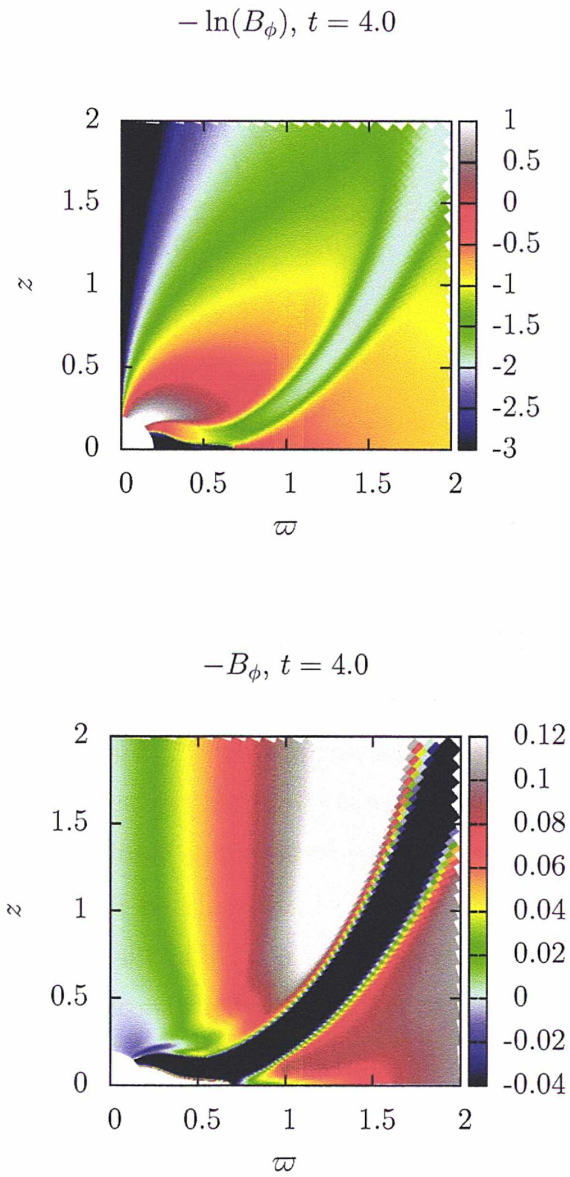$-\ln(B_\phi)$, $t = 4.0$

$-B_\phi$, $t = 4.0$

FIGURE 4.6: In the helmet-shaped region with closed fieldlines (green fieldlines on 4.4 the flow remains in solid rotation and satisfies $B_\phi = 0$; this makes the flow in this zone self-consistent, as explained in §4.1.5
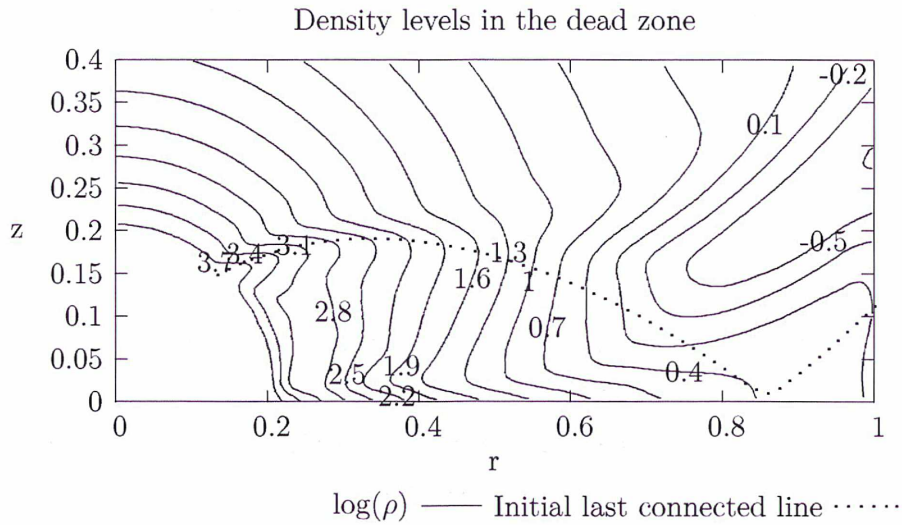
Density levels in the dead zone

$\log(\rho)$ —— Initial last connected line $\cdots\cdots$

FIGURE 4.7: Density contour plot in the dead zone. Matter is accumu-
lated near the equator.

rooted at the star, and initially situated within the dead zone (the initial
position of the dead zone is plotted on this figure for clarity), are no longer
closed. The initial position of the last connected line corresponds to $\alpha =$
0.9885, and in the final state, to $\alpha = 1.1411$, hence from a dead zone starting
at $\theta \approx 42°$, to a dead zone starting at $\theta \approx 47°$. Fieldlines, rooted between
$\theta = 42°$ and $\theta = 47°$, are emptied from matter, since we have suppressed
the outflow at the base, supposing that those fieldlines will remain closed.
On the other boundary, matter is accumulated near the equator, which
could be seen more easily on Figure 4.7. On the other side of the dead
zone, in the region close to the stellar wind, density is lower as compared
to the initial setup. The form of the closed fieldlines, in green of Fig. 4.4,

As we discussed in §4.1.2, in order to maintain plasma in static equilibrium,
we need the magnetic pressure to dominate the thermal pressure. This is
indeed verified on Fig. 4.10, where in black lines are the contours of the
plasma β parameter, which are also those of the CASO solution, and in red
are the contours of the plasma β at the final stage. We can see that this
parameter globally keeps its values throughout the domain, and drops in

the dead zone, which is convenient in the light of the requirement of low plasma β for dead zones.

We are also interested in seeing how the specific angular momentum (Fig. 4.9) and the total angular momentum (Fig. 4.8) are modified between the initial and the final state. First we note that along the fieldlines, rooted between $\theta = 42°$ and $\theta = 47°$ at the stellar surface, which open up, we have a much bigger specific angular momentum. As we maintained fixed the boundary conditions over there, and we suppressed the mass flux, those lines are emptied. This is why we plotted the total angular momentum flux, ρL. We see that this quantity is changing slightly, but not significantly between the initial and the final state of the simulation. We have also plotted the torque (Eq. 2.20), which represents the constant rate of angular momentum transport across a unit flux tube. For this simulation, it is plotted on Fig. 4.11.

In a similar way for the previous solution, we plotted the relative differences between the final and the initial state for this solution in Appendix B. As we can see from Fig. B.1, plotting the relative increase of density, we have a dead zone which is comparatively denser, and as we can see from Fig. B.3, a bigger pressure in the dead zone. In the self-consistent part of the dead zone with the helmet form, we have mutual increase of pressure and drop of density. This means that the resulting dead zone is with higher temperature than the surrounding flow. As we can see on Fig. 4.5, depicting the velocity field in the final state, the static condition is maintained in the dead zone. The requirements, derived in 4.1.5, for a self-consistent dead zone, are maintained in the helmet-shaped part of the dead zone, as could be deduced from the fact that in this helmet-shaped part of the dead zone, the relative changes in B_ϕ and V_ϕ (Figures B.9 and B.15) are null.

This helmet-shaped structure, which is similar to the structures observed in the solar corona in large closed loops, might be modified by the presence of an accretion disk, which we are not exploring in this work.

4.4 Physical implications

There are two important conclusions that could be drawn on the outcome of this simulation. First, the extent and the shape of the dead zone vary significantly for the given physical conditions. Let us remind that for the particular set of parameters in Table 3.1, gives a flow with magnetic field strength at the surface $B_0 \approx 1.1\text{kG}$, (Sauty *et al.*, 2011) compatible with the observed dipole of BP Tau $B_{\text{BPTau}} = 1.2\text{kG}$ of Donati *et al.* (2008). However, the CASO solution predicts a radius of the dead zone of ~ 7.5 stellar radii, while Donati *et al.* (2008) report a size of the dead zone of ~ 4 stellar radii. We conclude that within the framework of the discussed models, outflows with inconsistent magnetosphere (the CASO solution, having a mass flux through the equator), predict twice as large dead zone than the observed one. When we modify the solution, in order to introduce a static magnetosphere, the self-consistent dead zone is approximately half the size than the initial condition. Hence, the dead zone we obtained, delimited by the last connected line on Fig. 4.4 is corresponding better to the observations than the dead zone of the semi-analytical solution.

Next, as we said, the last connected fieldline is not rooted at $\theta = 42°$ at the inner boundary, but at $\theta = 47°$. Sauty *et al.* (2011) predict a braking time for such a system

$$T_{\text{brake}} \approx 2 \times 10^5 \, \text{yr}. \tag{4.6}$$

The braking time being computed by the following formula: (Sauty *et al.*, 2011)

$$T_{\text{brake}} = \frac{2k\mathcal{M}r_0^2}{r_*^2 \dot{M}_{\text{wind}}} \frac{\Psi_{\text{out}}}{\alpha_{\text{out}}\sqrt{1 + \delta\alpha_{\text{out}}}} \tag{4.7}$$

with k the dimensionless inertial constant of the star, and Ψ_{out}:

$$\Psi_{\text{out}} = \frac{2}{3\delta}\left\{(1+\delta\alpha_{\text{out}})^{\frac{3}{2}} - 1\right\} \tag{4.8}$$

Now, as we discussed, the last connected line is not the one with a magnetic flux of $\alpha_{\text{out},1} = 0.9885$, but $\alpha_{\text{out},2} = 1.1411$ ($\Psi_{\text{out},1} = 1.0073$ and $\Psi_{\text{out},2} = 1.1661$). Straightforwardly, the ratio of braking times $T_{\text{brake},1}/T_{\text{brake},2}$ of two winds, with two different values for α_{out}, but with the same physical characteristics of the central object, is:

$$\frac{T_{\text{brake},1}}{T_{\text{brake},2}} = \frac{\Psi_{\text{out},1}}{\alpha_{\text{out},1}\sqrt{1+\delta\alpha_{\text{out},1}}} \times \frac{\alpha_{\text{out},2}\sqrt{1+\delta\alpha_{\text{out},2}}}{\Psi_{\text{out},2}} \tag{4.9}$$

Hence

$$T_{\text{brake},2} = 0.9974 \times T_{\text{brake},1} \approx T_{\text{brake},1} \tag{4.10}$$

Hence, even if the big dead zone of the CASO solution and the smaller self-consistent one are rooted at different θ at the inner boundary, the braking time is not significantly smaller than in the previous model. That supports the conclusion that the smaller dead zone is not significantly changing the overall properties of the solution, but nevertheless its size is in better accordance with the observations.
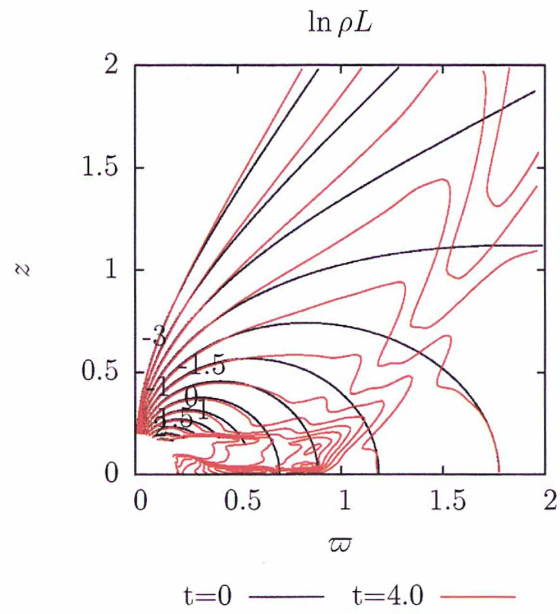
FIGURE 4.8: The total angular momentum L throughout the simulation
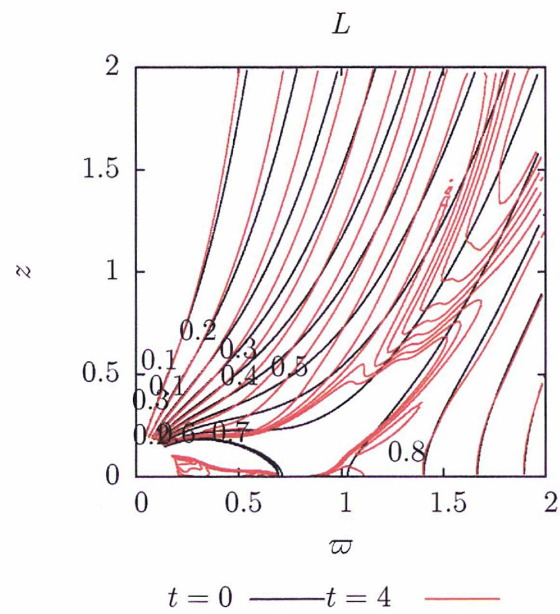
FIGURE 4.9: The specific angular momentum L throughout the simulation
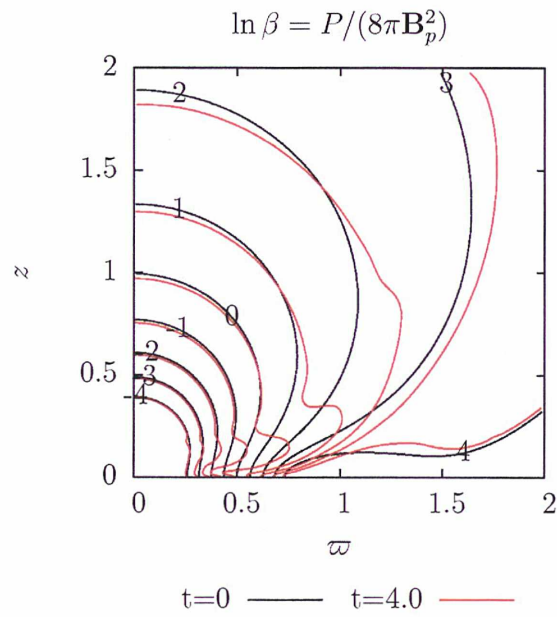
FIGURE 4.10: The plasma β throughout the simulation
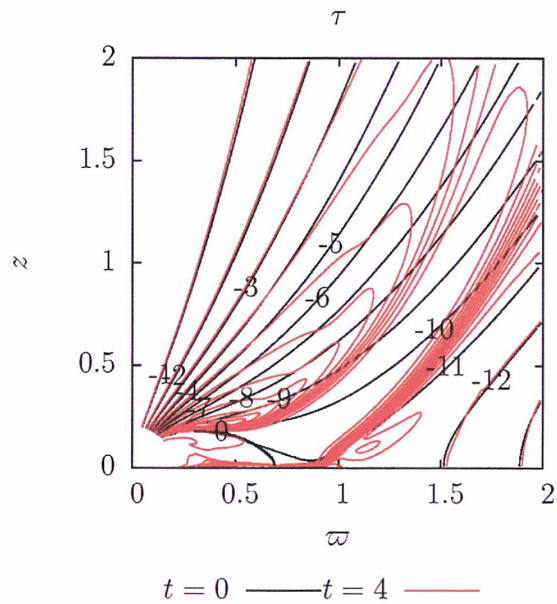
FIGURE 4.11: The torque τ throughout the simulation

4.5 Towards a fully self-consistent magnetosphere

4.5.1 Why the magnetosphere is reshaped during the simulation?

As we saw in the discussion so far, the magnetosphere is shrinking between the initial and the final stage of the simulation. This change in shape and extent could be easily understood as consequence of the the null poloidal speed that we impose at the beginning of the simulation. Indeed there is no reason to suppose that the magnetosphere should keep its initial shape. Its shape is governed by the force balance. Thus, by suppressing the polidal velocity in the magnetosphere, we are suppressing the inertial terms in the momentum equation (Eq. 2.9), and those terms are directed outwards. Hence, by suppressing them, the force balance changes, and inwards directed terms of the momentum equation, that were previously balanced by the then suppressed inertial terms, will tend to shrink the magnetosphere. The new balance is achieved when a pressure gradient, capable of stopping this shrinking, develops. Indeed, a close inspection of Fig. B.3 shows that in the reshaped magnetosphere, close to the inner boundary, the pressure has increased by $\approx 5\%$ and just outside the helmet-shaped magnetosphere the pressure has dropped by $\approx 10\%$. Hence, the pressure gradient in that region is steeper than the semi-analytical solution and is directed inwards. As the acceleration, resulting from the pressure gradient is always opposite to the pressure gradient $\left(\mathbf{a} = -\dfrac{\nabla P}{\rho} \right)$, this force is indeed replacing the suppressed intertial terms.

The way the pressure balance is modified is by changing the heating function, which is the source term of the energy equation (Eq. 2.11.) This solution, where the heating is turned off in the magnetosphere, could be compared to the solution in the next chapter, where the magnetosphere is

heated. In the case of the heated solution, an even bigger pressure gradient is indeed created and the magnetosphere shrinks less.

4.5.2   Modifications needed

There remains an inconsistency in the solution we presented so far. Indeed, some fieldlines open up, as previously discussed, but the boundary conditions we set are fixed in time. Mass flux is suppressed on all fieldlines that were closed at $t = 0.0$, no matter if they open up during the simulation or not. Allowing a mass flux on those lines means that we should also turn on the heating that we suppressed, because we wanted to suppress the velocities in this region. Hence we need to restore the heating, if we want to restore the mass flux along those fieldlines.

One possibility in order to decide whether or not to put a mass flux from the inner boundary and to turn on the heating is to determine if the fieldline is open or closed. But trace the fieldlines, at each timestep, is computationally prohibitive. The criterion we are going to use in order to decide if we are in the helmet-shaped self-consistent magnetosphere, in which we have to suppress mass flux and turn off heating, or outside it, is whether or not we are in the region that is in solid rotation and with no toroidal magnetic field component. As we discussed so far, inside the helmet-shaped magnetosphere those requirements are fulfilled and they are not fulfilled outside it.

Hence, we are going to turn off the heating only in the helmet-shaped part of the flow and we are going to suppress the mass flux only in that helmet-shaped part of the flow. In practice, the magnetosphere of the semi-analytical solution was starting at $\theta_{\text{lim}} = 41.7°$, and for $t = 4.0$ this angle increased to to $\theta_{\text{lim}} = 54.9°$, hence we are going to suppress the mass flux only for $\theta > 54.9°$. Also, we are going to turn off the heating for the fieldline, for which $|B_\phi| = 0.01 B_*$ and all the fieldlines below. At $t = 12.0$, we will have a new magnetosphere. What we observe is that this time, some

TABLE 4.1: Evolution of θ_{lim} during the consecutive readjustments

t	θ_{lim}
0.0	41.7°
4.0	54.9°
9.00	50.43°
14.00	50.10°
20.00	50.17°

fieldlines will close and the extent and size of the magnetosphere will slightly increase, but will not attain the initial value. Hence, at $t = 12.0$, we are going to readjust again heating, so that the whole magnetosphere is heated, and we will readjust the mass flux, which will be suppressed now from $\theta_{\text{lim}} = 50.417°$. We will re-run the simulation until $t = 15.0$ and we will find a new shape of the dead zone and a new $\theta_{\text{lim}} = 52.98°$, but the variation will be less important as compared to the previous step. With this approach, we are improving, or *training* the model at each step. The evolution of the last connected line, determining the size of the magnetosphere, is shown on Fig. 4.13 and the evolution of θ_{lim} is summarized in Table 4.1

By following this recipe, we are able to decrease the size of the zone which is not self-consistent, with each step, until we have a solution with an inconsistent part so small, that we could confidently say that the whole solution we have obtained is actually self-consistent. For illustration, on Fig. 4.14 is plotted the poloidal velocity magnitude, and as we can see $\mathbf{V_p} = 0$ only in the helmet-shaped region. On Fig. 4.15 is plotted the density, so we can compare the density of the final model and the density of the solution with a static, self-consistent helmet-shaped magnetosphere.
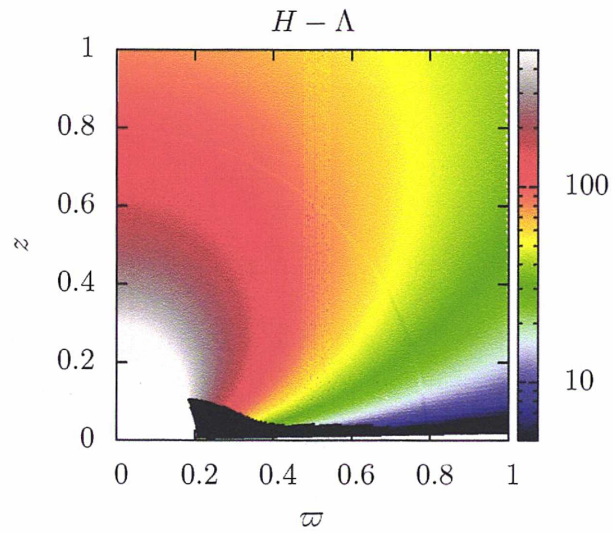
FIGURE 4.12: The heating function $H - \Lambda$ corresponding to the helmet-shaped magnetosphere
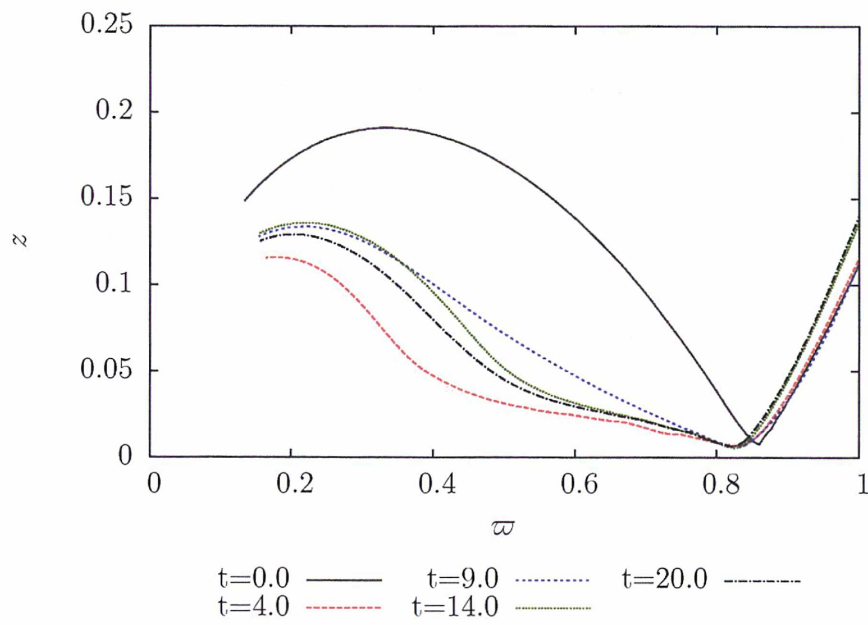

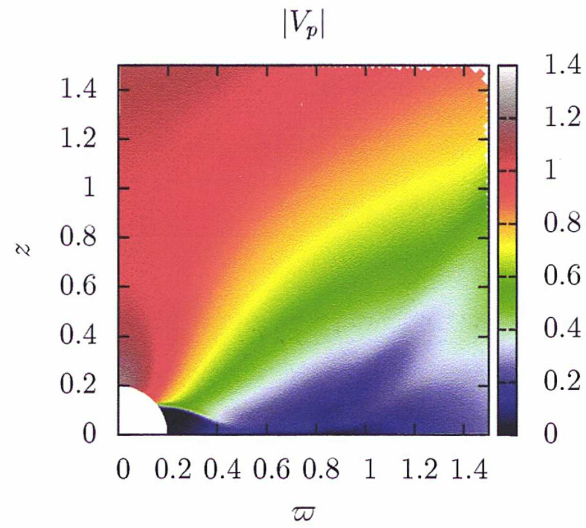FIGURE 4.13: Evolution of the size of the magnetosphere on each re-adjustment step

$|V_p|$

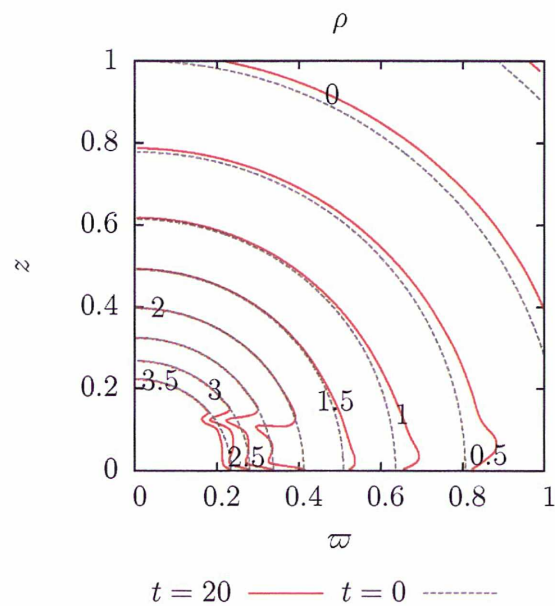FIGURE 4.14: Poloidal velocity magnitude during the simulation

ρ

$t = 20$ ——— $t = 0$ ----------

FIGURE 4.15: Density during the simulation

Chapter 5

Heated dead zone

Contents

Chapter Abstract

The goal of this short chapter is to investigate the hypothesis under which the heating flux in the dead zone is not null. By using the same heating function as the one used in Chapter 3, we find a solution with a dead zone, which is larger than the Cold dead zone solution of Chapter 4, but still with no mass flux through the equator. In all cases, the heating function, used to ensure the topological stablity of the solution is not imposed a priori, but emerges as a consequence of the construction of the model, under the hypothesis of self-similarity. Assuming a non-zero heat function is equivalent to considering that physical processes, responsible for heating/cooling in the wind are not exactly balanced. Including a full heating is a limit case, but nevertheless shows that a self-consistent dead zone could also be constructed in this case, enabling to study the influence of different heatings on such outflows.

5.1 Initial and boundary conditions for the simulation

The initial conditions for this simulation will be the same as those used in the Cold dead zone solution of Chapter 4. We are plotting this initial condition on Figures 5.1 and 5.2. The difference with the previous simulation is that we are going to use the same heating, as the one for the CASO solution of Chapter 3. As we saw in the previous chapter, setting up a static dead zone, with the requirements to keep this zone static, discussed in §4.1.5, has the result that when we use this solution as an initial condition for a simulation, and evolve it with time, we obtain a final solution in which the dead zone is reshaped. Nevertheless, in realistic situations, the heat distribution might not be the one in which different processes like radiative cooling/heating by damping of Alfvén waves or heat deposited by accretion, are not balanced out.

Density contours and fieldlines, t=0.0

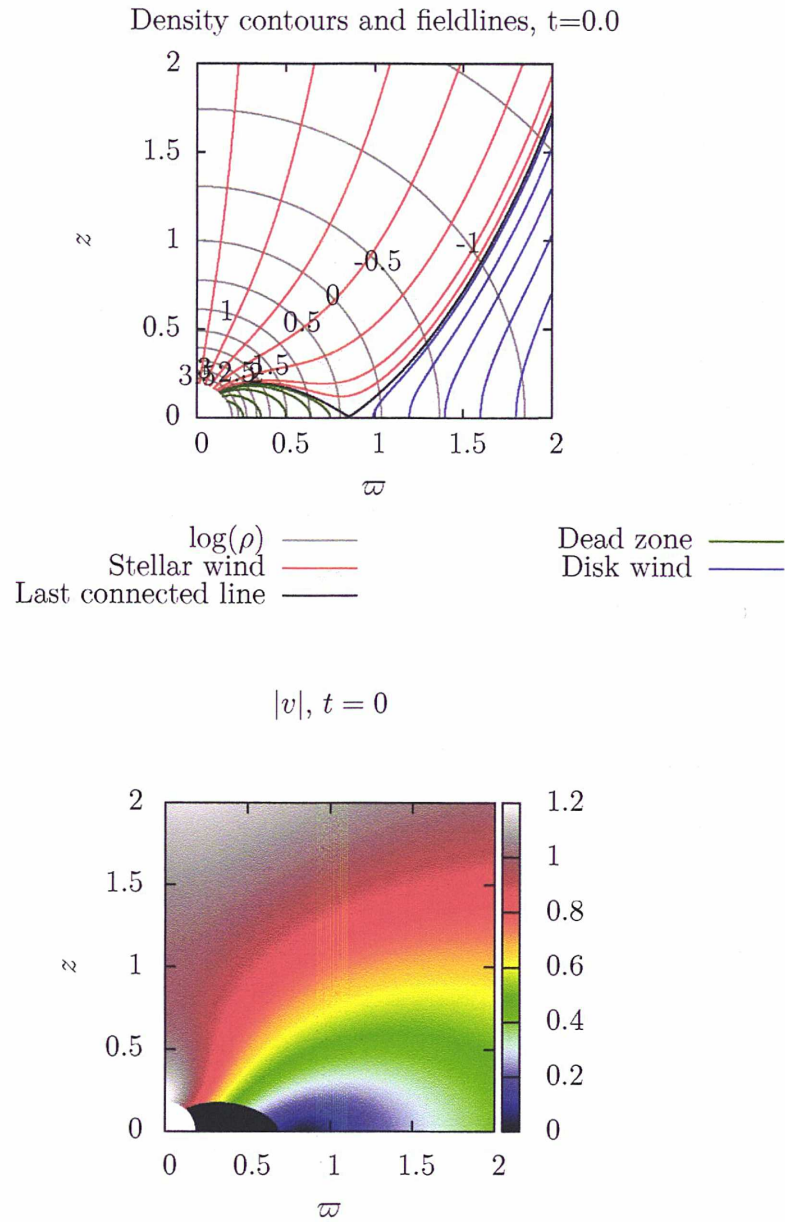| | log(ρ) —— | Dead zone —— |
| Stellar wind —— | | Disk wind —— |
| Last connected line —— | | |

$|v|$, $t = 0$

FIGURE 5.1: Once again, we start from the same initial setup, which we except is an educated guess for a solution with a dead zone. On the top panel we have density and fieldlines as well, on the bottom panel absolute value of the poloidal velocity
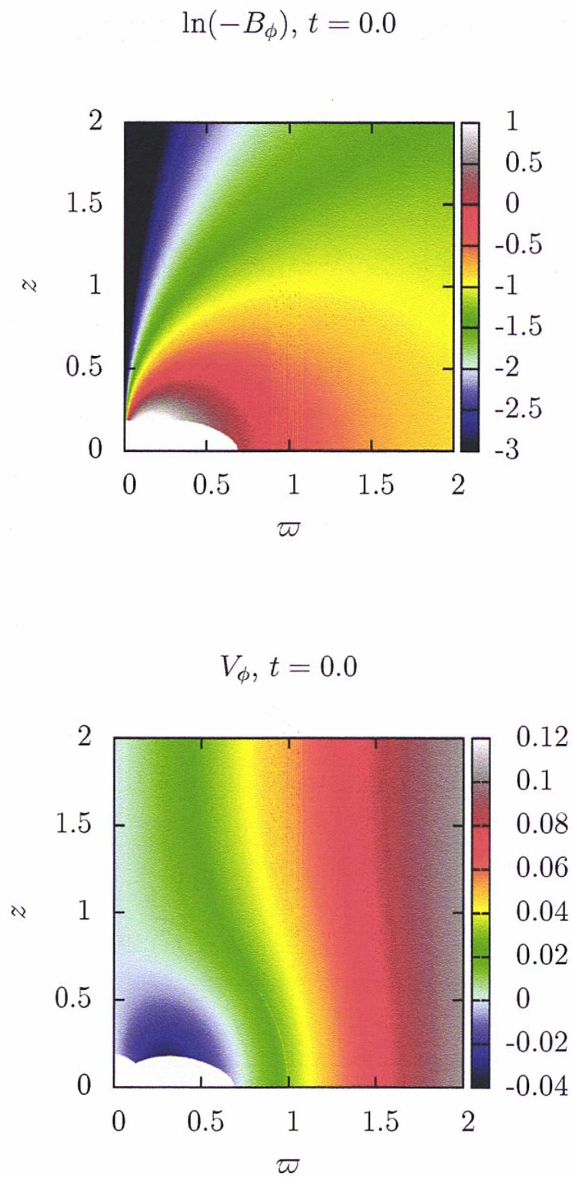
$\ln(-B_\phi)$, $t = 0.0$

V_ϕ, $t = 0.0$

FIGURE 5.2: On the top panel the toroidal component of the magnetic field and on the bottom panel rotationnal velocity

Regarding the simulation box, we will again be using the same mesh, as the one used for the simulations in Chapters 3 and 4, described in §3.2.

5.2   Outcome of the simulation: description of the final solution

As we can see from figure 5.3, the final state in this 'heated dead zone' solution is not significantly different from the cold dead zone one. As expected, matter is accelerated in the whole dead zone, but typical velocities are quite small and tend to zero towards the equator. Once again, the stellar wind component is not sensibly modified; the disk wind component is more distorted. The initial dead zone is reshaped again, but this time it has a final shape which is much closer to the initial one. This solution is similar to the cold dead zone one in an important aspect: the self-consistent setup, but this case with a dynamical magnetosphere, but still with no mass flux through the equator, solid rotation and vanishing toroidal component of the magnetic field. Indeed, on Fig. 5.3, we see in green the closed fieldlines of this solution. Note the specific form of the last connected line of this solution, which is almost coincidental to the last connected line of the CASO solution, used for initial condition. This last connected line has the same shape as the zone of the toroidal magnetic field, which is kept to 0 by the time evolution, and the zone in which the solid rotation is maintained during the simulation (see Fig.5.3). The difference with the previous case is that matter is not accumulated near the equator. This time, several fieldlines rooted on the star open up, but this time those are fieldlines rooted in a much smaller area on the inner boundary.

As we have done it for the previous cases, we are plotting the relative changes in all eight MHD quantities (see Appendix C). First, the pressure distribution (C.3) is almost identical to the initial distribution. This is

not a surprise, since the heating/cooling term $H - \Lambda$ in the energy equation (2.11) is computed in order to satisfy this equation. Let us have a look on the density distribution on Fig. C.1. The density in the heated dead zone solution is basically dropping by a factor of 2. Again, as in the Cold dead zone solution, this magnetosphere is hotter than the surrounding wind. Besides the fact that here the magnetosphere is dynamical, another important difference between this solution and the Cold dead zone solution is that jere, the self-consistent dead zone is not varying much in size and extent, *i.e.* the last closed fieldline is rooted approximately at the same angle at the inner boundary and the shape of the last closed fieldline is almost identical to that of the initial condition.

5.3   Conserved quantities

On Figure 5.6 we are plotting the plasma β parameter. As in the case of the Cold dead zone solution, the low value of this parameter close to the inner boundary and the equator is maintained to its low levels, as it is required in order to keep a plasma in static equilibrium. The plasma β is indeed increasing as we look above the dead zone, but unlike the previous case, where fieldlines open up and empty the vicinity of the dead zone, now we are in a situation where the matter is accelerated and flowing along the last connected line (note how this time we do not have null velocities on the interface dead zone/stellar wind), which explains why the thermal pressure is bigger than the corresponding region.

Concerning Ψ_A (Fig. 5.5), the mass-to-magnetic flux ratio, we note again the sensitive behaviour of this quantity. Nevertheless, Ψ_A contours are almost parallel to the fieldlines in the stellar wind part of the solution, and as we discussed for the two previous solutions, is showing a sensitive behaviour in the region in the interface of the stellar and the disk wind.

Density contours and fieldlines, t=50.0

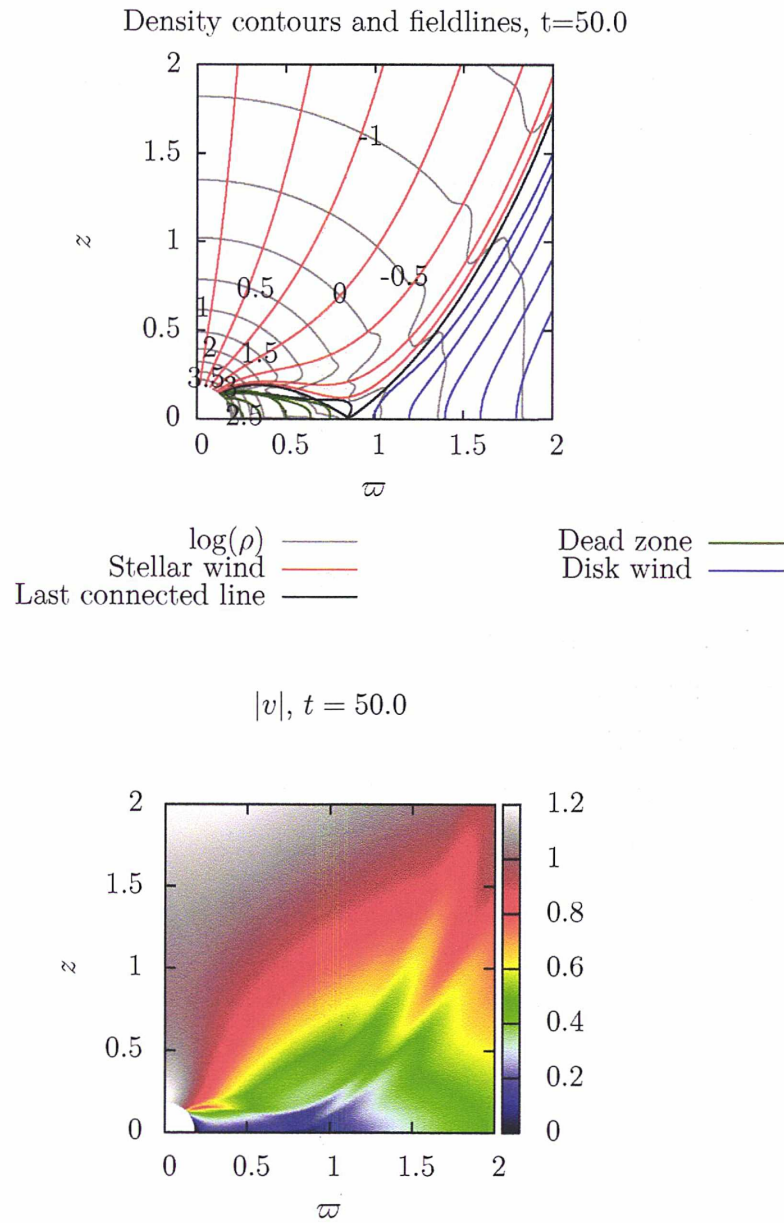|	
$\log(\rho)$ ——	Dead zone ——
Stellar wind ——	Disk wind ——
Last connected line ——	

$|v|$, $t = 50.0$

FIGURE 5.3: The quantities, plotted on Figure 5.1, are shown at their final state. Note the shape of the last closed fieldline. It will define the size of the self-consistent dead zone, as in the Cold dead zone solution
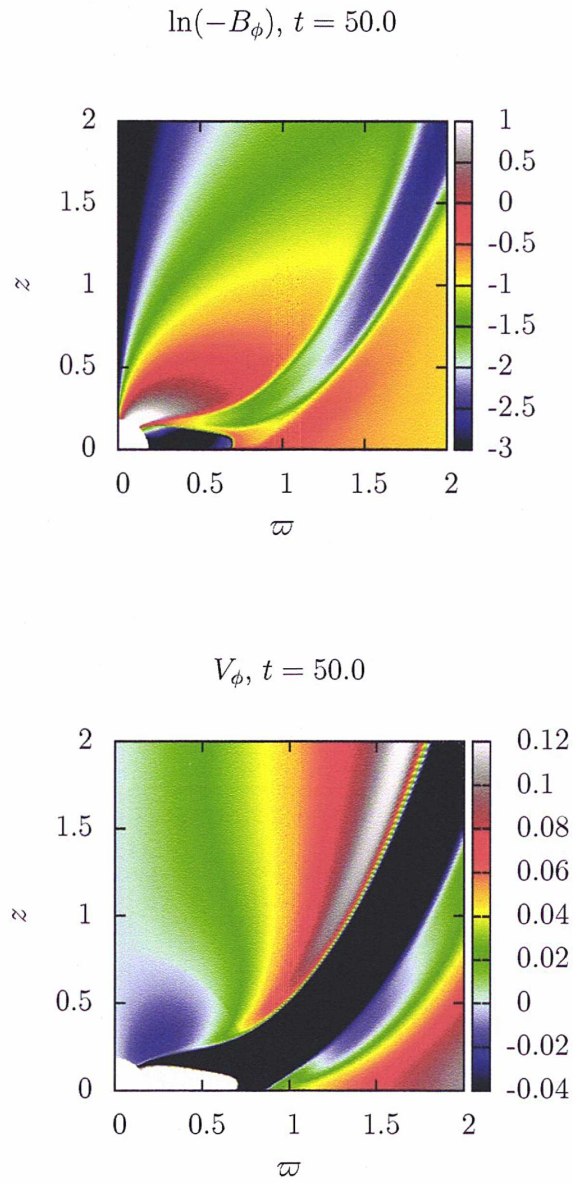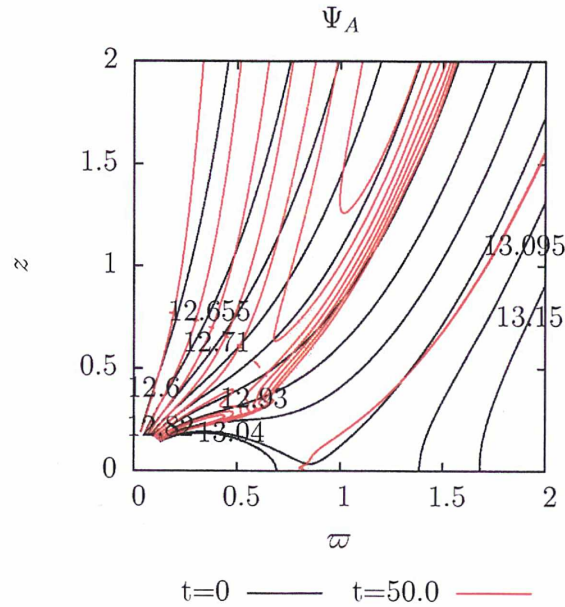
$$\ln(-B_\phi),\, t = 50.0$$

$$V_\phi,\, t = 50.0$$

FIGURE 5.4: The same quantities as Figure 5.2 and are plotted here. We note the characteristic shape of the zone, in which $B_\phi = 0$ and V_ϕ corresponds to solid rotation, which has the same shape as the form of the last closed fieldline on Fig. 5.3

FIGURE 5.5: Contour plot of Ψ_A, for $t = 0.0$ and $t = 50.0t_*$

The specific angular momentum L (5.8) and the total angular momentum ρL (Fig. 5.7) are again quite close to their initial distributions. Similar effects are those observed in the Cold dead zone solution are also observed here. As in the Cold dead zone case, lines of equal L are a bit closer to the axis than in the initial condition. As L increases with θ, this means that the stellar wind is carrying a slightly bigger angular momentum than the stellar wind of the CASO solution. Indeed, we see that the last connected line is at slightly bigger θ than at $t = 0$, but as we showed in the Cold dead zone case, this is not affecting much the angular momentum flux. We are also going to plot, as in the case of the Cold dead zone solution, the torque τ throughout the simulation (Fig. 5.9). We again see that the contours of equal τ are not significantly different, in the stellar wind region, than the torque of the CASO solution. We are going to conclude that this stellar wind is braking the star the same manner as the stellar wind of the CASO solution.
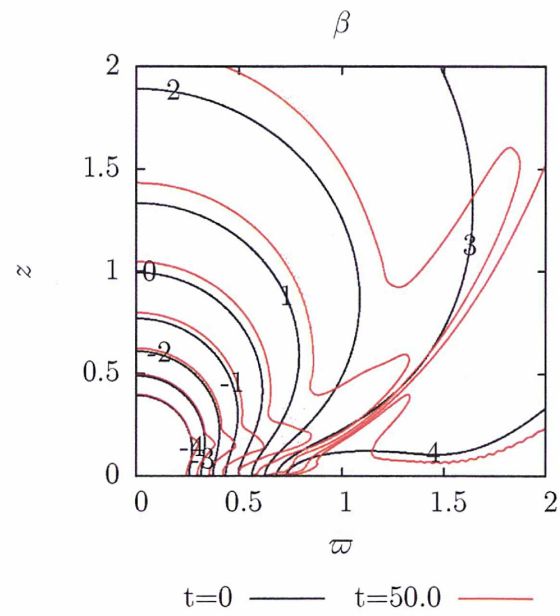
FIGURE 5.6: The plasma β throughout the simulation
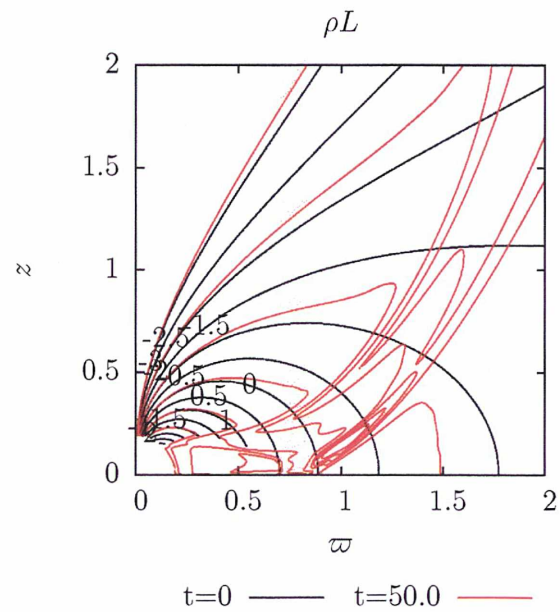
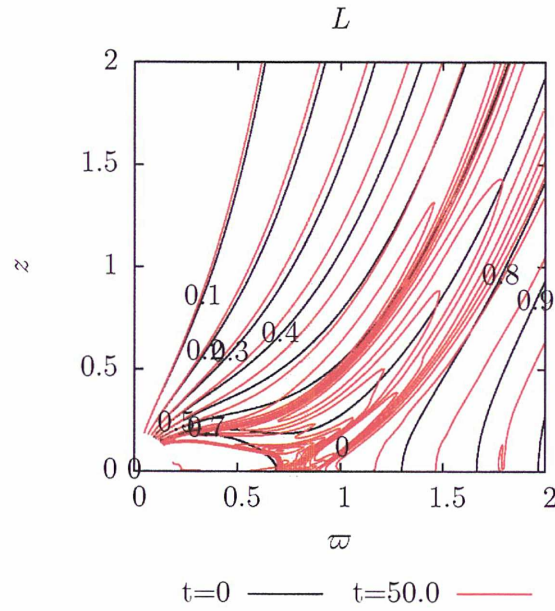FIGURE 5.7: The total angular momentum L throughout the simulation

L

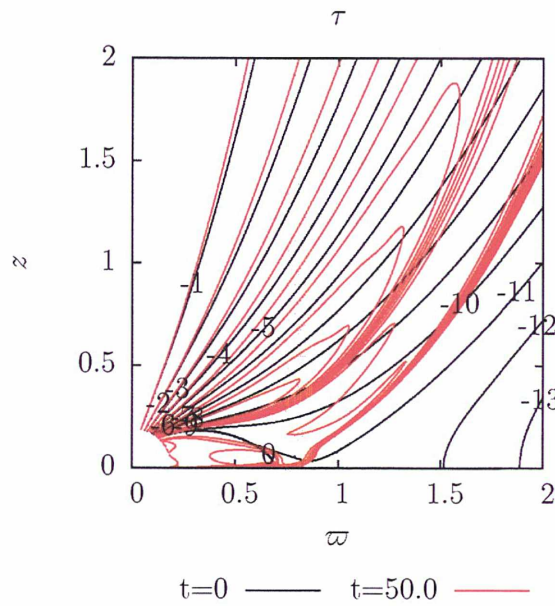FIGURE 5.8: The specific angular momentum L throughout the simulation

τ

FIGURE 5.9: The torque τ throughout the simulation

Chapter 6

Conclusion

The goal of this thesis was to gain insight in the physical properties YSO jets with self-consistent magnetospheres. We based this work on previously obtained semi-analytical solutions, providing the geometrical framework needed to study YSO jets, and used the semi-analytical solutions as initial conditions of a numerical simulation box. This solution, on which we extensively discussed in Chapter 3, is obtained under reasonnable hypotheses, and was proven, in this work, to be topologically stable. This means that when introduced in a MHD simulation, all quantities converged to a steady, stationnary state. The importance of this finding is that by proving that we have a stable, from MHD point of view solution, we could discuss on the physical meaning of the potentially observable quantities. The question of the stability was not trivial, because in order to ensure that the eight MHD quantities, in the form they were written under the self-similar hypothesis, are solutions of the equations of ideal MHD we ought to employ a non-polytropic heating function. We have shown that the three main parts of the solution: the stellar wind component, the disk wind component and the magnetosphere with closed fieldlines are structurally stable, that they keep their positions and properties, but that we should proceed with caution when discussing the interface region between the stellar and the disk wind.

In Chapters 4 and 5, we have explored two different ways of modifying the semi-analytical solution. This was needed in order to obtain numerical solutions, accounting for a self-consistent magnetosphere, which we defined as a magnetosphere with no mass flux through the equator, and by accounting for the consequences of such a constraint, imposed by the equations of ideal MHD. The employed method is an illustration of the potential of the combination of analytical and numerical methods for the study of the astrophysical problem. The mixed approach consists of using the semi-analytical solution, which topological stability we tested, but by simply suppressing the mass flux along the closed magnetic fieldlines. This initial condition was then evolved with the numerical tool, which is the PLUTO code. We proved that even with the modifications we introduced, the stellar wind component is topologically stable, and also the disk wind component. In the case of the non heated magnetosphere, which we introduced in Chapter 4, we have found that initially closed fieldlines, anchored close to the stellar wind open up, hence decreasing the extent of the dead zone as seen from the stellar surface, and that those lines pinch the magnetosphere, decreasing significantly its size, and giving it a particular helmet-type structure. We argue that this smaller magnetosphere is in better agreement with the observations that the unmodified semi-analytical solution, as the modified solution predicts a magnetosphere with a typical size twice as smaller as the unmodified solution for the same strength of the stellar magnetic field. We presented another solution, in which the stellar and the disk wind are again topologically stable, and in which the size of the self-consistent magnetosphere is practically the same as the initial one. This is achieved by restoring the non-polytropic heating in this zone. By this, we argue, we could model magnetospheres with different sizes for the same magnetic field. The non heated magnetosphere corresponds to a case where all the processes, contributing to heating balance out those who contribute to cooling, and in the case of the heated dead zone where the heating is much larger than the cooling. Proving that in both cases

we have topologically stable, self-consistent magnetospheres, which introduction is not dramatically changing the semi-anaytical solution, and hence astrophysical conclusions are appropriate. This is also a hint that in future, we could also model intermediate cases, where for example we could model contributions to heating from different physical processes, and most importantly, include a more precise model of the disk wind part, by including an α-disk in the box and model in a more precise way the disk wind part of the jet.

Appendix A

Normalized deviations between the final and initial state for the CASO solution

A.1   Density

Relative differences $\left(\dfrac{\rho(t=50) - \rho(t=0)}{\rho(t=0)}\right)$ are plotted on Fig. A.1 and A.2

A.2   Pressure

Relative differences $\left(\dfrac{P(t=50) - P(t=0)}{P(t=0)}\right)$ are plotted on Fig. A.3 and A.4

A.3 B_R

Relative differences $\left(\dfrac{B_R(t=50) - B_R(t=0)}{B_R(t=0)}\right)$ are plotted on Fig. A.5 and A.6

123

A.4 B_θ

Relative differences $\left(\dfrac{B_\theta(t=50) - B_\theta(t=0)}{B_\theta(t=0)}\right)$ are plotted on Fig. A.7 and A.8

A.5 B_ϕ

Relative differences $\left(\dfrac{B_\phi(t=50) - B_\phi(t=0)}{B_\phi(t=0)}\right)$ are plotted on Fig. A.9 and A.10

A.6 V_R

Relative differences $\left(\dfrac{V_R(t=50) - V_R(t=0)}{V_R(t=0)}\right)$ are plotted on Fig. A.11 and A.12

A.7 V_θ

Relative differences $\left(\dfrac{V_\theta(t=50) - V_\theta(t=0)}{V_\theta(t=0)}\right)$ are plotted on Fig. A.13 and A.14

A.8 $V\phi$

Relative differences $\left(\dfrac{V_\phi(t=50) - V_\phi(t=0)}{V_\phi(t=0)}\right)$ are plotted on Fig. A.15 and A.16

$$\frac{\rho(t=50) - \rho(t=0)}{\rho(t=0)}$$
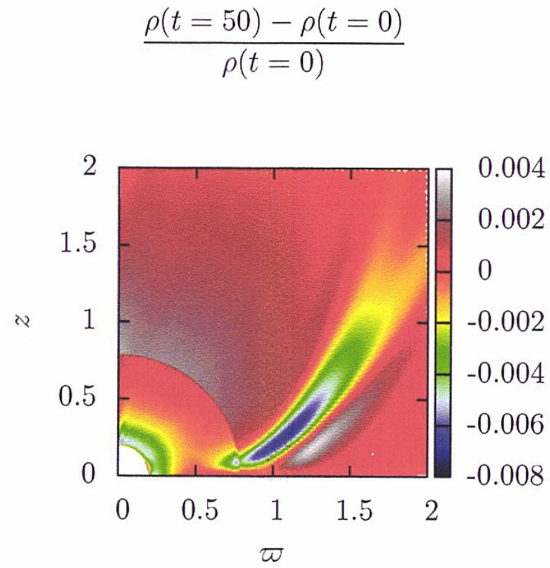
FIGURE A.1: Relative change in density on the ejection scale

$$\frac{\rho(t=50) - \rho(t=0)}{\rho(t=0)}$$
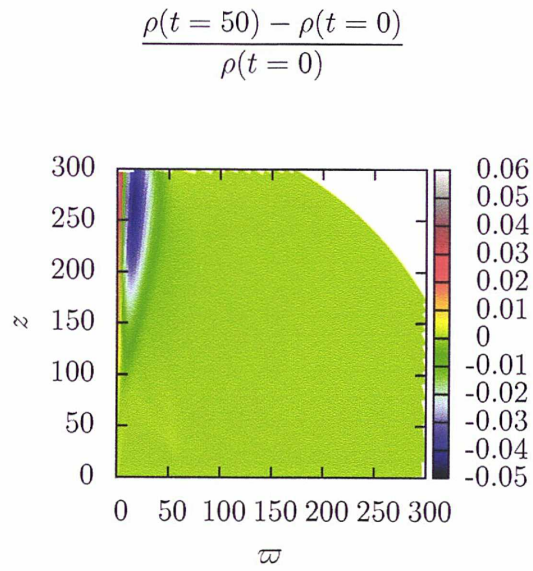
FIGURE A.2: Relative change in density on the propagation scale

$$\frac{P(t=50) - P(t=0)}{P(t=0)}$$
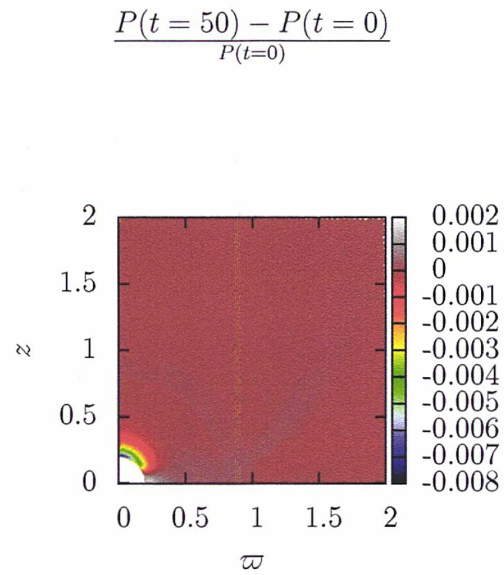
FIGURE A.3: Relative change in pressure on the ejection scale

$$\frac{P(t=50) - P(t=0)}{P(t=0)}$$
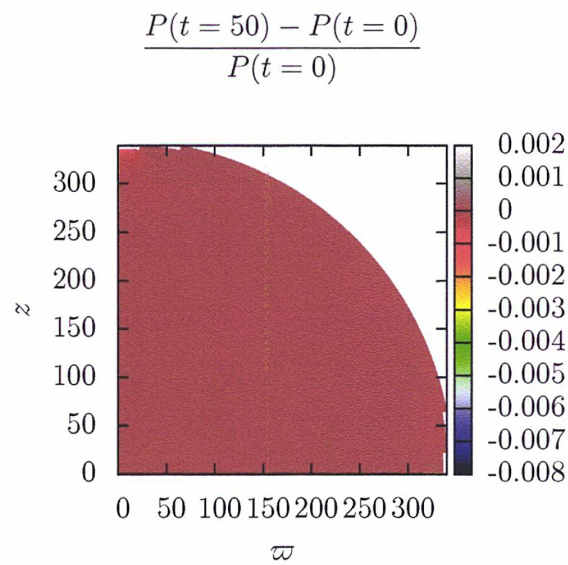
FIGURE A.4: Relative change in pressure on the propagation scale

$$\frac{B_R(t=50) - B_R(t=0)}{B_R(t=0)}$$
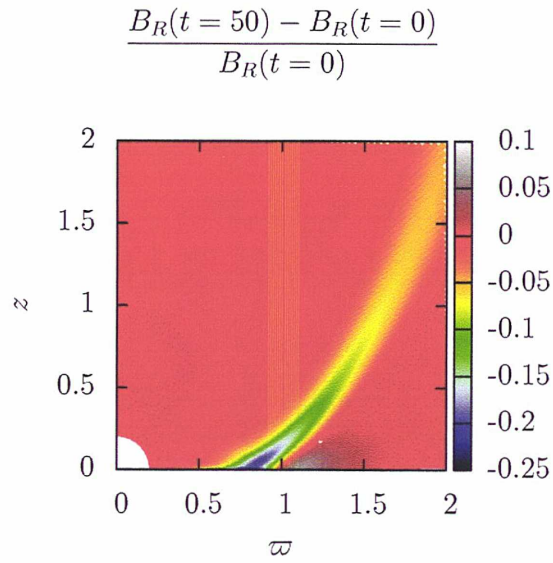
FIGURE A.5: Relative change in radial magnetic field on the ejection scale

$$\frac{B_R(t=50) - B_R(t=0)}{B_R(t=0)}$$
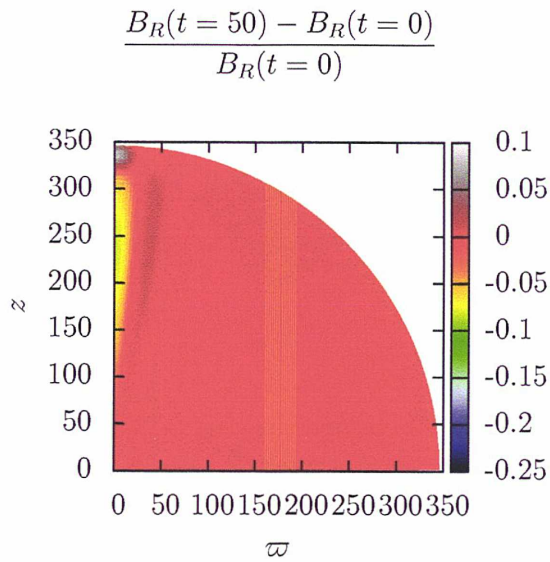
FIGURE A.6: Relative change in radial magnetic field on the propagation scale
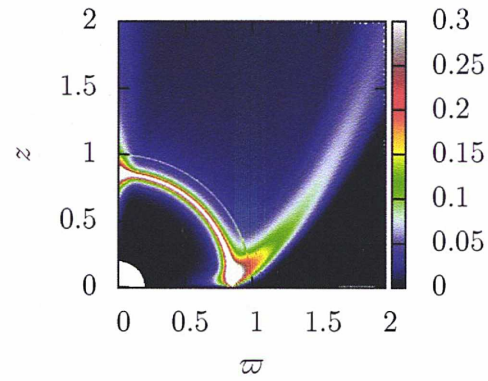
$$\frac{B_\theta(t=50) - B_\theta(t=0)}{B_\theta(t=0)}$$

FIGURE A.7: Relative change in longitudinal magnetic field on the ejection scale
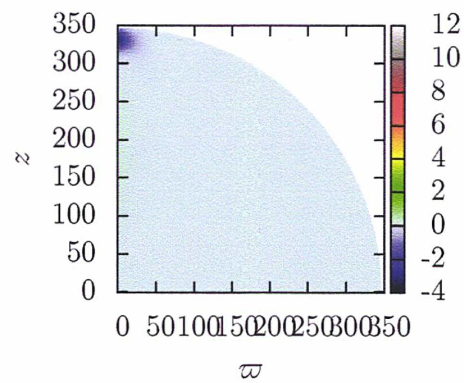
$$\frac{B_\theta(t=50) - B_\theta(t=0)}{B_\theta(t=0)}$$

FIGURE A.8: Relative change in longitudinal magnetic field on the propagation scale

$$\frac{B_\phi(t=50) - B_\phi(t=0)}{B_\phi(t=0)}$$

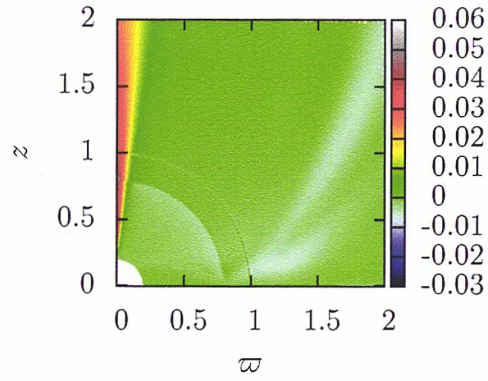FIGURE A.9: Relative change in toroidal magnetic field on the ejection scale
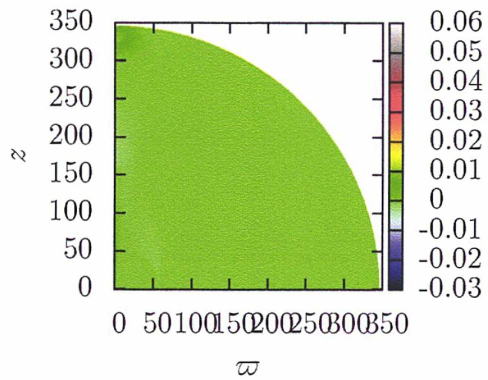
$$\frac{B_\phi(t=50) - B_\phi(t=0)}{B_\phi(t=0)}$$

FIGURE A.10: Relative change in toroidal magnetic field on the propagation scale

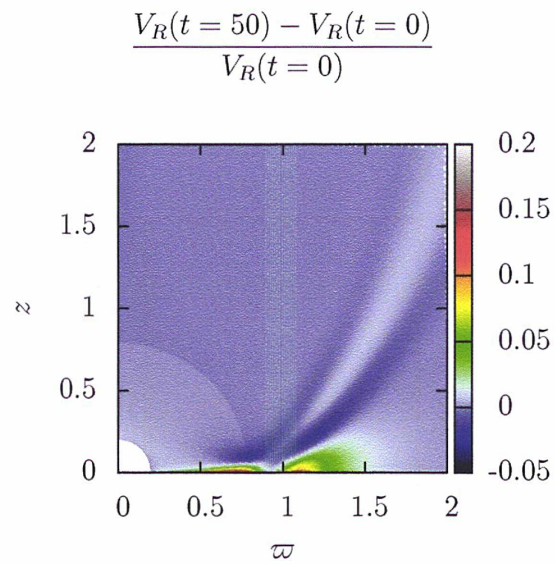$$\frac{V_R(t=50) - V_R(t=0)}{V_R(t=0)}$$

FIGURE A.11: Relative change in radial velocity on the ejection scale
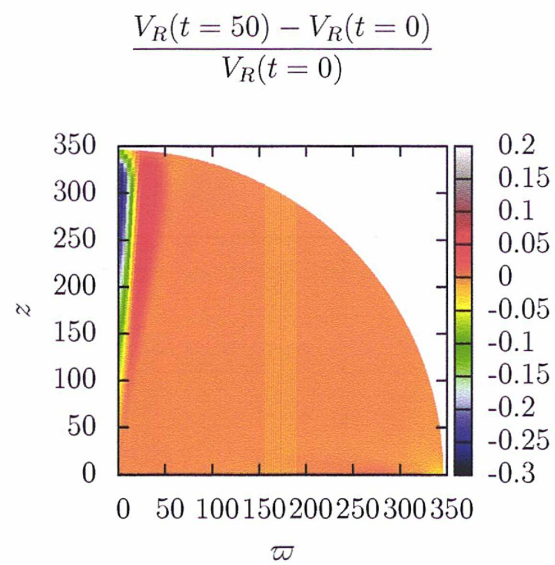
$$\frac{V_R(t=50) - V_R(t=0)}{V_R(t=0)}$$

FIGURE A.12: Relative change in radial velocity on the propagation scale

$$\frac{V_\theta(t=50) - V_\theta(t=0)}{V_\theta(t=0)}$$
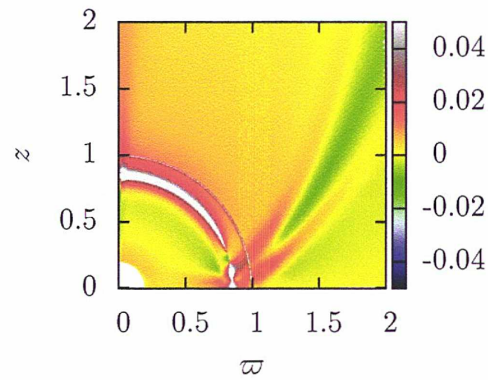

FIGURE A.13: Relative change in longitudinal velocity on the ejection scale

$$\frac{V_\theta(t=50) - V_\theta(t=0)}{V_\theta(t=0)}$$

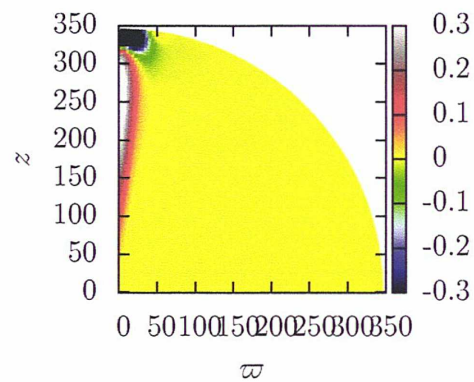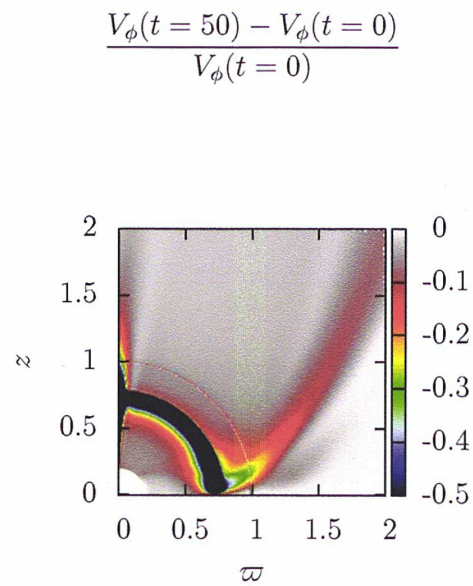FIGURE A.14: Relative change in longitudinal velocity on the propagation scale

$$\frac{V_\phi(t=50) - V_\phi(t=0)}{V_\phi(t=0)}$$

FIGURE A.15: Relative change in toroidal velocity on the ejection scale

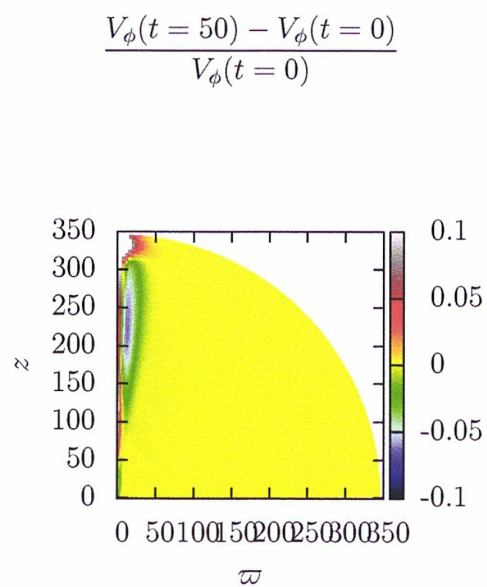$$\frac{V_\phi(t=50) - V_\phi(t=0)}{V_\phi(t=0)}$$

FIGURE A.16: Relative change in toroidal velocity on the propagation scale

Appendix B

Normalized deviations between the final and initial state for the Cold dead zone solution

B.1 Density

Relative differences $\left(\dfrac{\rho(t=4) - \rho(t=0)}{\rho(t=0)} \right)$ and $\left(\dfrac{\rho(t=20) - \rho(t=4)}{\rho(t=0)} \right)$ are plotted on Fig. B.1 and B.2

B.2 Pressure

Relative differences $\left(\dfrac{P(t=4) - P(t=0)}{P(t=0)} \right)$ and $\left(\dfrac{P(t=20) - P(t=4)}{P(t=4)} \right)$ are plotted on Fig. B.3 and B.4

B.3 B_R

Relative differences $\left(\dfrac{B_R(t=4) - B_R(t=0)}{B_R(t=0)} \right)$ and $\left(\dfrac{B_R(t=20) - B_R(t=4)}{B_R(t=4)} \right)$ are plotted on Fig. B.5 and B.6

B.4 B_θ

Relative differences $\left(\dfrac{B_\theta(t=4) - B_\theta(t=0)}{B_\theta(t=0)} \right)$ and $\left(\dfrac{B_\theta(t=20) - B_\theta(t=4)}{B_\theta(t=4)} \right)$
are plotted on Fig. B.7 and B.8

B.5 B_ϕ

Relative differences $\left(\dfrac{B_\phi(t=4) - B_\phi(t=0)}{B_\phi(t=0)} \right)$ and $\left(\dfrac{B_\phi(t=20) - B_\phi(t=4)}{B_\phi(t=4)} \right)$
are plotted on Fig. B.9 and B.10

B.6 V_R

Relative differences $\left(\dfrac{V_R(t=4) - V_R(t=0)}{V_R(t=0)} \right)$ and $\left(\dfrac{V_R(t=20) - V_R(t=4)}{V_R(t=4)} \right)$
are plotted on Fig. B.11 and B.12

B.7 V_θ

Relative differences $\left(\dfrac{V_\theta(t=4) - V_\theta(t=0)}{V_\theta(t=0)} \right)$ and $\left(\dfrac{V_\theta(t=20) - V_\theta(t=4)}{V_\theta(t=4)} \right)$
are plotted on Fig. B.13 and B.14

B.8 $V\phi$

Relative differences $\left(\dfrac{V_\phi(t=4) - V_\phi(t=0)}{V_\phi(t=0)} \right)$ and $\left(\dfrac{V_\phi(t=20) - V_\phi(t=4)}{V_\phi(t=4)} \right)$
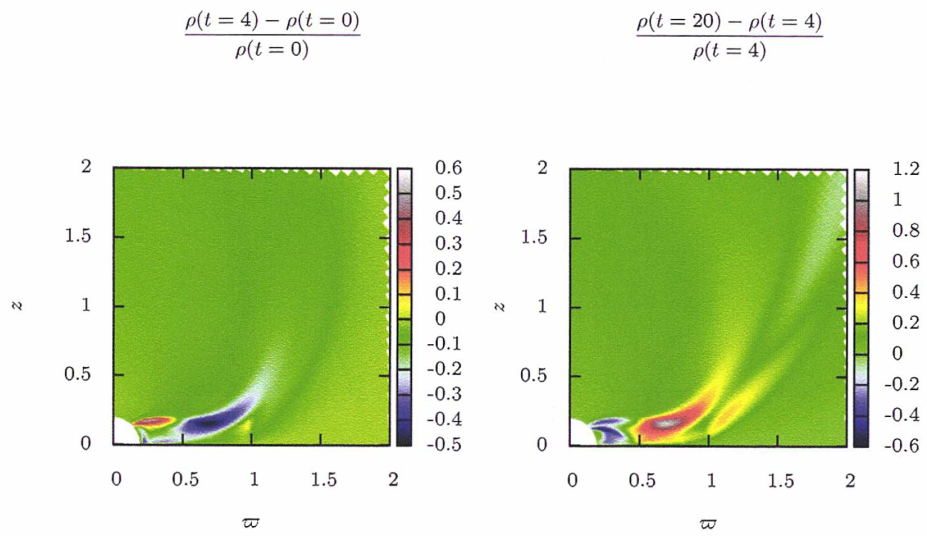are plotted on Fig. B.15 and B.16

$$\frac{\rho(t=4) - \rho(t=0)}{\rho(t=0)} \qquad\qquad \frac{\rho(t=20) - \rho(t=4)}{\rho(t=4)}$$

FIGURE B.1: Relative change in density on the ejection scale

$$\frac{\rho(t=4) - \rho(t=0)}{\rho(t=0)} \qquad\qquad \frac{\rho(t=20) - \rho(t=4)}{\rho(t=4)}$$
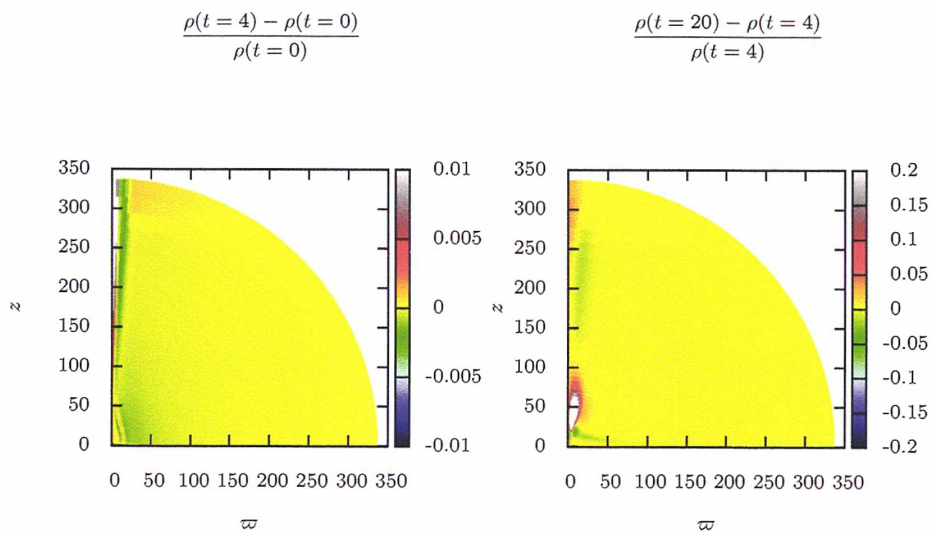
FIGURE B.2: Relative change in density on the propagation scale

$$\frac{P(t=4) - P(t=0)}{P(t=0)}$$

$$\frac{P(t=20) - P(t=4)}{P(t=4)}$$
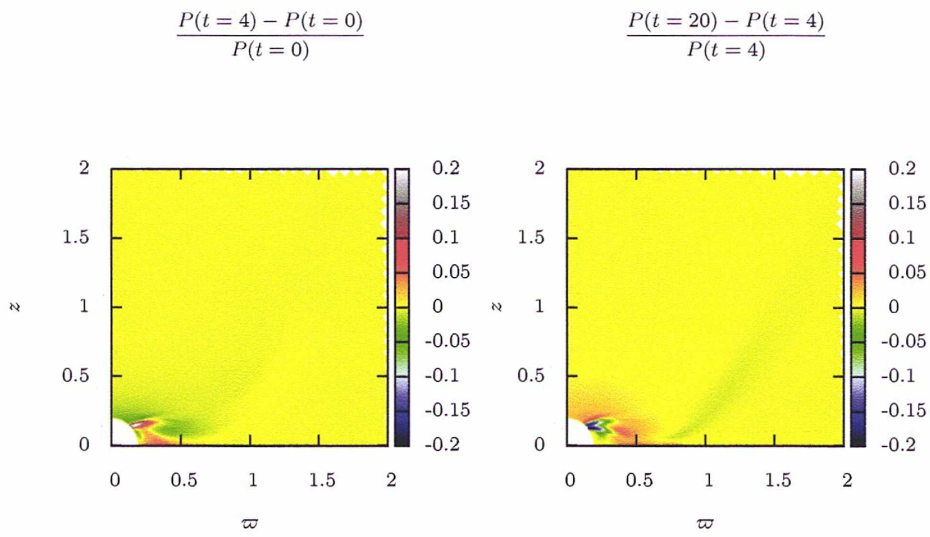
FIGURE B.3: Relative change in pressure on the ejection scale

$$\frac{P(t=4) - P(t=0)}{P(t=0)}$$

$$\frac{P(t=20) - P(t=4)}{P(t=4)}$$
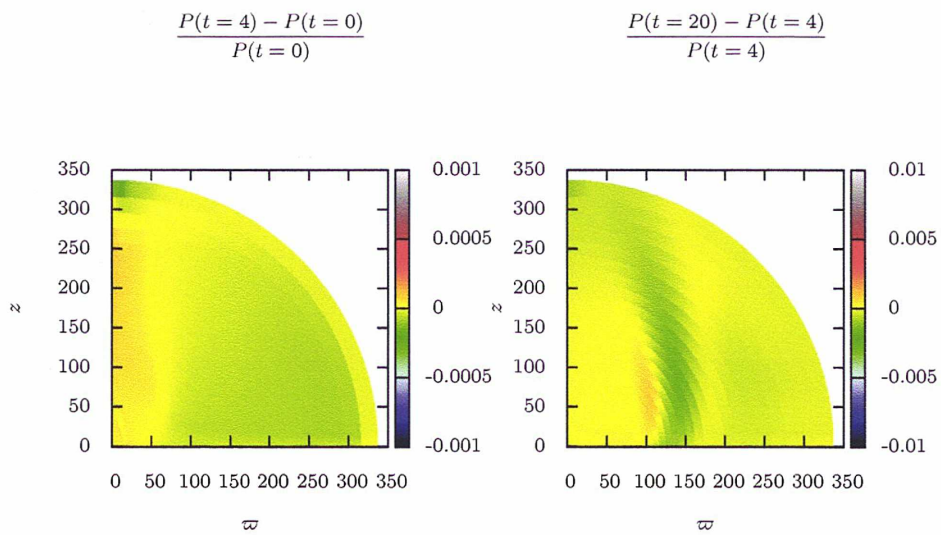
FIGURE B.4: Relative change in pressure on the propagation scale

$$\frac{B_r(t=4) - B_r(t=0)}{B_r(t=0)} \qquad \frac{B_r(t=20) - B_r(t=4)}{B_r(t=4)}$$
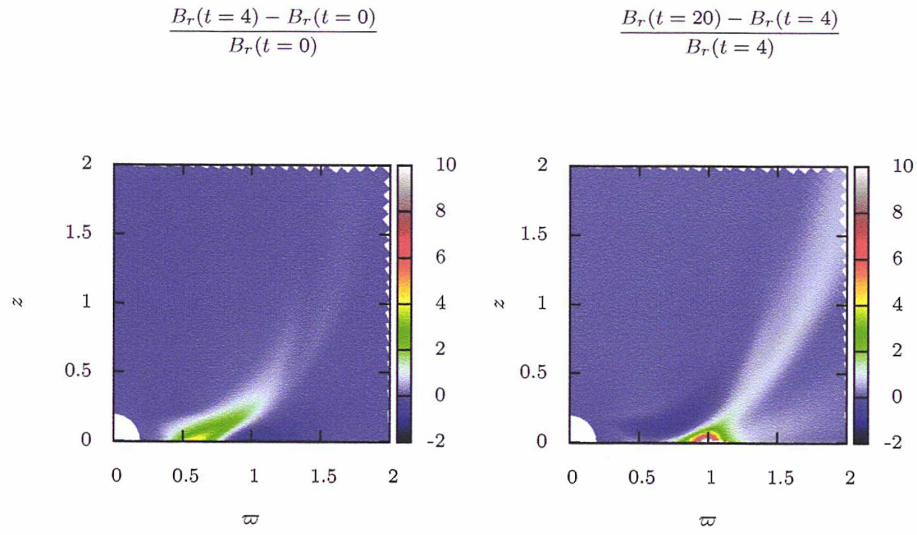
FIGURE B.5: Relative change in radial magnetic field on the ejection scale

$$\frac{B_r(t=4) - B_r(t=0)}{B_r(t=0)} \qquad \frac{B_r(t=20) - B_r(t=4)}{B_r(t=4)}$$
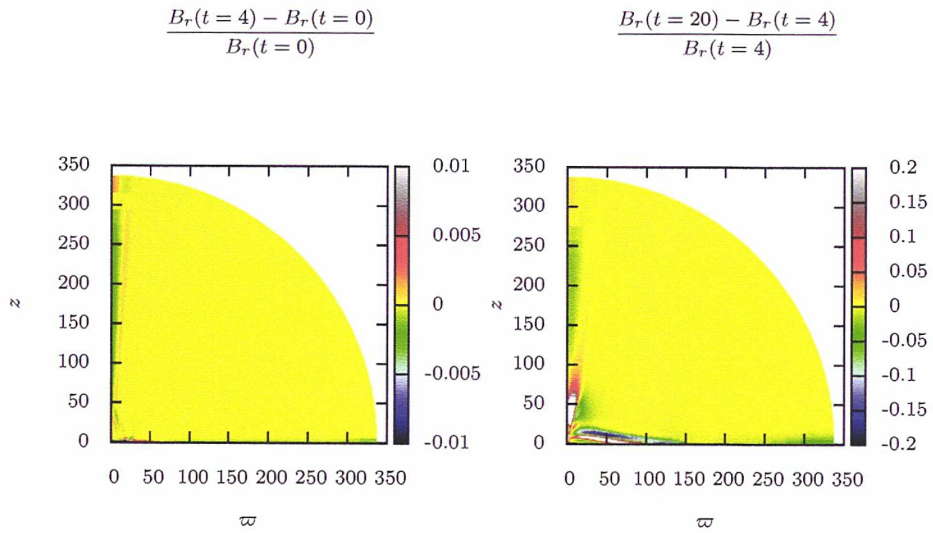
FIGURE B.6: Relative change in radial magnetic field on the propagation scale

$$\frac{B_\theta(t=4) - B_\theta(t=0)}{B_\theta(t=0)} \qquad\qquad \frac{B_\theta(t=20) - B_\theta(t=4)}{B_\theta(t=4)}$$
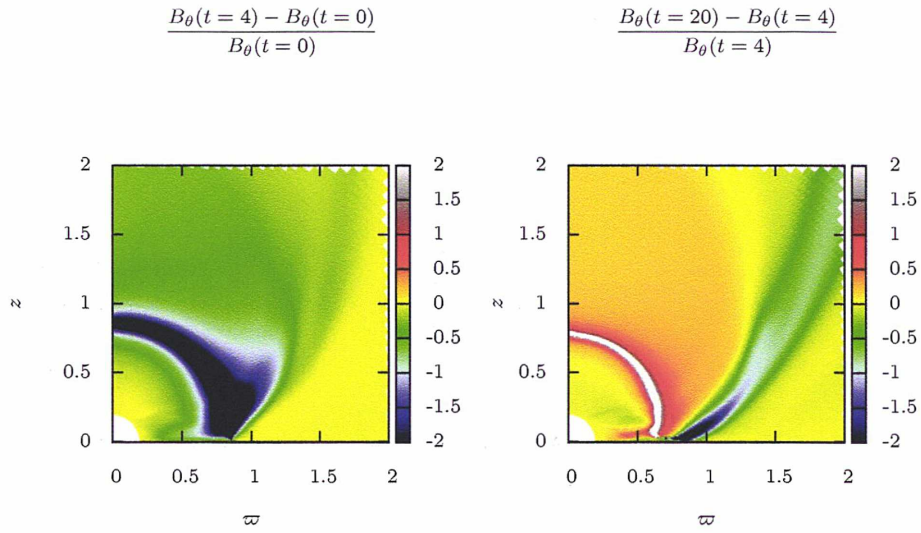
FIGURE B.7: Relative change in longitudinal magnetic field on the ejection scale

$$\frac{B_\theta(t=4) - B_\theta(t=0)}{B_\theta(t=0)} \qquad\qquad \frac{B_\theta(t=20) - B_\theta(t=4)}{B_\theta(t=4)}$$
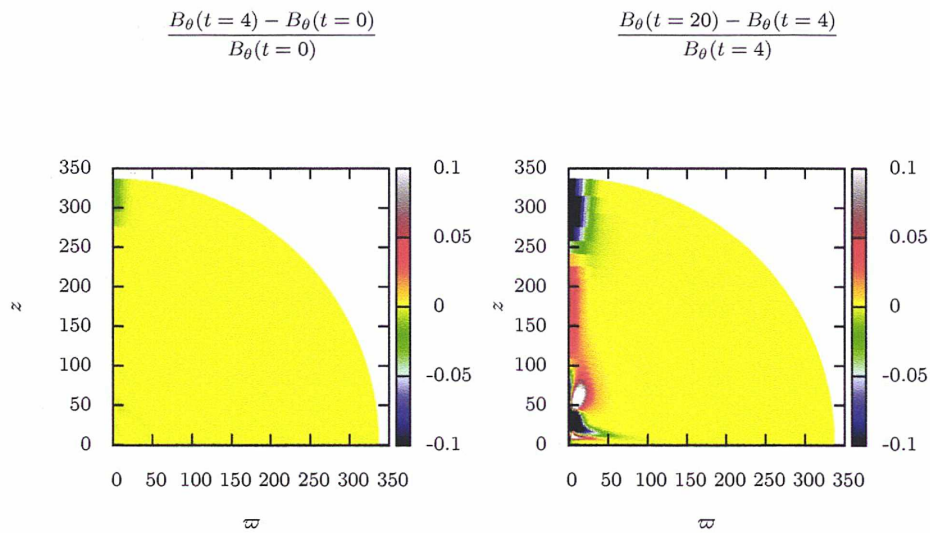
FIGURE B.8: Relative change in longitudinal magnetic field on the propagation scale

$$\frac{B_\phi(t=4) - B_\phi(t=0)}{B_\phi(t=0)} \qquad\qquad \frac{B_\phi(t=20) - B_\phi(t=4)}{B_\phi(t=4)}$$
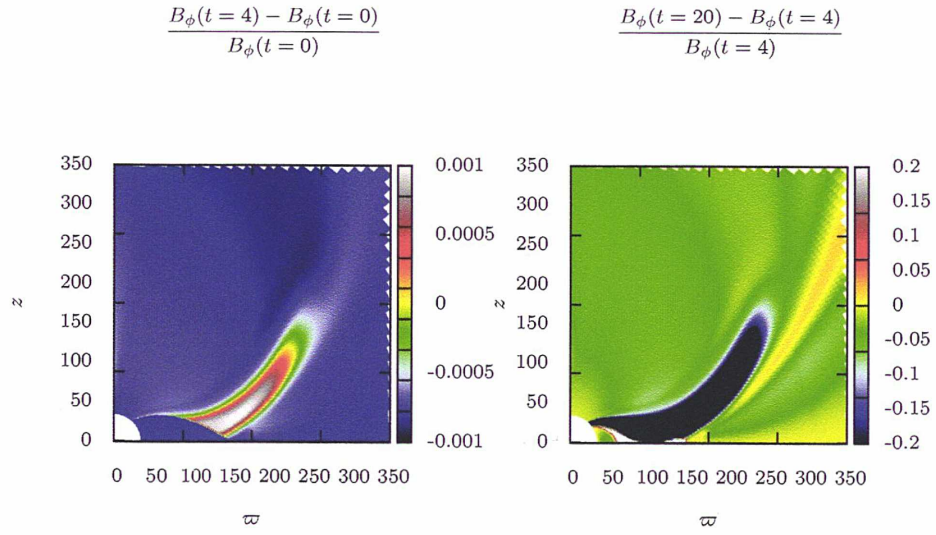
FIGURE B.9: Relative change in toroidal magnetic field on the ejection scale

$$\frac{B_\phi(t=4) - B_\phi(t=0)}{B_\phi(t=0)} \qquad\qquad \frac{B_\phi(t=20) - B_\phi(t=4)}{B_\phi(t=4)}$$
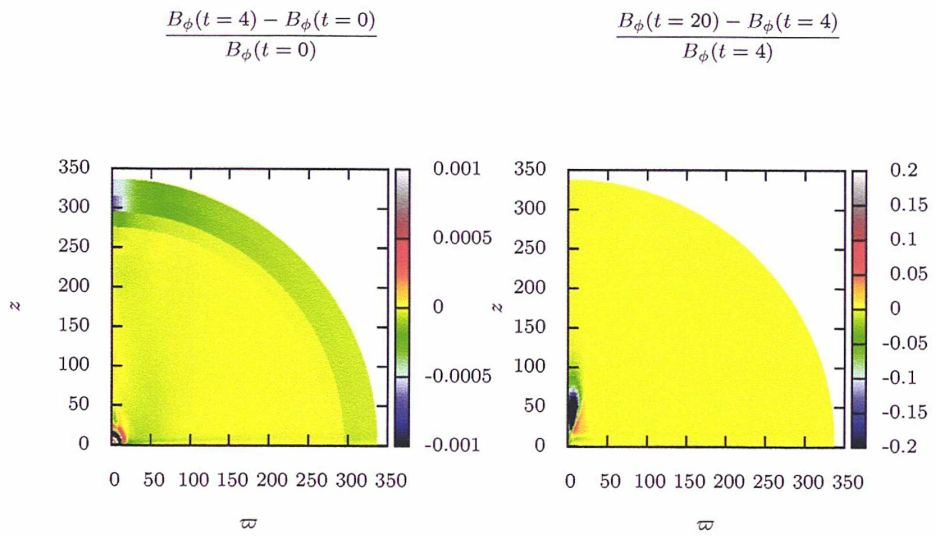
FIGURE B.10: Relative change in toroidal magnetic field on the propagation scale

$$\frac{V_r(t=4) - V_r(t=0)}{V_r(t=0)}$$

$$\frac{V_r(t=20) - V_r(t=4)}{V_r(t=4)}$$
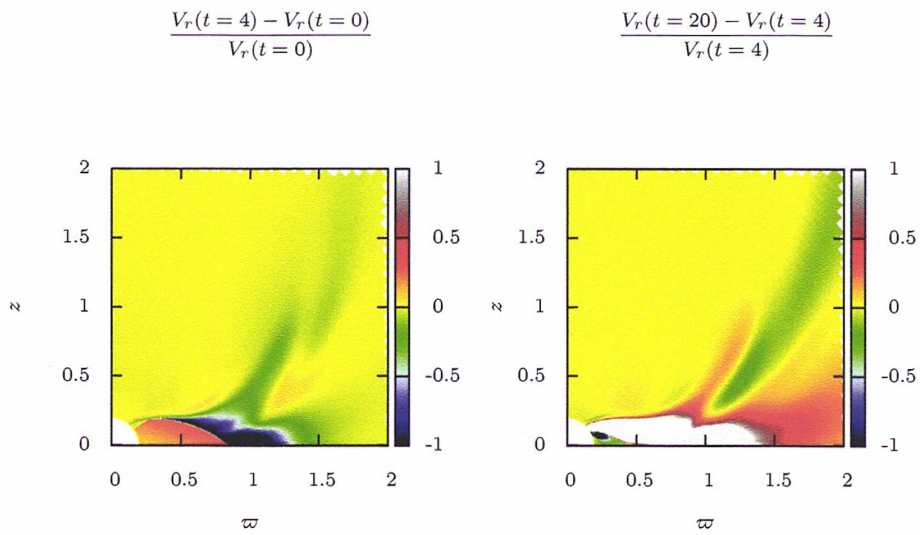
FIGURE B.11: Relative change in radial velocity on the ejection scale

$$\frac{V_r(t=4) - V_r(t=0)}{V_r(t=0)}$$

$$\frac{V_r(t=20) - V_r(t=4)}{V_r(t=4)}$$
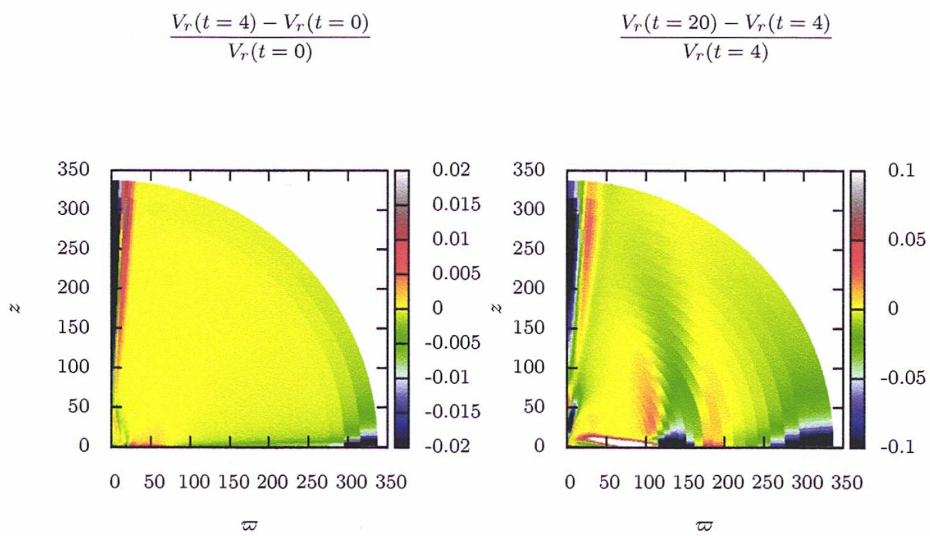
FIGURE B.12: Relative change in radial velocity on the propagation scale

$$\frac{V_\theta(t=4) - V_\theta(t=0)}{V_\theta(t=0)} \qquad\qquad \frac{V_\theta(t=20) - V_\theta(t=4)}{V_\theta(t=4)}$$
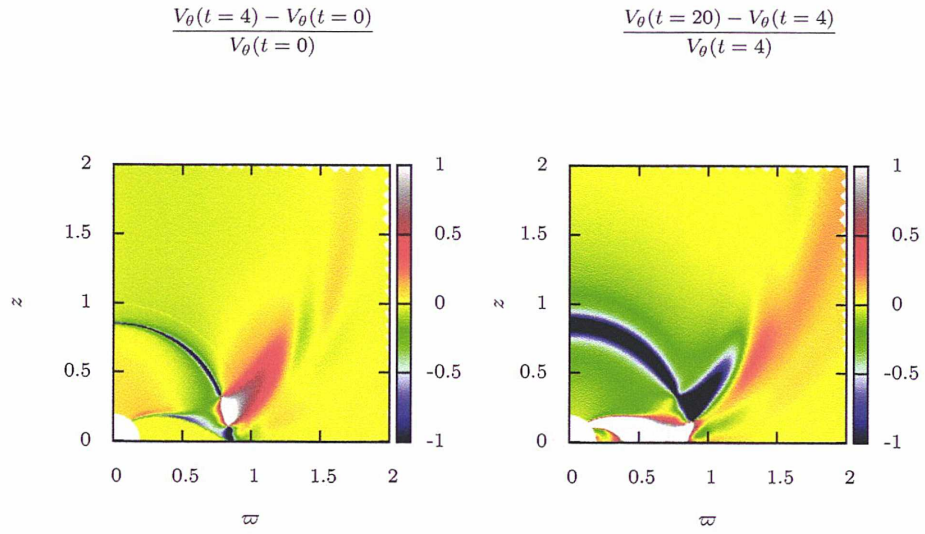
FIGURE B.13: Relative change in longitudinal velocity on the ejection scale

$$\frac{V_\theta(t=4) - V_\theta(t=0)}{V_\theta(t=0)} \qquad\qquad \frac{V_\theta(t=20) - V_\theta(t=4)}{V_\theta(t=4)}$$
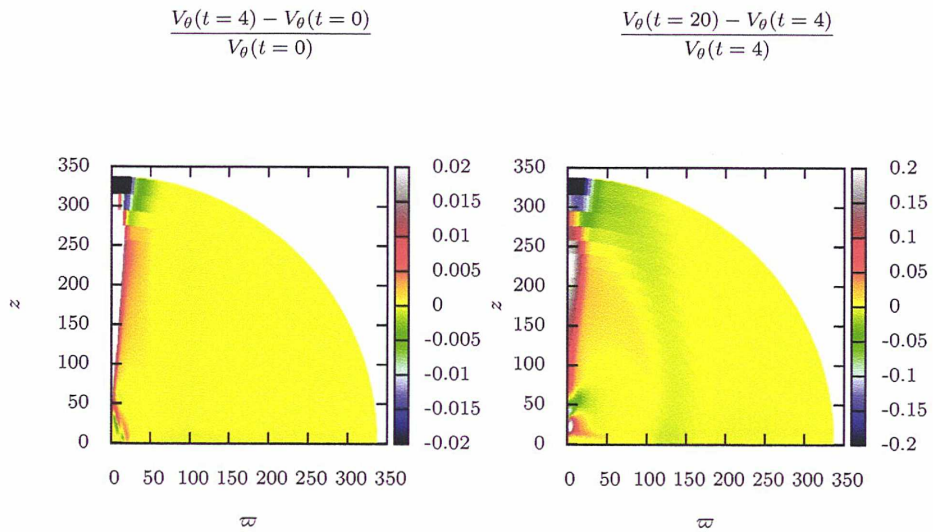
FIGURE B.14: Relative change in longitudinal velocity on the propagation scale

$$\frac{V_\phi(t=4) - V_\phi(t=0)}{V_\phi(t=0)} \qquad\qquad \frac{V_\phi(t=20) - V_\phi(t=4)}{V_\phi(t=4)}$$
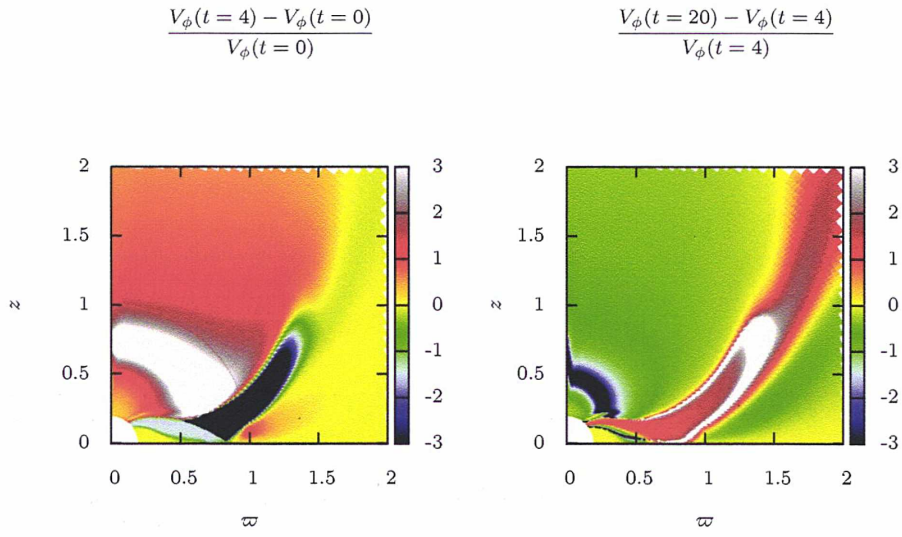
FIGURE B.15: Relative change in toroidal velocity on the ejection scale

$$\frac{V_\phi(t=4) - V_\phi(t=0)}{V_\phi(t=0)} \qquad\qquad \frac{V_\phi(t=20) - V_\phi(t=4)}{V_\phi(t=4)}$$

FIGURE B.16: Relative change in toroidal velocity on the propagation scale

Appendix C

Normalized deviations between the final and initial state for the Heated dead zone solution

C.1 Density

Relative differences $\left(\dfrac{\rho(t=50) - \rho(t=0)}{\rho(t=0)} \right)$ are plotted on Fig. C.1 and C.2
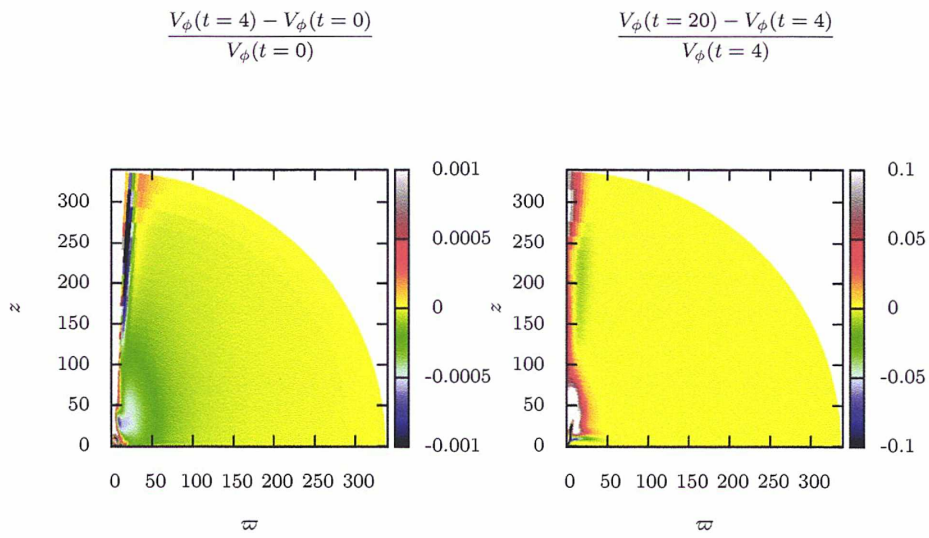
C.2 Pressure

Relative differences $\left(\dfrac{P(t=50) - P(t=0)}{P(t=0)} \right)$ are plotted on Fig. C.3 and C.4

C.3 B_R

Relative differences $\left(\dfrac{B_R(t=50) - B_R(t=0)}{B_R(t=0)} \right)$ are plotted on Fig. C.5 and C.6

C.4 B_θ

Relative differences $\left(\dfrac{B_\theta(t=50) - B_\theta(t=0)}{B_\theta(t=0)} \right)$ are plotted on Fig. C.7 and C.8

C.5 B_ϕ

Relative differences $\left(\dfrac{B_\phi(t=50) - B_\phi(t=0)}{B_\phi(t=0)} \right)$ are plotted on Fig. C.9 and C.10

C.6 V_R

Relative differences $\left(\dfrac{V_R(t=50) - V_R(t=0)}{V_R(t=0)} \right)$ are plotted on Fig. C.11 and C.12

C.7 V_θ

Relative differences $\left(\dfrac{V_\theta(t=50) - V_\theta(t=0)}{V_\theta(t=0)} \right)$ are plotted on Fig. C.13 and C.14

C.8 $V\phi$

Relative differences $\left(\dfrac{V_\phi(t=50) - V_\phi(t=0)}{V_\phi(t=0)} \right)$ are plotted on Fig. C.15 and C.16
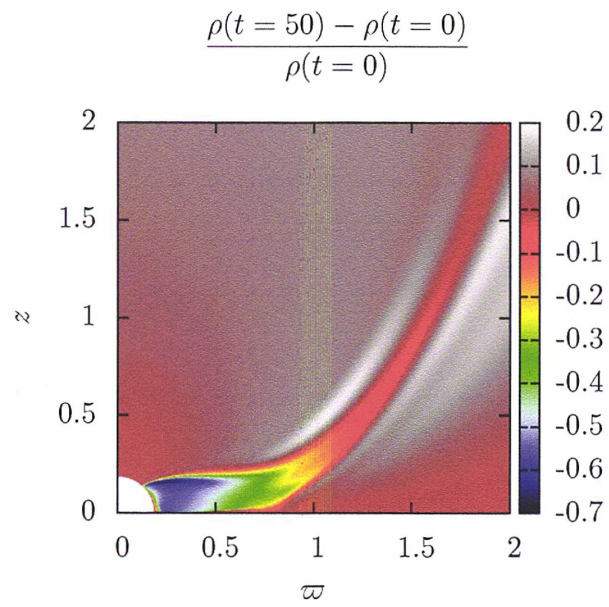
$$\frac{\rho(t=50) - \rho(t=0)}{\rho(t=0)}$$

FIGURE C.1: Relative change in density on the ejection scale

$$\frac{\rho(t=50) - \rho(t=0)}{\rho(t=0)}$$
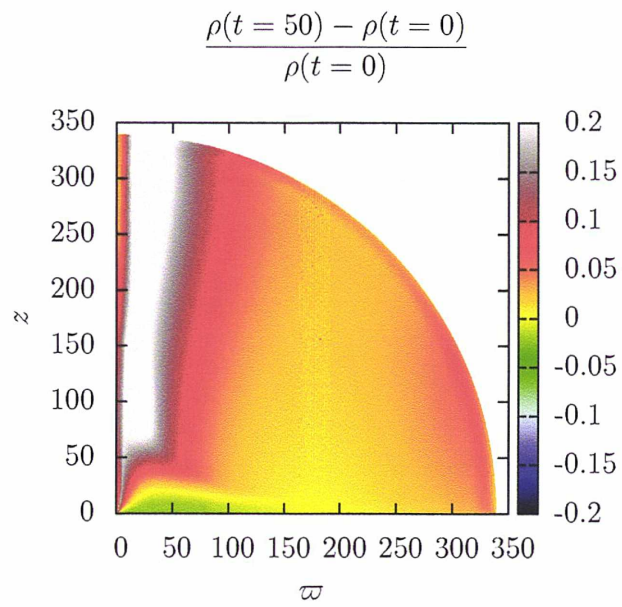
FIGURE C.2: Relative change in density on the propagation scale

$$\frac{P(t=50) - P(t=0)}{P(t=0)}$$
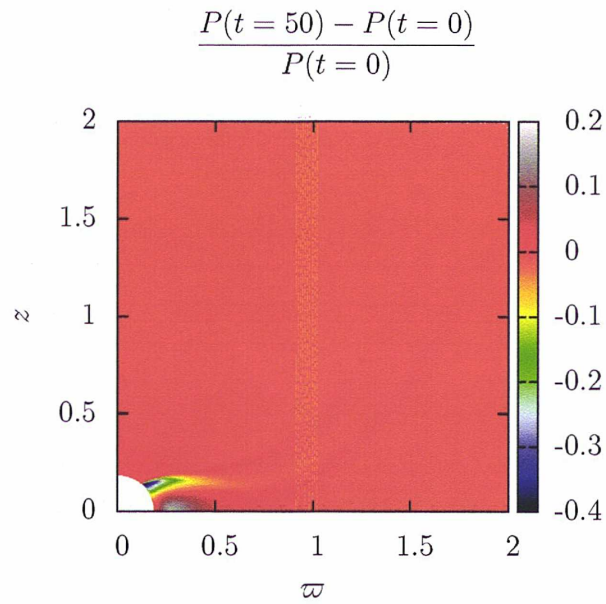
FIGURE C.3: Relative change in pressure on the ejection scale

$$\frac{P(t=50) - P(t=0)}{P(t=0)}$$
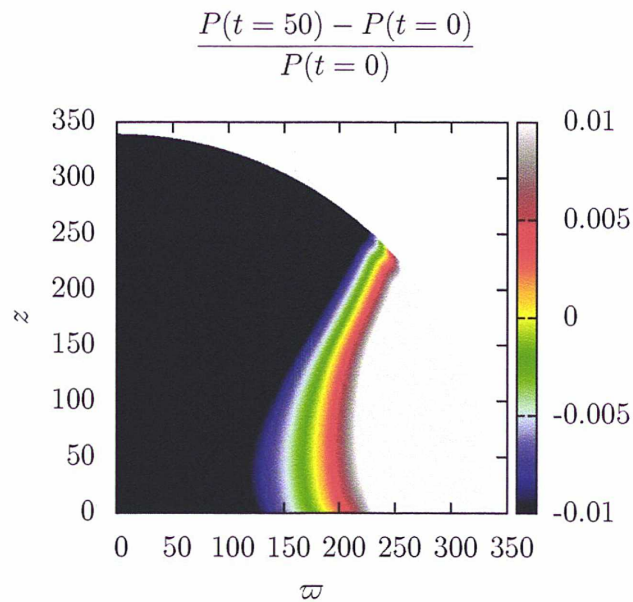
FIGURE C.4: Relative change in pressure on the propagation scale

$$\frac{B_r(t=50) - B_r(t=0)}{B_r(t=0)}$$
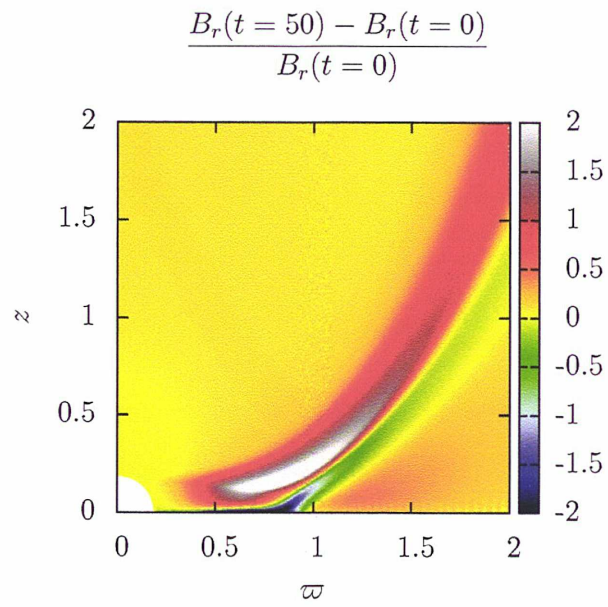
FIGURE C.5: Relative change in radial magnetic field on the ejection scale

$$\frac{B_r(t=50) - B_r(t=0)}{B_r(t=0)}$$
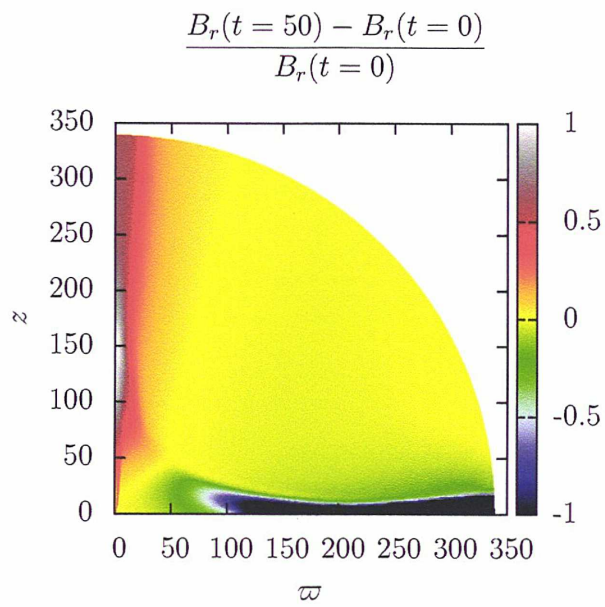
FIGURE C.6: Relative change in radial magnetic field on the propagation scale

$$\frac{B_\theta(t=50) - B_\theta(t=0)}{B_\theta(t=0)}$$
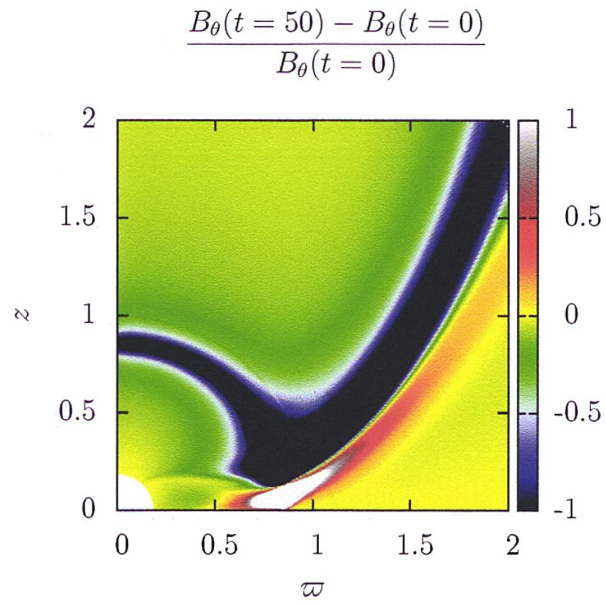
FIGURE C.7: Relative change in longitudinal magnetic field on the ejection scale

$$\frac{B_\theta(t=50) - B_\theta(t=0)}{B_\theta(t=0)}$$
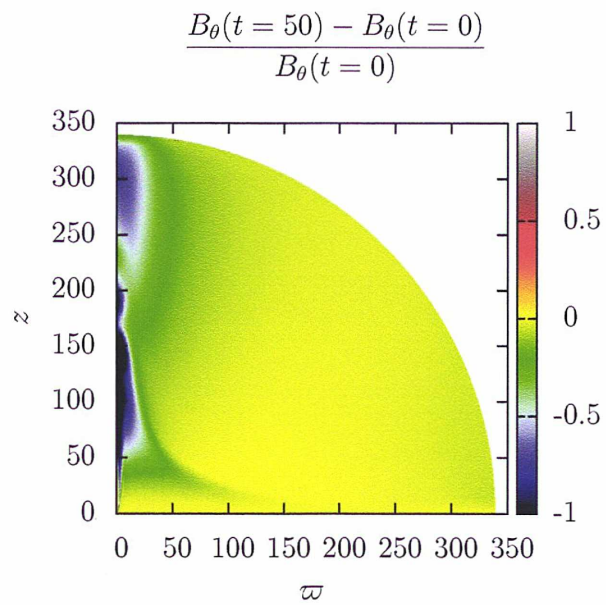
FIGURE C.8: Relative change in longitudinal magnetic field on the propagation scale

$$\frac{B_\phi(t=50) - B_\phi(t=0)}{B_\phi(t=0)}$$
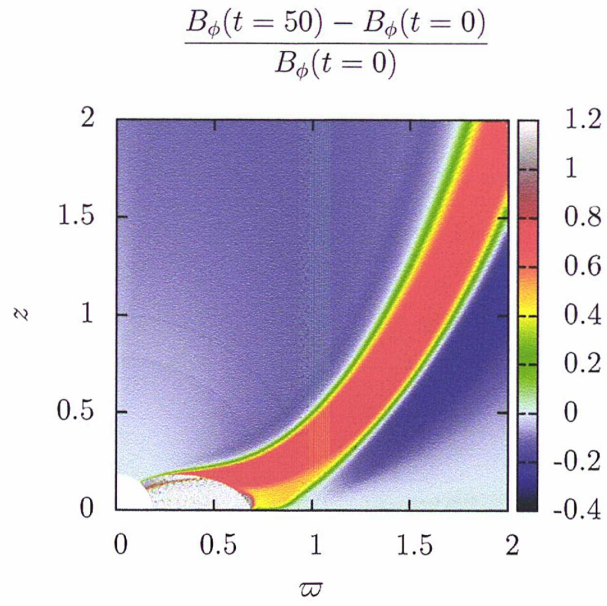
FIGURE C.9: Relative change in toroidal magnetic field on the ejection scale

$$\frac{B_\phi(t=50) - B_\phi(t=0)}{B_\phi(t=0)}$$
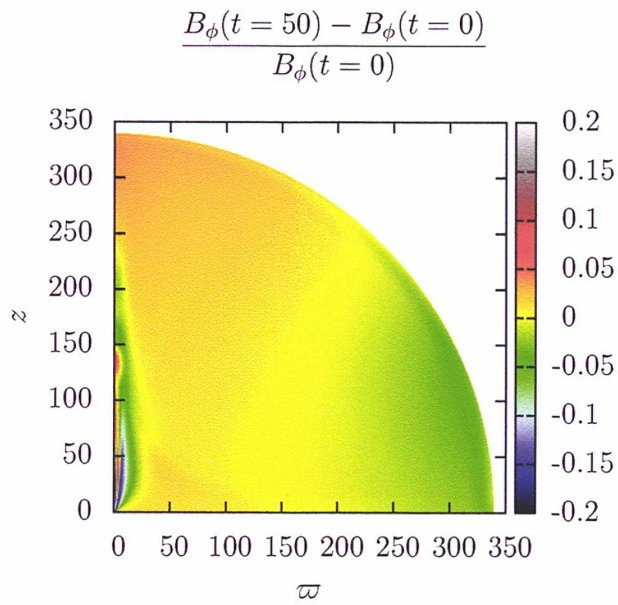
FIGURE C.10: Relative change in toroidal magnetic field on the propagation scale

$$\frac{V_r(t=50) - V_r(t=0)}{V_r(t=0)}$$
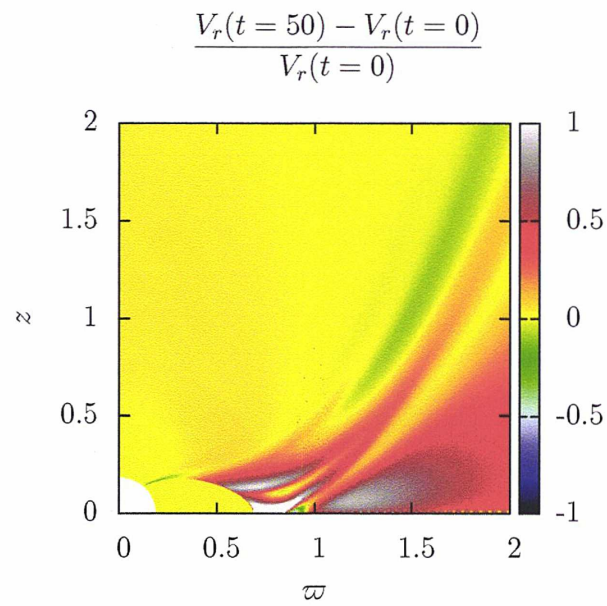
FIGURE C.11: Relative change in radial velocity on the ejection scale

$$\frac{V_r(t=50) - V_r(t=0)}{V_r(t=0)}$$
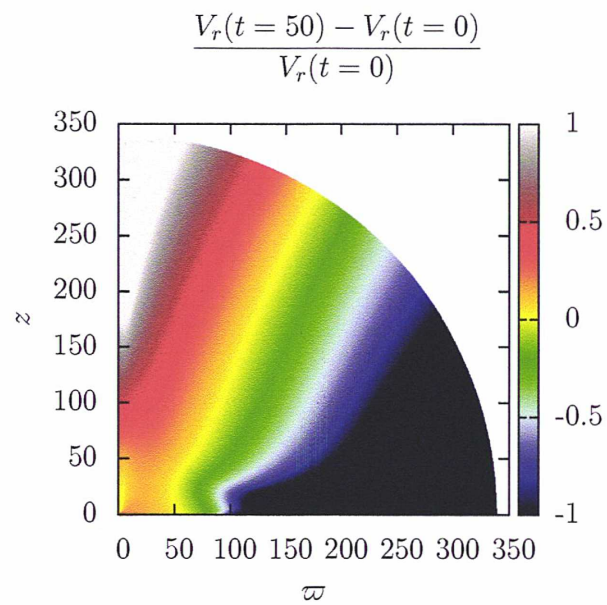
FIGURE C.12: Relative change in radial velocity on the propagation scale

$$\frac{V_\theta(t=50) - V_\theta(t=0)}{V_\theta(t=0)}$$
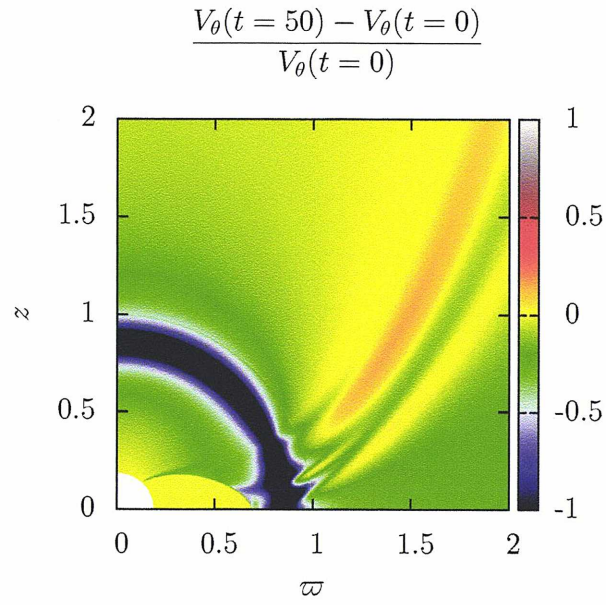
FIGURE C.13: Relative change in longitudinal velocity on the ejection scale

$$\frac{V_\theta(t=50) - V_\theta(t=0)}{V_\theta(t=0)}$$
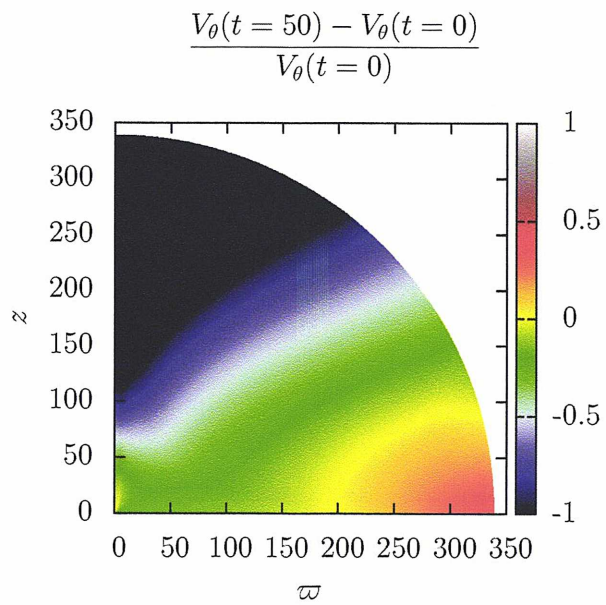
FIGURE C.14: Relative change in longitudinal velocity on the propagation scale

$$\frac{V_\phi(t = 50) - V_\phi(t = 0)}{V_\phi(t = 0)}$$
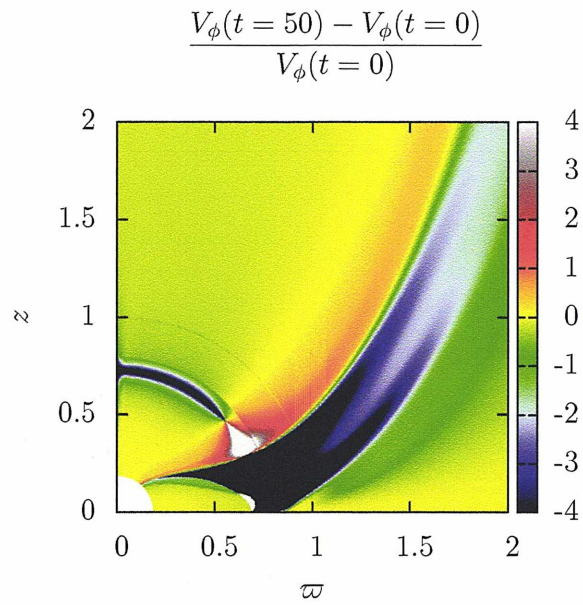
FIGURE C.15: Relative change in toroidal velocity on the ejection scale

$$\frac{V_\phi(t = 50) - V_\phi(t = 0)}{V_\phi(t = 0)}$$
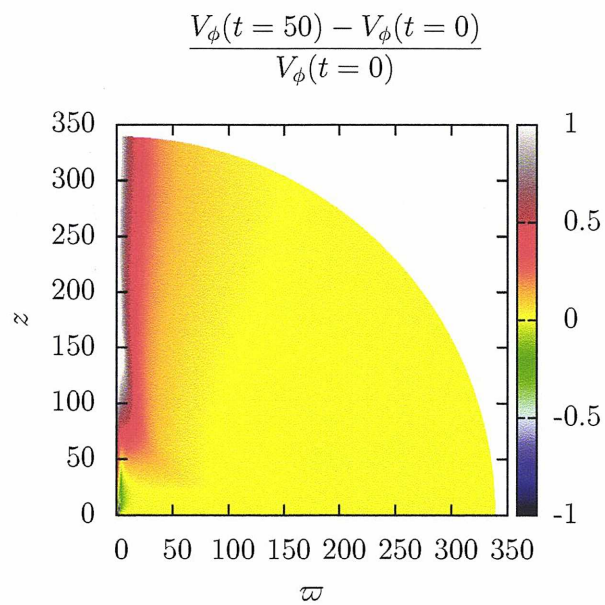
FIGURE C.16: Relative change in toroidal velocity on the propagation scale

Bibliography

[1] Agra-Amboage, V., 2009, *Protostellar Jets in Context*, Tsinganos, K.; Ray, T.; Stute, M. (Eds), p. 143, Springer, ISBN: 1570-6591 Quoted on pp. 36

[2] Agra-Amboage, V. *et al.*, 2009, *A&A*, **493**, 1029–1041 Quoted on pp. 60

[3] Agra-Amboage, V. *et al.*, 2011, *A&A*, **532**, A59 Quoted on pp. 36

[4] Anderson, V. *et al.*, 2003, *ApJ*, **590**, L107–L110 Quoted on pp. 42

[5] André, P.; Ward-Thompson, D.; Barsony, M., 2000, *Protostars & Planets*, **IV**, Mannings, V; Boss, A.P.; & Russell, S. S. (Eds.), University of Arizona Press, ISBN-13 978-0816520596, pp. 59–96 Quoted on pp. 32

[6] Arce, H. G. *et al.*, 2006, *Protostars & Planets*, **V**, Reipurth, B; Jewitt, D; and Keil, K. (Eds.), University of Arizona Press, ISBN-13 978-0816526543 Quoted on pp. 35, 36, 39, 41

[7] Bacciotti, F. *et al.*, 2000, *ApJ*, **537**, L49–L52 Quoted on pp. 36, 42

[8] Bacciotti, F. *et al.*, 2002, *ApJ*, **576**, 222 Quoted on pp. 43, 44

[9] Balbus, S. A.; Hawley, J. F., *et al.*, 1991, *ApJ*, **376**, 214–233 Quoted on pp. 34

[10] Barral, J. F.; Canto, J., 1981, *RMA&A*, **5**, 101 Quoted on pp. 40

[11] Beck, T.L. *et al.*, 2008, *ApJ*, **676**, 472 Quoted on pp. 36

[12] Belloche, A., 2013, *EES 2012*, **180**, Hennebelle, P.; Charbonnel, C. (Eds.) Quoted on pp. 34, 43, 44

[13] Beskin, V.S., 2010, *Usp. Fiz. Nauk*, **180**, 1241–1278 Quoted on pp. 64

[14] Beuther, H. *et al.*, 2002, *A&A*, **387**, 931 Quoted on pp. 39, 43

[15] Blandford, R.D.; Payne, D. G., 2012, *MNRAS*, **199**, 883–903 39

[16] Blandford, R.D.; Thorne, K. S., 2012, "Applications of classical physics" (course textbook) Quoted on pp. 50

[17] Bogovalov, S.V., 1998, *Pis'ma Astr. Zhur.*, **24**, 321 Quoted on pp.

[18] Bontemps, S., 1996, *A&A*, **311**, 858 Quoted on pp. 36, 37

[19] Bouvier, J., 1990, *AJ*, **99**, 946 Quoted on pp. 34

[20] Bouvier, J.; Forestini, M.; Allain, S., 1997, *A&A*, **326**, 1023–1043 Quoted on pp. 31

[21] Cabrit, S.; André, P., 1991, *ApJ*, **379**, L25–L28 Quoted on pp. 38

[22] Cabrit, S.; Bertout, C., 1992, *A&A*, **261**, 274–284 Quoted on pp. 37

[23] Cabrit, S. *et al.*, 1990, *ApJ*, **354**, 687–700 Quoted on pp. 37, 38

[24] Cabrit, S. *et al.*, 2006, *A&A*, **452**, 897 Quoted on pp.

[25] Cabrit, S., 2007, in *Lect. Notes Phys.*, **723**, 3; Ferreira, J; Dougados, C; Whelan, E; (Eds.), Springer ISBN 978-3-540-68033-8 Quoted on pp. 35, 36, 37, 38, 40, 41

[26] Cabrit, S., 2009, *Protostellar Jets in Context*, Tsinganos, K.; Ray, T.; Stute, M. (Eds), p. 143, Springer, ISBN: 1570-6591 Quoted on pp. 38

[27] Cai, M.J. *et al.*, 2008, *ApJ*, **672**, 489–503 Quoted on pp. 44

[28] Cai, M.J., 2009, *Protostellar Jets in Context*, Tsinganos, K.; Ray, T.; Stute, M. (Eds), p. 143, Springer, ISBN: 1570-6591 Quoted on pp. 40

[29] Cerqueira, A. H.; de Gouveia Dal Pino, E. M., 2004, *A&A*, **426**, L25–L28 Quoted on pp. 37

[30] Chrysostomou, A.; Lucas, P. W.; Hough, J. H., 2007, *Nature*, **450**, 71-73 Quoted on pp. 41

[31] Coffey *et al.*, 2004, *ApSS*, **292**, 553 Quoted on pp. 43, 44

[32] Coffey, D.; Bacciotti, F.; Podio, L., 2008, *ApJ*, **689**, 1112–1126 Quoted on pp. 36, 37

[33] Collier Cameron, A., 1988, *MNRAS*, **233**, 235–256 Quoted on pp. 84

[34] Collier Cameron, A.; Robinson, R. D., 1989a, *MNRAS*, **236**, 57–87 Quoted on pp. 84, 85

[35] Collier Cameron, A.; Robinson, R. D., 1989b, *MNRAS*, **238**, 657–674 Quoted on pp. 84, 85

[36] Collier Cameron, A., 1996, *Proced. IAUS*, **176**, 449 Quoted on pp. 85

[37] Contopoulos, J.; Lovelace, R. V. E., 1994, *ApJ*, **429**, 139–152 Quoted on pp. 40

[38] Contopoulos, I.; Sauty, C., 2001, *A&A*, **365**, 165–173 Quoted on pp. 29

[39] Davis, C. J. *et al.*, 2000, *MNRAS*, **314**, 241 Quoted on pp. 43

[40] Decampli, W. M., 1981, *ApJ*, **244**, 124–146 Quoted on pp. 62, 69, 83

[41] Donati *et al.*, 2008, *MNRAS*, **386**, 1234–1251 Quoted on pp. 85, 98

[42] Dopita, M. A.; Evans, I.; Schwartz, R. D., 1982, *ApJ*, **263**, L73-L77 Quoted on pp. 35

[43] Dougados, C. *et al.*, 2004, *Ap & S S*, **293**, 45–52 Quoted on pp. 36

[44] Dunham, M. M.; Vorobyov, E. I., 2012, *ApJ*, **747**, 52 Quoted on pp. 29, 30

[45] Dwivedi, B. N.; *"The Dynamic Sun"*, Cambridge University Press, ISBN 0521810574 Quoted on pp. 85

[46] Evans, N. J. *et. al.*, 2009, *ApJS*, **181**, 321–350 Quoted on pp. 29

[47] Edwards, S., 1993, *Protostars & Planets*, **III**, Levy, E.H.; Lunine, J. (Eds.), University of Arizona Press, ISBN-13 978-0816513345, p. 567 Quoted on pp. 34

[48] Edwards, S., 1997, *IAUS*, **182**, Reipurth, B. & Bertout, C. (Eds.) 433–442 Quoted on pp. 43

[49] Eislöffel, J., 2000, *Protostars & Planets*, **IV**, Mannings, V; Boss, A.P.; & Russell, S. S. (Eds.), University of Arizona Press, ISBN-13 978-0816520596, pp. 815–840 Quoted on pp. 35

[50] Fendt, C.; Camenzind, M.; Appl, S., *A&A*, **300**, 791 Quoted on pp. 47

[51] Fendt, C., 2009, *ApJ*, **692**, 346–363 Quoted on pp. 75

[52] Fendt, C., 2011, *ApJ*, **737**, 43 Quoted on pp. 44

[53] Ferraro, V. C. A., 1937, *MNRAS*, **147**, 220. Quoted on pp. 53

[54] Ferreira, J. M.; Mendoza-Briceño, C. A., 1997, *A&A*, **327**, 252–264 Quoted on pp. 85

[55] Ferreira, J. M., 1997, *A&A*, **319**, 340 Quoted on pp. 40

[56] Ferreira, J.; Pelletier, G.; Appl, S., 2000, *MNRAS*, **312**, 387 Quoted on pp. 40

[57] Ferreira, J.; Dougados, C.; Cabrit, S., 2006, *A&A*, **453**, 785 Quoted on pp. 39, 42

[58] Ferreira, J., 2007, in *Lect. Notes Phys.*, **723**, 3; Ferreira, J; Dougados, C; Whelan, E; (Eds.), Springer ISBN 978-3-540-68033-8 Quoted on pp. 41

[59] Ferreira, J. M., 2009, *Protostellar Jets in Context*, Tsinganos, K.; Ray, T.; Stute, M. (Eds), pp. 99-110, Springer, ISBN: 1570-6591 Quoted on pp. 38

[60] Ferreira, J. M.; Deguiran, R., 2013, *HEDP*, **9**, 67–74 Quoted on pp.

[61] Globus, N., 2011, PhD Thesis, Observatoire de Paris URL: http://www.sudoc.fr/161678858. Quoted on pp. 62

[62] Gracia, J.; Vlahakis, N.; Tsinganos, K., 2006, *MNRAS*, **367**, 201 Quoted on pp. 62

[63] Grad, H.; Rubin, H.,1958, *Proc. 2nd. UN Conf. Peac. Us. At. En.*, **31**, 190. Quoted on pp. 58

[64] Goodman, J., 1993, *ApJ*, **406**, 596–613 Quoted on pp. 34

[65] Gomez, M.; Whitney, B. A.; Kenyon, S. J., 1997, *AJ*, **114**, 1138 Quoted on pp. 38

[66] Gómez de Castro, A.I.; Verdugo, E., 2001, *ApJ*, **548**, 976–989 Quoted on pp. 60

[67] Graham, J. A.; Elias, J. H., 1983, *ApJ*, **272**, 615–617 Quoted on pp. 35

[68] Günther, H.M. *et al.*, 2013, *ApJ*, **771**, 70 Quoted on pp. 31

[69] Günther, H.M. *et al.*, 2013, *A&A*, **552**, A142 Quoted on pp. 31

[70] Herbig, G.H, 1950, *ApJ*, **111**, 11 Quoted on pp. 35

[71] Haro, G., 1950, *AJ*, **55**, 72 Quoted on pp. 35

[72] Hartmann, L., 2009, *"Accretion processes in star formation"*, Cambridge University Press, ISBN-13 978-0-521-53199-3. Quoted on pp. 26, 29, 31

[73] Hartigan, P.; Edwards, S.; Ghandour, L., 1995, *ApJ*, **452**, 736 Quoted on pp. 37

[74] Hartigan, P.; Edwards, S.; Pierson, R., 2004, *ApJ*, **609**, 261 Quoted on pp. 42

[75] Hartigan, P.; 2009, *Protostellar Jets in Context*, Tsinganos, K.; Ray, T.; Stute, M. (Eds), p. 143, Springer, ISBN: 1570-6591 Quoted on pp. 41

[76] Hatchell, J.; Fuller, G. A.; Richer, J. S., 2007, *A&A*, **472**, 187-198 Quoted on pp. 37

[77] Hoffleit, D., 1997, *JAVSO*, **25**, 115 Quoted on pp. 25

[78] Heyvaerts, J.; Norman, C., 1989, *ApJ*, **347**, Quoted on pp. 64

[79] Joy, A. H., 1945, *ApJ*, **102**, 168 Quoted on pp. 25

[80] Klaassen, P.D. *et al.*, 2013, *A&A*, **555**, A73 Quoted on pp. 43

[81] Keppens, R.; Goedbloed, J. P., 1999, *A&A*, **343** 251-260. Quoted on pp. 83, 86

[82] Königl, A.; Pudritz, R. E., 2000, *Protostars & Planets*, **IV**, Mannings, V; Boss, A.P.; & Russell, S. S. (Eds.), University of Arizona Press, ISBN-13 978-0816520596, pp. 815-840 Quoted on pp. 39

[83] Kundurthy, P. *et al.*, 2006, *AJ*, **132**, 2469-2477 Quoted on pp. 31

[84] Lee, C.-F. *et al.*, 2000, *ApJ*, **542**, 925-945 Quoted on pp. 40

[85] Lee, C.-F. *et al.*, 2001, *ApJ*, **549**, 1231-1231 Quoted on pp. 40

[86] Lee, C.-F. *et al.*, 2002, *ApJ*, **576**, 294-312 Quoted on pp. 40

[87] Mathieu, R. D., 2004, *Proc. IAUS*, **215**, Maeder, A; Eenens, P. (Eds.), 168 Quoted on pp. 34

[88] Matsakos, T. *et al.*, 2008, *A&A*, **477**, 521-533 Quoted on pp. 63, 65, 70, 82

[89] Matsakos, T. *et al.*, 2009, *A&A*, **502**, 21 Quoted on pp. 63, 65, 70

[90] Matt, S.; Pudritz, R. E., 2005, *ApJ*, **632**, L135-L138 Quoted on pp. 40, 69

[91] Matt, S.; Pudritz, R. E., 2008, *ApJ*, **678**, 1109 Quoted on pp. 32

[92] Matt, S.; Pudritz, R. E., 2008, *ApJ*, **681**, 391 Quoted on pp.

[93] Matzner, C. D.; McKee, C. F., 2000, *ApJ*, **545**, 364–378 Quoted on pp.

[94] Mundt, R.; Fried, J. W., 1983, *ApJ*, **274**, L83-L86 Quoted on pp. 35

[95] McCaughrean, M.J.;Stapelfeldt, K.R.; & Close, L.M.,2000, *Protostars & Planets*, **IV**, Mannings, V; Boss, A.P.; & Russell, S. S. (Eds.), University of Arizona Press, ISBN-13 978-0816520596, pp. 59–96 Quoted on pp. 37

[96] McKee, C. F.; Ostriker, E. C., 2007, *ARA&A*, **45**, 565 Quoted on pp. 27, 28, 30, 32

[97] Meliani, Z.; Casse, F.; Sauty, C., 2006, *A&A*, **460**, 1 Quoted on pp.

[98] Mestel, L., 1968, *MNRAS*, **138** 359–391. Quoted on pp. 83

[99] Mestel, L.; Spitzer, L., Jr., 1956, *MNRAS*, **116**, 503 Quoted on pp. 28

[100] Mestel, L.; Spruit, H. C., 1987, *MNRAS*, **226**, 57–66 Quoted on pp.

[101] Mestel, L, 2012, *"Stellar magnetism,"* Oxford university press, second edition ISBN:978-0-19-964174-1 32, 41, 47, 54, 69, 85

[102] Mignone, A. *et al.*, 2007, *ApJS*, **170**, 228 Quoted on pp. 50, 71

[103] Molinari, S. *et al.*, 2010, *A&A*, **518**, 100 Quoted on pp. 26

[104] Nisini, B., 2009, *Protostellar Jets in Context*, Tsinganos, K.; Ray, T.; Stute, M. (Eds), p. 215, Springer, ISBN:1570-6591 Quoted on pp. 37

[105] Pagani, L. *et al.*, 2010, *Science*, **329**, 1622 Quoted on pp. 26
[105]

[106] Perrin, M. D.; Graham, J. R., 2007, *ApJ*, **670**, 499–508. Quoted on pp. 38

[107] Pelletier, G.; Pudritz, R. E., 1992, *ApJ*, **394**, 117–138 Quoted on pp. 42

[108] Pesenti *et al.*, 2003, *A&A*, **410**, 155–164 Quoted on pp. 37

[109] Pizzo, V. J., 1983, *NASCP*, **2280**, 675 Quoted on pp.

[110] Pinto, R. F. *et al.*, 2011, *ApJ*, **737**, 72 Quoted on pp. 34

[111] Pneuman, G. W.; Kopp, R. A., 1971, *SoPh*, **18** 258. Quoted on pp. 83

[112] Pudritz, R. E.; Rogers, C. S.; Ouyed, R., 2006, *MNRAS*, **365**, 1131 Quoted on pp.

[113] Pudritz, R. E. *et al.*, 2006, *Protostars & Planets*, **V**, Reipurth, B; Jewitt, D; and Keil, K. (Eds.), University of Arizona Press, ISBN-13 978-0816526543 Quoted on pp.

[114] Pneuman, G. W., 1972, *ApJ*, **177**, 793 Quoted on pp.

[115] Ray, T., 1998, in *Ap Jets: Op. Pr.*; Massaglia, S; Bodo, G. (Eds.), Springer ISBN 90-5699637-1 Quoted on pp. 35

[116] Ray, T., 2007, in *Lect. Notes Phys.*, **723**, 3; Ferreira, J; Dougados, C; Whelan, E; (Eds.), Springer ISBN 978-3-540-68033-8 Quoted on pp. 25, 26, 27, 28, 29, 31

[117] Reipurth, B., 1986, *A&A*, **164**, 51–66 Quoted on pp. 35

[118] Reipurth, B.; Bally, J., 2001, *ARA&A*, **39**, 403 Quoted on pp. 35

[119] Richer, J.S., 2000, *Protostars & Planets*, **IV**, Mannings, V; Boss, A.P.; & Russell, S. S. (Eds.), University of Arizona Press, ISBN-13 978-0816520596, pp. 59–96 Quoted on pp.

[120] Salmeron, R.; Königl, A.; Wardle, M., 2011, *MNRAS*, **412**, 1162–1180 Quoted on pp. 40

[121] Sauty, C; Tsinganos, K., 1994, *A&A*, **287**, 893–926. Quoted on pp. 40, 55, 56, 57, 62, 82

[122] Sauty, C.; Tsinganos, K.; Trussoni, E. , 1999, *A&A*, **348**, 327 Quoted on pp. 55

[123] Sauty, C.; Trussoni, E.; Tsinganos, K. , 2002, *A&A*, **389**, 1068 Quoted on pp. 55, 69

[124] Sauty, C.; Meliani, Z.; Trussoni, E.; Tsinganos, K., 2004a, *ApSS*, **293**, 75 Quoted on pp. 55

[125] Sauty, C.; Trussoni, E.; Tsinganos, K., 2004b, *A&A*, **421**, 797 Quoted on pp. 55

[126] Sauty, C., Meliani, Z., Lima, J. J. G., *et al.*, 2011, *A&A*, **533**, A46 Quoted on pp. 15, 21, 31, 55, 58, 60, 61, 62, 63, 82, 85, 98

[127] Sauty, C. *et al.*, 2012, *ApJ*, **759**, L1 Quoted on pp. 44

[128] Schatzman, E., 1962, *Ann. Astr.*, **25**, 18 Quoted on pp. 77

[129] Schroeder, K. P., 1983, *A&A*, **124**, 16 Quoted on pp. 84

[130] Shafranov, V.D., 1966, *Rev. Plas. Phys.*, **2**, 103 Quoted on pp. 58

[131] Shepherd, D. S.; *et al.*, 1998, *ApJ*, **507**, 861–873 Quoted on pp. 38

[132] Shu, F.H., 1977, *ApJ*, **214**, 488–497 Quoted on pp. 30

[133] Shu, F.H. *et al.*, 1988, *ApJ*, **328**, L19–L23 Quoted on pp. 40

[134] Shu, F. H. *et al.*, 2000, *Protostars & Planets*, **IV**, Mannings, V; Boss, A.P.; & Russell, S. S. (Eds.), University of Arizona Press, ISBN-13 978-0816520596, pp. 59–96 Quoted on pp. 39

[135] Soker, N., 2005, *A&A*, **435**, 125–129 Quoted on pp. 44

[136] Stahler, S. W., 1988, *ApJ*, **274**, 822–829 Quoted on pp. 30

[137] Spitzer, L., 1978, "Physical processes in the interstellar medium", New York Wiley-Interscience, ISBN-13: 978-0471293354 Quoted on pp. 32

[138] St-Onge, G.; Bastien, P., 2008, *ApJ*, **674**, 1032–1036 Quoted on pp. 60

[139] Stix, M., 2004, "The Sun: an introduction", Berlin: Springer, ISBN: 3540207414 Quoted on pp. 85

[140] Sonnentrucker, P. *et al.*, 2010, *A&A*, **521**, 12 Quoted on pp. 26

[141] Takahashi, S.; Ho, P. T. P., 2012, *ApJL*, **745**, L10 Quoted on pp. 35

[142] Trussoni, E.; Tsinganos, K.; Sauty, C., 1997, *A&A*, **325**, 1099 Quoted on pp. 55

[143] Tsinganos, K., 1981, *ApJ*, **245**, 764 Quoted on pp. 53

[144] Tsinganos, K.; Low, B. C., 1989, *ApJ*, **342**, 1028–1048 Quoted on pp. 83

[145] Tsinganos, K.; Trussoni, E., 1991, *A&A*, **249**, 156–172 Quoted on pp.

[146] Tsinganos, K.; Sauty, C., 1992, *A&A*, **255**, 405 Quoted on pp. 54

[147] Tsinganos, K.; Sauty, C., 1992b, *A&A*, **257**, 790 Quoted on pp. 55

[148] Tsinganos, K.; Sauty, C.; Surlantzis, G.; Trussoni, E.; Contopoulos, J., 1996, *MNRAS*, **283**, 811–820 Quoted on pp. 64

[149] Tsinganos, K., 2007, in *Lect. Notes Phys.*, **723**, 3; Ferreira, J; Dougados, C; Whelan, E; (Eds.), Springer ISBN 978-3-540-68033-8 Quoted on pp. 40, 41, 47, 49, 64

[150] Tzeferacos, P. *et al.*, 2009, *MNRAS*, **400**, 820–834 Quoted on pp. 40

[151] Vogel, S. N.; Kuhi, L. V., 1981, *ApJ*, **245**, 960–976 Quoted on pp. 34

[152] Wilner, D.J..; Lay, O. P., 2000, *Protostars & Planets*, **IV**, Mannings, V; Boss, A.P.; & Russell, S. S. (Eds.), University of Arizona Press, ISBN-13 978-0816520596, pp. 815–840 Quoted on pp. 42

[153] Wu, Y.; Huang, M.; He, J., 1996, *A&AS*, **115**, 283 Quoted on pp. 37

[154] Wu, Y. *et al.*, 2004, *A&A*, **426**, 503–515 Quoted on pp. 37

[155] Parker, E., 1963, "Interplanetary dynamical processes," New York, Interscience Publishers Quoted on pp. 69

[156] White, N. E.; Culhane, J. L.; Parmar, A. N.;, 1986, *ApJ*, **301**, 262 Quoted on pp. 84

[157] Zanni, C., 2009, *Protostellar Jets in Context*, Tsinganos, K.; Ray, T.; Stute, M. (Eds), p. 143, Springer, ISBN: 1570-6591 Quoted on pp. 40

[158] Zanni, C.; Ferreira, J., 2013, *A&A*, **550**, A99 Quoted on pp. 75